UNIVERSITY OF TECHNOLOGY SYDNEY

Fuel economy analysis and powertrain dynamic control of a parallel hydraulic hybrid vehicle

by Shilei Zhou

Thesis submitted in fulfilment of the requirements for the degree of

Doctor of Philosophy

under the supervision of Dr. Paul Walker, Prof. Nong Zhang

University of Technology Sydney
Faculty of Engineering and Information Technology

August 2021

Certificate of Original Authorship

I, Shilei Zhou declare that this thesis, is submitted in fulfilment of the requirements for the award of Doctor of Philosophy, in the Faculty of Engineering and Information Technology at the University of Technology Sydney.

This thesis is wholly my own work unless otherwise referenced or acknowledged. In addition, I certify that all information sources and literature used are indicated in the thesis.

This document has not been submitted for qualifications at any other academic institution.

This research is supported by the Australian Government Research Training Program.

Signature of Student: Production Note:
Signature removed prior to publication.

Date: August 2021

Acknowledgements

During the journal of my PhD study, I have got too much help from many people to whom I want to show my acknowledgements. First I want to express my appreciation to my principal supervisor Dr. Paul Walker who gives me invaluable help in building my research skills. Since I started my PhD study, He guides me to develop a completed research plan with his knowledge and experience. With clear targets, I work step by step and get expected results. He also helps me with my English writing, paper organization, oral presentation and many other skills a researcher needs.

I would also like to thank my co-supervisor Prof. Nong Zhang who gives a lot of advice with his broad academic vision. His more than thirty years of research experience helps me to have a better understanding of the history and trend of automotive technology. His passion and enthusiasm for academics always encourage me to work harder and harder.

I always feel blessed to have these outstanding people as my teammates: Yang Tian, Cong Thanh Nguyen, Boyi Xiao, Anna lidfors Lindqvist, Pu Gao, Hanfei Wu, Enoch Zhao, Jinglai Wu, Jiageng Ruan, Jiejunyi Liang, Haitao Yang, Wenwei Mo, Weiwei Yang, Shengxiong Sun. Thank you for giving me help on my research and even more for making my life a happier one.

The financial supports from the China Scholarship Council and University of Technology Sydney are much appreciated.

No matter where I am and what I do, I know my family is always behind me and unconditionally supporting me. Thank you and love you.

Table of Contents

List of Figures

List of Tables

Abbreviation

AMT	Automated manual transmission
BSFC	Brake specific fuel consumption
CEM	Centralized electric motor
CEV	Centralized motor drive vehicle
CHM	Centralized hydraulic motor
CTUDC	Chinese typical urban driving cycle
DP	Dynamic programming
EKF	Extended Kalman filter
EMS	Energy management strategy
HEV	Hybrid electric vehicle
HPA	High pressure accumulator
HPM	Hydraulic pump/motor
IEM	In-wheel electric motor
IEV	In-wheel drive electric vehicle
IHM	In-wheel hydraulic pump/motor
IHV	In-wheel drive electric hydraulic hybrid vehicle
LPA	Low pressure accumulator
LQR	Linear quadratic regulator
PHHV	Parallel hydraulic hybrid vehicle
PSHHV	Power-split hydraulic hybrid vehicle
SHHV	Series hydraulic hybrid vehicle
SoC	State of charge
WLTP-3	World harmonized light-duty vehicles test procedure class 3

Notation

Common symbols which are used at different places in thesis are listed below and will only be explained when they firstly appear in thesis to avoid redundancy.

M	Vehicle mass	g	Gravitational acceleration
a	Vehicle acceleration	V	Vehicle speed
δ	Vehicle rotational inertia factor	A_f	Vehicle frontal area
R_w	Tyre dynamic radius	ρ_{air}	Air density
T_e	Engine torque	C_D	Air drag coefficient
T_h	HPM torque	ϕ	Road slope
T_L	Vehicle resistant torque	f_r	Rolling resistance coefficient
T_c	Engine clutch torque	α	HPM swashplate angle
T_{bm}	Mechanical braking torque	d	HPM cylinder diameter
T_{dri}	Driver torque demand	z_c	HPM cylinder number
i_g	AMT gear ratio	R	HPM cylinder pitch radius
i_f	Main reducer gear ratio	n_h	HPM speed
i_h	HPM gear ratio	n_e	Engine speed
η_e	Engine powertrain efficiency	η_h	Hydraulic powertrain efficiency
J_e	Engine inertia	K_c	Engine clutch stiffness
J_c	Engine clutch inertia	K_o	AMT output shaft stiffness
J_i	AMT input shaft inertia	K_s	Driveshaft stiffness
J_o	AMT output shaft and driveshaft inertia	K_t	Tyre stiffness
J_f	Main reducer inertia	K_h	HPM clutch stiffness
J_v	Vehicle body inertia	C_c	Engine clutch damping
J_h	HPM inertia	C_h	HPM clutch damping
θ_e	Engine angular displacement	C_t	Tyre damping
θ_c	Engine clutch angular displacement		

θ_i AMT input shaft angular displacement

θ_o AMT output shaft and driveshaft angular displacement

θ_f Main reducer angular displacement

θ_w Wheel angular displacement

θ_h HPM angular displacement

Abstract

This research investigates the fuel economy and powertrain vibration characteristics of a parallel hydraulic hybrid vehicle (PHHV). The main work includes: Hydraulic driving system parameter design, energy management strategy (EMS) design, powertrain vibration analysis and transient process control.

Firstly, hydraulic driving system parameters are selected based on vehicle power analysis with the Chinese typical urban driving cycle (CTUDC) which is a typical urban driving cycle. PHHV powertrain dynamics are analyzed and components such as engine, hydraulic pump/motor (HPM) and accumulator are modelled to demonstrate the PHHV working principle. PHHV fuel economy is verified by both dynamic programming (DP) optimization and practical rule-based EMS. DP optimization is conducted to explore the optimal PHHV fuel economy. The practical rule-based EMS includes driving torque allocation strategy, regenerative braking control strategy and gear shift schedule.

A lumped parameter dynamic model is built to capture the PHHV powertrain vibration characteristics including the natural frequencies and mode shapes. Then model reduction is conducted to simplify the model complexity while retaining the model fidelity in interested frequency range. The natural frequencies and mode shapes of PHHV powertrain are compared with the original vehicle powertrain which is the vehicle that PHHV refitted from. Results show that the vibration characteristics of PHHV powertrain are not significantly influenced by the addition of hydraulic driving system.

Based on the powertrain dynamic model, control strategies are designed for transient process control such as mode switching and power on gear shifting. During mode switching, engine, HPM and engine clutch are coordinately controlled. LQR based closed-loop control strategy is adopted to analyze the effect of engine clutch engaging speed on vehicle jerk, clutch frictional work and hydraulic energy consumption. HPM torque is adjusted to compensate the engine clutch torque to maintain vehicle dynamic performance. The effectiveness of the proposed mode switching control strategy is verified by simulation.

To avoid vehicle driving torque interruption during gear shifting, power on gear shifting control strategy is designed. In the control strategy, HPM compensates engine torque when engine clutch is disengaged for gear shifting. Engine clutch engagement process is also controlled by LQR controller to mitigate PHHV powertrain vibration and improve

vehicle driving comfort. Extended Kalman filter (EKF) is adopted to estimate the powertrain states required by LQR controller. Because the available HPM torque depends on its working pressure which varies a lot with different accumulator pressure state, the HPM torque compensation capability is investigated by analyzing the traction force requirement during gear shifting under typical urban driving cycles.

With the motivation of taking the advantage of high power density of HPM for in-wheel drive, a novel in-wheel drive electric hydraulic hybrid vehicle (IHV) is proposed as a case study. Its energy economy and vertical vibration characteristics are researched and compared with the centralized motor drive electric vehicle (CEV) and in-wheel drive electric vehicle (IEV).

Chapter 1 Introduction

1.1 Background

The massive production and use of vehicle have led to serious environmental pollution and energy shortage. Research on reducing vehicle emission and increasing energy efficiency has been vigorously promoted in the past decades. Numerous effective solutions have been achieved. From the powertrain perspective, efforts are made on increasing efficiency of power source and reducing energy loss in powertrain.

In recent years, alternative power systems have been developed for vehicle driving while electric motor and hydraulic motor are the most popular ones [1-6]. Regarding to energy storage systems, battery, fuel cell, ultra-capacitor, flywheel and hydraulic accumulator are considered as promising alternative vehicle energy storages [7-9]. Among these energy storages, battery is mostly used in vehicle combined with electric motor. Electric motor is used to drive vehicle individually or combined with engine, which are called battery electric vehicle and hybrid electric vehicle (HEV).

However, electric driving system is mainly used in passenger vehicles and light duty commercial vehicles due to the high cost and low energy density of battery. Engine is still the main power source for medium and heavy duty vehicles. For medium and heavy duty vehicles working in urban area such as refuse collection vehicle, bus and delivery vehicle, their energy efficiencies are remarkably deteriorated with frequent start-stop during operating and traffic waiting [10, 11]. With added power source to launch vehicle from standstill and drive vehicle in low speed, low efficiency working area of engine could be avoided. Besides, considerable braking energy could be recovered. With the hybridization of more than one power source, energy efficiency of these vehicles can be improved.

Considering controllability and torque characteristics, electric motor is a suitable choice. Electric motor has high efficiency in a broad area. However, high power is needed for battery and electric motor when starting and braking a medium or heavy duty vehicle because of its heavy mass. This means large electric motor and battery are required, so that high manufacturing cost is unavoidable [12, 13].

Comparing to electric power source, hydraulic power source takes the advantages of high power density and low cost [14]. It could help launch vehicle quickly and recover more braking energy without adding too much cost. The working condition determines the city

use vehicles have to start and stop frequently. At each start and stop, high power is needed but not very much energy is consumed or generated. This helps to reduce the negative effect of hydraulic accumulator's low energy density [15].

Hydraulic driving system mainly consists of high pressure accumulator (HPA), low pressure accumulator (LPA), control valve, hydraulic motor and hydraulic pump [16]. Hydraulic motor is used as the driving unit in hydraulic hybrid vehicle. Oil flows from HPA to LPA when hydraulic motor drives vehicle. When vehicle works in regenerative braking mode, hydraulic pump is used to transfer the vehicle kinetic energy to hydraulic energy and store it in HPA. Oil is pumped from LPA to HPA during braking [17]. There are generally three types of hydraulic hybrid vehicles, named series hydraulic hybrid vehicle (SHHV), parallel hydraulic hybrid vehicle (PHHV) and power-split hydraulic hybrid vehicle (PSHHV) respectively [18, 19].

In SHHV, engine is used to drive hydraulic pump and vehicle is driven by dual function hydraulic pump/motor (HPM). Hydraulic components are connected by tubes by which hydraulic energy is transferred [20, 21]. Engine is disconnected from wheels, so it can work in high efficiency area most of the time. HPM could also be installed in wheels so that vehicle powertrain could be simplified and vehicle handling and stability could be increased by torque vectoring control [22]. Accumulators can adjust driving torque and reduce engine torque fluctuation. However, a long hydraulic powertrain deteriorates the system efficiency. To satisfy the vehicle power and torque demand, large HPM size is required.

In PHHV, hydraulic driving system is added to vehicle powertrain [23]. Engine and HPM could drive vehicle together or independently. In PHHV, braking energy is recovered by HPM and stored in HPA. This energy is used for launching and driving vehicle, by which the engine low efficiency operating regions are avoided and vehicle fuel economy is improved [24].

PSHHV combines SHHV structure and PHHV structure by parallel shaft or planetary gear set [25] to realize torque coupling and speed coupling [26, 27]. It could work in either series mode or parallel mode. Complicated SPHHV powertrain structure increases the control difficulty.

Among various hydraulic hybrid vehicles, PHHV can be refitted from conventional engine driving vehicle by adding a HPM on it driveshaft, which helps reduce the design cost and simplify the system configuration [28-30]. A thorough investigation on PHHV

is necessary to prove its economical and societal values for commercialization, especially its fuel economy and dynamic performance.

Firstly, hydraulic driving system parameter design methods should be researched. So that based on certain vehicle specifications and working conditions, tailored hydraulic driving systems could be designed and selected to maximize the vehicle fuel economy. Vehicle energy management strategy (EMS) should also be investigated to coordinate the engine driving system, hydraulic driving system and braking system. Besides, with the added hydraulic driving system on driveshaft, the vehicle powertrain vibration characteristics such as natural frequency and mode shape are changed which should also be researched to make sure that the powertrain vibrations are acceptable. In PHHV, mode switching would happen between HPM driving mode and engine driving mode, so control strategy should be designed for this transient process. The implementation of HPM brings another benefit to vehicle dynamic performance which is the power on gear shifting. In the original engine driving vehicle which is equipped with automated manual transmission (AMT), driving torque is cut off to conduct gear shifting. In PHHV, by using HPM to compensate the driving torque during gear shifting, vehicle dynamic performance could be improved.

The above mentioned points are important for PHHV, but not well explored at the moment. The following literature review will give a detailed introduction on the state of the art of PHHV research and the gaps which should be further investigated.

1.2 **Literature review**

Hydraulic driving system parameters have a great impact on vehicle energy efficiency [31]. Hydraulic driving system parameters mainly refer to HPM size and accumulator size. It is a multi-objects optimization process to choose hydraulic driving system parameters [30]. The effect of accumulator size on vehicle energy efficiency is researched in [32] based on a delivery truck. With different accumulator size, the cost, weight and energy efficiency are compared. Compromise should be made according to producer preference when choosing accumulator size. In [33], HPM size and accumulator size are jointly optimized. According to certain driving cycles based on predefined vehicle routine, energy efficiency is set as the target. The best combination of HPM and accumulator is obtained through simulation and the results are verified by experiments. In [29], accumulator size was selected according to the power demand of a bus.

To design PHHV EMS, dynamic programming (DP) is used in [34] to find the maximal PHHV energy saving potential which works as a benchmark for other EMS. A more practical rule-based EMS is designed and compared with the DP optimization results. Based on vehicle working condition and predefined target functions related to fuel economy, local optimization EMS can be designed. Researches show that local optimization EMS can get better energy efficiency than rule-based EMS. In [35], a real time EMS is designed using a cerebellar model articulation controller combined with RBF neural networks. Parameters are trained by the results obtained from DP optimization. Model predictive control strategy is used in [36], the local optimization algorithm is demonstrated to achieve better energy efficiency over ruled-based EMS. Besides, it doesn't need future driving condition information, making it more applicable for real implementation. However, the implementation of local optimization EMS is restricted by limitation of hardware because massive high-speed calculation is required in work.

Some researchers have made significant contributions to PHHV regenerative braking control strategy. PHHV is normally rear wheel driving so more braking force should be allocated to rear wheels in PHHV to maximize the recovered braking energy. However, to maintain vehicle stability during braking, rear wheels should be locked after front wheels. The braking force distribution between front wheels and rear wheels have to be well designed based on the requirements of braking energy recovery and safety restrictions [37, 38]. Hydraulic braking force and mechanical braking force should be allocated considering both safety and energy efficiency. Toque coupler gear shifting schedule is considered in [39] when designing braking control strategy. An optimal braking torque distribution curve and gear shifting schedule are developed for an urban driving condition. Optimization of the PHHV braking process using a hydraulic pump is conducted in [40] with the target of increasing the braking energy recovery rate. In [41], economic commission of Europe regulation is considered when designing regenerative braking control strategy. Some typical urban driving cycles are adopted to validate the control strategy. Vehicle load is taken into consideration when designing regenerative braking control strategy in [42]. The braking force distribution lines are designed respectively for full load and no load cases. This control strategy can improve vehicle fuel economy and braking performance, but the vehicle load identification during braking is a challenge. It is considered in [28, 41, 43] that HPM torque is proportional to its

working pressure. So a minimum working pressure is guaranteed to provide adequate torque for regenerative braking.

Some studies have been completed to validate the fuel economy of PHHV. In [44], a typical driving circle is extracted from a conventional routine to research the energy efficiency of a refuse collection vehicle. Through simulation, 20% energy efficiency improvement is achieved compared to a conventional engine driving vehicle. In [29], tests are conducted where HPM is used for regenerative braking and launching. The PHHV energy benefits during an entire urban driving cycle are verified.

Compared with the massive researches on PHHV energy benefits, vibration of the PHHV powertrain is still under researched. Powertrain dynamic model is the foundation of vibration analysis. By establishing powertrain dynamic model and hydraulic components model, the source of vibration and the vibration transferring routine can be determined. Vertical vibration problems on vehicle chassis caused by hydraulic driving system are analyzed in [45, 46] and magnetorheological fluid mounts are adopted for vibration isolation. In [47], HPM toque is modelled in detail and the effect of piston numbers is analyzed. The frequency characteristics of HPM excitation are revealed in this paper. However, vehicle powertrain model is not built so the effect of HPM torque on vehicle powertrain vibration is not studied. HPM caused pressure pulsation is researched in [48]. Lower speed and bigger swashplate angle are recommended to reduce total noise and vibration. An accumulator model is built in [49] to investigate the pressure pulsations in hydraulic driving system. Accumulator can be used to reduce the pressure pulsation generated by HPM like a capacitor in the electric circuit. This research shows that more accumulators connected can reduce the system pressure pulsation while increasing accumulator volume seems ineffective. The pipe damping effect on hydraulic hybrid vehicle powertrain vibration is researched in [50]. The response time of accumulator under different temperature is researched in [51]. Results show that temperature can affect accumulator characteristics by changing the oil viscosity.

Current research on HEV powertrain vibration provides useful references to PHHV powertrain vibration research. A dynamic model of HEV is built in [52]. The frequency response of powertrain to engine excitation is analyzed. Different dual-mass flywheel inertia, stiffness and damping characteristics are compared in the model to find the parameters that cause the least vibration. Model reduction of a HEV powertrain is conducted in [53]. The simplified model is compared with the full order model. Results

show that the simplified model could correctly capture the powertrain low frequency vibration characteristics. In [54], a HEV powertrain is simplified as a two mass model to research the powertrain vibration caused by electric motor during vehicle launching. A 15 degree of freedom model and a simplified 4 degree of freedom model of a dual clutch transmission equipped powertrain are compared in [55]. Results show that the simplified model provides a reasonable representation of the detailed model, especially at lower natural frequencies. Experiments are conducted in [56] to validate the fidelity of a 3 degree of freedom powertrain model. Simulation results and experimental results show great consistency. In [57], only the driveshaft stiffness is considered and a two degree of freedom model is built for a power-split HEV. This model has less complexity while is still sufficient to research the powertrain vibration during rapid accelerating and decelerating. In [58], a HEV simulation model is built and validated by tests. Active torsional vibration control is used for vehicle launching and mode switching. Vehicle jerk is reduced remarkably with active control. A bus powertrain model is established in [59] by finite element method to research powertrain vibration during accelerating and gear shifting. It is concluded that the changing rate of driving torque and clutch torque should be restricted otherwise significant powertrain vibration could occur.

From above references, it could be found research on vehicle powertrain vibration is necessary and significant. Conventional engine driving vehicle and HEV powertrain modelling and vibration analysis have been deeply investigated. However, modelling and vibration analysis of PHHV powertrain have not been researched yet.

In PHHV, mode switching and gear shifting happen according to EMS. Torque coordinated control and speed control are required in these transient processes. No research on PHHV powertrain coordinated control could be found although it is important. These control strategies could only be designed referring to coordinated control in HEV. Control of vehicle launching [60, 61], mode switching [62, 63], gear shifting [64] and regenerative braking [65] of HEV has been investigated [66].

A hierarchical mode switching control strategy is proposed in [67, 68]. Robust controllers are designed for clutch target toque trajectory design and tracking. To reduce the effects of external disturbance and parameters perturbation, a robust control strategy is developed in [69]. In [70], model reference control is used to coordinately control the engine torque, clutch torque and motor torque. By choosing suitable controllers, benefits regarding to torque interruption, vehicle jerk and clutch frictional losses are gained compared to

conventional control strategies. The mode switching process is divided into four phases in [71], they are engine cranking phase, synchronization phase, clutch engagement phase and torque switching phase. Control strategies are designed for each phase. A disturbance observer is used to improve the control accuracy and tracking performance. Data-driven mode switching control strategy is proposed in [72]. The best advantage of the proposed control strategy is that accurate model is not necessary. In [73], model predictive control strategy is used for mode switching control. The object function is defined according to the requirements of suppressing vehicle jerk and clutch wear. In [74], engine cranking and ignition process are modelled in detail to investigate their impacts on powertrain vibration. In [75], the condition that the mode switching and gear shifting happen simultaneously is considered. The coordinated control strategy is designed to shorten the duration of this process.

In mode switching control, engine can be started by electric motor through clutch torque [76]. Clutch engagement brings vehicle jerk which affects the vehicle driving comfort. Clutch friction also leads to clutch wear which is represented by clutch frictional work. Vehicle jerk and clutch frictional work are conflict targets. Slow clutch engagement helps decrease vehicle jerk but increase clutch frictional work. Fast clutch engagement brings an opposite effect [77]. LQR control strategy is designed for clutch control to compromise vehicle jerk and clutch frictional work. Fast mode switching and slow mode switching can be achieved according to the driver intention. In [78], a feedforward-LQR feedback controller is adopted to improve the mode switching control performance. Nonlinearity, disturbance and parameter uncertainties are considered in HEV modelling. In [67], LQR control strategy is used for clutch torque control when starting engine.

PHHV is normally equipped with AMT, which makes it is inevitable to have torque interruption during gear shifting and thus vehicle dynamic performance and driving comfort are degraded [79]. In PHHV, power on gear shifting could be realized with the help of HPM to drive vehicle when engine torque is cut off. However, research on PHHV power on gear shifting are quite scarce. Meanwhile, AMT power on gear shifting in other applications is deeply researched. In [80], power on gear shifting of a parallel HEV is researched. The effectiveness of using an electric motor to compensate engine torque during gear shifting is validated by simulation. Parameter sensitivity analysis is conducted to investigate the torque compensation capability with different electric motor size. A flywheel is adopted as the secondary driving unit in [4]. During gear shifting, the flywheel

stored kinetic energy is used to drive vehicle so that torque gap is reduced. In [81], a two electric motor driving system is proposed. The primary motor drives vehicle via AMT and the second motor is installed on vehicle driveshaft and used to drive vehicle during gear shifting. Motor torque transfer control strategy is designed based on a modified bump function. In [82], an electric motor is integrated into AMT output shaft by a two speed epicyclical gear set to enlarge the electric motor torque compensation range. An assist clutch is used to replace the fifth gear synchronizer of AMT in [83]. In the revised transmission, the assist clutch helps to transfer engine torque during gear shifting so that torque interruption is solved.

To improve PHHV driving comfort and dynamic performance, it is worthy to research and design mode switching and power on gear shifting control strategies [84]. There are several specific characteristics of PHHV powertrain that should be considered when designing control strategies. Engine inertia is much larger in medium and heavy duty vehicles, which means the powertrain equivalent inertia notably changes with or without engine [85]. It potentially causes vibration to powertrain when engine clutch is engaged and disengaged, depending on vehicle acceleration. Besides, HPM torque is directly determined by its working pressure, which means the available HPM torque is restricted by accumulator pressure state [86]. Therefore, the HPM torque compensation capability under different accumulator pressure should also be investigated.

Accurate powertrain state parameters are the foundation of control. However, it is hard to measure the powertrain state parameters such as clutch speed and torque for technical or cost reasons [87]. For these measurable state parameters such as vehicle speed and acceleration, noise also affects measurement accuracy. To estimate the unmeasurable state parameters and reduce the measurement noise effect, various estimation algorithms have been proposed [88, 89]. In [90], a self-adaptive unscented Kalman filter is adopted to estimate vehicle speed. The estimation is based on wheel speed, vehicle acceleration and wheel braking torque which could be measured by sensors. In [91], a model based estimator is used to estimate vehicle mass. To conduct active vibration control, dual extended Kalman filter is used in [92] to estimate the driveshaft torsional angle and vehicle mass. Unscented Kalman filter algorithm is designed in [93] to estimate clutch torque. Experimental results verify that the proposed algorithm is capable of practical use. Engine torque estimation is researched in [94]. Through simulation and experiment, the proposed unknown input observer is demonstrated to be robust under sensor noise. The

unknown input observer is also used in [95] to estimate road bank and slope. Tyre resistant torque is affected by road roughness which is changing with different road conditions. In [96], road roughness is estimated by a discrete Kalman filter. In [97], a dual H infinity filter is designed for electric vehicle inertial parameters estimation. The convergence rate is verified by hardware-in-loop experiment, which proves the practicality of the estimator.

1.3 **Research objectives**

This research targets on improving the PHHV fuel economy, driving comfort and dynamic performance, which are presented as following in detail:

1) Propose a comprehensive PHHV hydraulic driving system parameter design method that could be used for different vehicle specifications and driving conditions.
2) Design PHHV EMS to properly coordinate engine driving system, hydraulic driving system and braking system during vehicle driving and braking.
3) Investigate the effect of hydraulic driving system on PHHV powertrain vibration characteristics.
4) Design mode switching and gear shifting control strategies to reduce powertrain vibration and increase vehicle dynamic performance and driving comfort during these transient processes.
5) Investigate the prospect of using HPM for in-wheel drive applications considering its high power density advantage.

1.4 **Contribution to the knowledge**

1) A comprehensive method is proposed for PHHV hydraulic driving system parameter design. It provides a completed process to select the hydraulic driving system parameters based on power analysis under different vehicle specifications and driving conditions.
2) A practical rule-based EMS is designed for PHHV including the driving torque allocation strategy, gear shifting schedule, regenerative braking control strategy. All of the vehicle fuel economy, vehicle dynamic performance and braking safety are considered.

3) For the first time, the impact of hydraulic driving system on PHHV powertrain vibration characteristics is researched. The change of powertrain natural frequencies and mode shapes are revealed. The HPM excitation is modelled and its impact on powertrain vibration is analyzed.
4) For the first time, PHHV mode switching and power on gear shifting is researched and control strategies are designed to improve vehicle driving comfort and dynamic performance during these transient process.
5) A novel in-wheel drive electric hydraulic hybrid vehicle (IHV) is proposed which takes the HPM high power density advantage. Its energy economy and vertical vibration characteristics are researched and compared with centralized motor drive electric vehicle (CEV) and in-wheel drive electric vehicle (IEV).

1.5 **Outline of thesis**

The remainder of this thesis is organized as following:
In chapter 2, PHHV powertrain structure is introduced and modelled to reveal its working principle. According to power analysis results based on the Chinese typical urban driving cycle (CTUDC), hydraulic driving system parameters are designed.
In chapter 3, the optimal PHHV fuel economy is investigated by DP optimization. Then a rule-based EMS is designed to improve the PHHV practicality, including driving torque allocation control strategy, gear shifting schedule and regenerative braking control strategy.
In chapter 4, PHHV powertrain vibration characteristics are researched and compared with the original engine driving vehicle. A 14 degree of freedom powertrain dynamic model is established based on the lumped parameter method and then simplified to a 6 degree of freedom model. The frequency response of PHHV powertrain under the engine excitation and HPM excitation is researched based on the simplified model.
In chapter 5, mode switching control strategy is designed. Distinctive characteristics of PHHV such as relatively slower HPM torque response and larger engine inertia are considered. Due to the low energy density of accumulator, hydraulic energy consumption is also considered during mode switching.
In chapter 6, power on gear shifting control strategy is designed to maintain vehicle dynamic performance and improve vehicle driving comfort during gear shifting. Extended Kalman filter (EKF) is adopted for powertrain state estimation to provide more

accurate state feedback for power on gear shifting control strategy as well as mode switching control strategy. HPM torque compensation capability is researched based on the designed gear shifting schedule and typical driving cycles.

In chapter 7, a novel IHV is proposed and its energy economy and vertical vibration characteristics are researched and compared with CEV and IEV. DP optimization is used to explore the optimal energy consumption of each vehicle. Their vertical vibration characteristics are researched with a simplified quarter vehicle dynamic model.

In chapter 8, main works of this thesis are concluded.

1.6 List of Publications

Journal papers

1. **S. Zhou**, P. Walker, J. Wu, and N. Zhang, "Power on gear shift control strategy design for a parallel hydraulic hybrid vehicle," *Mechanical Systems and Signal Processing*, vol. 159, p. 107798, 2021.
2. **S. Zhou**, P. Walker, Y. Tian, and N. Zhang, "Mode switching analysis and control for a parallel hydraulic hybrid vehicle," *Vehicle System Dynamics*, vol. 59, no. 6, pp. 928-948, 2021.
3. **S. Zhou**, P. Walker, Y. Tian, C. T. Nguyen, and N. Zhang, "Comparison on Energy Economy and Vibration Characteristics of Electric and Hydraulic in-Wheel Drive Vehicles," Energies, vol. 14, no. 8, p. 2290, 2021.
4. **S. Zhou**, P. Walker, B. Xiao, and N. Zhang, "Modelling and Vibration Analysis of a Parallel Hydraulic Hybrid Vehicle," *IEEE Transactions on Vehicular Technology*, vol. 69, no. 10, pp. 10710-10723, 2020.
5. **S. Zhou**, P. Walker, and N. Zhang, "Parametric design and regenerative braking control of a parallel hydraulic hybrid vehicle," Mechanism and Machine Theory, vol. 146, p. 103714, 2020.
6. **S. Zhou**, P. Walker, W. Yang, C. T. Nguyen, and N. Zhang, "Energy management strategy design and fuel consumption analysis for a parallel hydraulic hybrid vehicle," *International Journal of Heavy Vehicle Systems*, (Accepted for publication).

Conference papers

1. **S. Zhou**, P. Walker, N. Zhang, "Modelling and Vibration Characteristics Analysis of a Parallel Hydraulic Hybrid Vehicle," *in 18th Asia-Pacific Vibration Conference*, Sydney, Australia, 18-20, November, 2019.
2. **S. Zhou**, P. Walker, N. Zhang, "Modelling and control of mode switching process for parallel hydraulic hybrid vehicle," *in 2019 International Conference on Advanced Vehicle Powertrains*, Hefei, China, 25-27, August, 2019.
3. **S. Zhou**, P. Walker, Y. Tian, and N. Zhang, "Parameter Design of a Parallel Hydraulic Hybrid Vehicle Driving System Based on Regenerative Braking Control Strategy," *in SAE World Congress Experience*, Detroit, United States, 19-21, April, 2019.

Chapter 2 Powertrain modelling and parameter design

2.1 Introduction

PHHV powertrain structure is shown in Figure 2.1. Hydraulic driving system is added to the driveshaft of a conventional rear wheel driving vehicle. This modification does not change the original engine driving powertrain. Engine torque is transmitted to rear wheels via engine clutch, AMT, driveshaft, differential and halfshaft. HPM is the driving unit in hydraulic driving system. It could provide both positive torque and negative torque for vehicle driving and braking. HPA is used to store the energy recovered from regenerative braking by compressing the inert gas in it. LPA works as a reservoir and its pressure is much lower than HPA. HPM works under the pressure difference between HPA and LPA. A valve is used to control oil flow in the system. When hydraulic driving system works, valve is opened and oil could flow between HPA and LPA. When hydraulic driving system does not work, valve is closed and oil flow is prevented.

During vehicle launching and driving, HPM works as a motor and oil flows from HPA to LPA. By adjusting the swashplate angle and direction, positive torque is generated by HPM under the pressure difference to propel vehicle. During regenerative braking, HPM works as a pump and oil flows from LPA to HPA. Negative HPM torque is applied to vehicle. Braking energy is recovered and stored in HPA. HPM gear is adopted to adjust HPM torque and speed. HPM clutch is used to protect HPM from over-speed operations. When HPM speed reaches its maximum working speed, HPM clutch is disengaged.

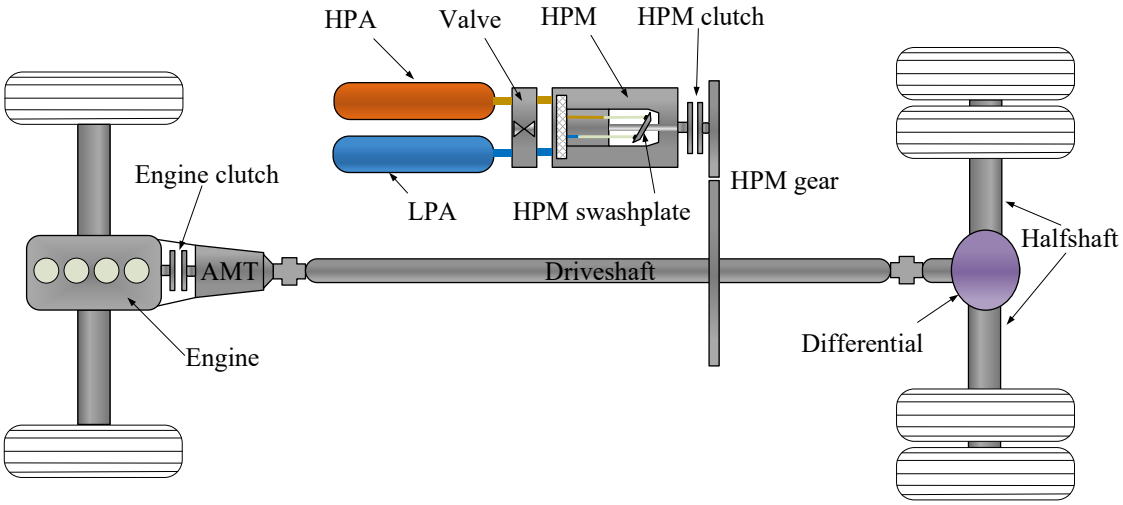

Figure 2.1. Structure of PHHV powertrain.

2.2 PHHV powertrain modelling

2.2.1 PHHV Powertrain modelling

PHHV is driven by engine and HPM individually or in combination. Engine and HPM torque is adjusted by AMT, HPM gear and main reducer, as described following:

$$\delta Ma = \left(T_e i_g i_f \eta_e + T_h i_h i_f \eta_h - T_L - T_{bm}\right) / R_w \tag{2.1}$$

where δ is vehicle rotational inertia factor, M is vehicle mass, a is vehicle acceleration, T_e is engine torque, i_g is AMT gear ratio, i_f is main reducer gear ratio, η_e is engine powertrain efficiency, T_h is HPM torque, i_h is HPM gear ratio, η_h is hydraulic powertrain efficiency, T_L is vehicle resistant torque, T_{bm} is mechanical braking torque. R_w is tyre dynamic radius. Vehicle resistant torque is mainly caused by air resistance, slope resistance and rolling resistance:

$$T_L = \left(Mg\sin\left(\phi\right) + \frac{1}{2}\rho_{air} A_f C_D V^2 + Mgf_r \cos\left(\phi\right) \right) R_w \tag{2.2}$$

where g is gravitational acceleration, ϕ is road slope, ρ_{air} is air density, A_f is vehicle frontal area, C_D is air drag coefficient, V is vehicle speed, f_r is rolling resistance coefficient.

2.2.2 HPM modelling

Figure 2.2 illustrates HPM structure. In HPM, the valve plate divides the hydraulic circuit into high pressure circuit and low pressure circuit. When HPM shaft rotates, cylinders connect with high pressure circuit and low pressure circuit alternatively. High pressure cylinders are connected to HPA and low pressure cylinders are connected to LPA. The pressure difference between high pressure cylinders and low pressure cylinders generates torque on HPM shaft. The direction and value of HPM torque are controlled by adjusting the swashplate angle.

A three position four way proportional directional valve is adopted to control oil flow. Spool is kept at the regular position under the spring force without control. When a control current i_{sp} is added to solenoid, spool moves as following:

$$m_{sp}\ddot{x}_{sp} + c_{sp}\dot{x}_{sp} + k_{sp}x_{sp} = k_i i_{sp} \tag{2.3}$$

where m_{sp} is spool mass, x_{sp} is spool displacement, c_{sp} is spool damping, k_{sp} is spool spring stiffness, k_i is solenoid electromagnetic coefficient.

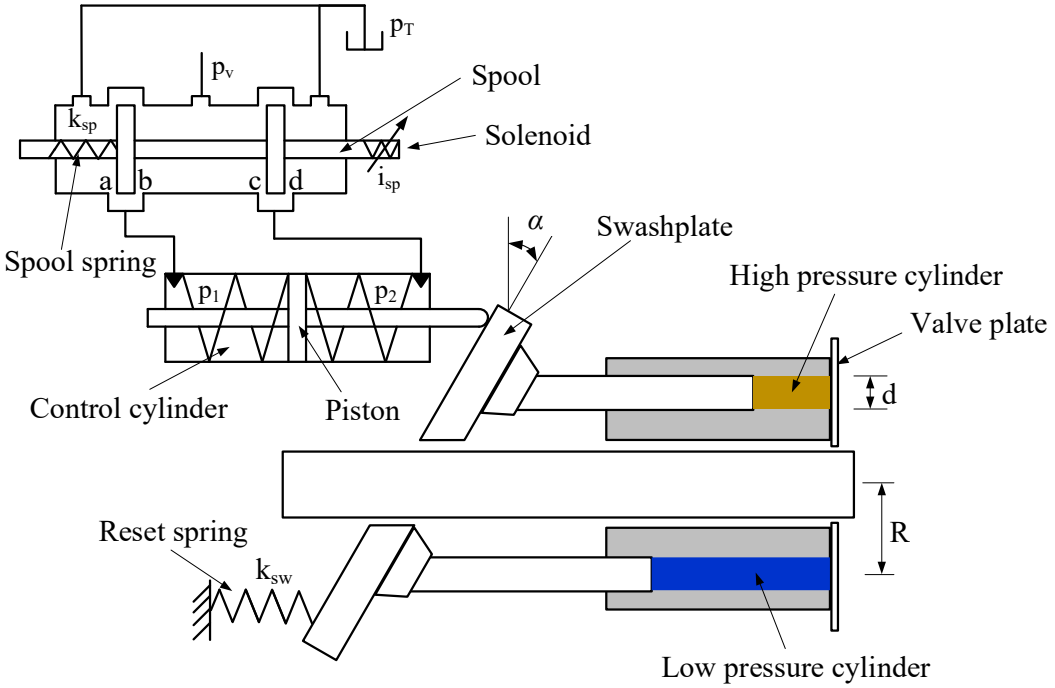

Figure 2.2. Structure of HPM.

Spool displacement controls oil flow through its four control gaps. Assuming constant discharge coefficient and neglecting the valve leakage, flow rates through the four control gaps can be described by equations:

$$Q_a = C_v w_v \left|x_{sp}\right| \varepsilon(x_{sp}) \sqrt{\frac{2\left|p_1 - p_T\right|}{\rho_c}} \operatorname{sgn}(p_1 - p_T) \tag{2.4}$$

$$Q_b = C_v w_v \left|x_{sp}\right| \varepsilon(-x_{sp}) \sqrt{\frac{2\left|p_v - p_1\right|}{\rho_c}} \operatorname{sgn}(p_v - p_1) \tag{2.5}$$

$$Q_c = C_v w_v \left|x_{sp}\right| \varepsilon(x_{sp}) \sqrt{\frac{2\left|p_v - p_2\right|}{\rho_c}} \operatorname{sgn}(p_v - p_2) \tag{2.6}$$

$$Q_d = C_v w_v \left|x_{sp}\right| \varepsilon(-x_{sp}) \sqrt{\frac{2\left|p_2 - p_T\right|}{\rho_c}} \operatorname{sgn}(p_2 - p_T) \tag{2.7}$$

where C_v is discharge rate, w_v is valve port width, $\varepsilon(x)$ is a function defined as: $\varepsilon(x) = 1$, when $x \geq 0$; $\varepsilon(x) = 0$, when $x < 0$; p_v is proportional valve pressure, p_1 and p_2 are pressure acting on the two sides of control cylinder piston, ρ_c is density of oil in control cylinder, p_T is tank pressure. p_1 and p_2 could be described by equation (2.8)

and equation (2.9). In control cylinder, the internal and external leakage is very small and can be neglected [98, 99].

$$p_1 = \frac{B}{V_1}\int (Q_b - Q_a - A_p\dot{x}_p - \frac{p_c}{R_L})dt \tag{2.8}$$

$$p_2 = \frac{B}{V_2}\int (Q_c - Q_d + A_p\dot{x}_p + \frac{p_c}{R_L})dt \tag{2.9}$$

where

$$p_c = p_1 - p_2 \tag{2.10}$$

$$V_1 = V_{1i} + A_p x_p \tag{2.11}$$

$$V_2 = V_{2i} - A_p x_p \tag{2.12}$$

where B is effective oil bulk modulus, V_1 and V_2 are volumes of the two sides of control cylinder piston, A_p is control cylinder piston cross sectional area, x_p is control cylinder piston displacement, p_c is the pressure difference between the two sides of control cylinder piston, R_L is leakage resistance, V_{1i} and V_{2i} are the initial volumes of the two sides of control cylinder piston.

Swashplate movement is represented by following equation:

$$J_{sw}\ddot{\alpha} = P_c A_p r_{sw} - k_{sw}\alpha - c_{sw}\dot{\alpha} + M_{sw} \tag{2.13}$$

where J_{sw} is the equivalent inertia of swashplate and control cylinder piston, α is swashplate angle, r_{sw} is the distance between swashplate rotating axle and control cylinder piston acting point, k_{sw} is equivalent reset spring stiffness, c_{sw} is equivalent swashplate damping, M_{sw} is pumping pistons lateral moment acting on swashplate.

HPM oil flow rate V_m and HPM torque T_h could be described by:

$$V_m = \frac{\pi d^2}{2} z_c R \tan\alpha \tag{2.14}$$

$$T_h = \begin{cases} \dfrac{V_m \Delta p}{2\pi}\eta_{mh} & \text{when HPM works as motor} \\ \dfrac{V_m \Delta p}{2\pi\eta_{mh}} & \text{when HPM works as pump} \end{cases} \tag{2.15}$$

Where where d is HPM cylinder diameter, z_c is HPM cylinder number, R is HPM cylinder pitch radius [99, 100], Δp is HPM working pressure which is the pressure

difference between HPA and LPA, η_{mh} is HPM mechanical efficiency which is mainly affected by HPM working pressure, speed and displacement.

2.2.3 **Accumulator modelling**

Accumulator layout is shown in Figure 2.3, here pressurized inert gas is contained in bladder. When oil flows into accumulator, bladder is compressed and inert gas pressure increases. When oil flows out of accumulator, bladder expands and inert gas pressure decreases. The energy stored in accumulator is described by equation (2.16). In this model, the compression and expansion process is considered as an adiabatic process [40]. So the thermal loss of accumulator is neglected as it is much less than the energy transferred in charging and discharging process.

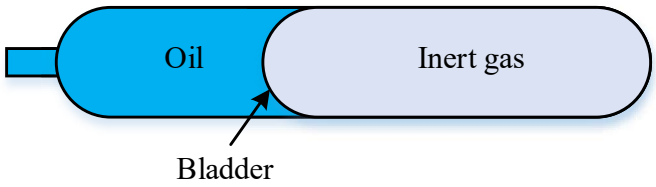

Figure 2.3. Layout of accumulator.

$$E_a = \frac{P_0 V_0}{k_a - 1}\left[\left(\frac{P}{P_0}\right)^{\frac{k_a - 1}{k_a}} - 1\right] \tag{2.16}$$

where E_a is the energy stored in accumulator, P_0 is accumulator pre-charged pressure, V_0 is inert gas volume under pressure P_0, k_a is inert gas ploy index and P is accumulator working pressure.

2.2.4 **Engine modelling**

Engine torque and fuel consumption are modelled as a lookup table, as shown in Figure 2.4. Engine fuel consumption is described by brake specific fuel consumption (BSFC). Smaller BSFC value indicates engine consumes less fuel to provide the same power, which also means vehicle gets better fuel economy.

During vehicle driving, engine torque is controlled by driver through throttle, as described by following equation:

$$T_e = \alpha_e T_{e\max}(n_e) \tag{2.17}$$

where α_e is engine throttle, $T_{e\max}(n_e)$ is the maximum engine torque at speed n_e.

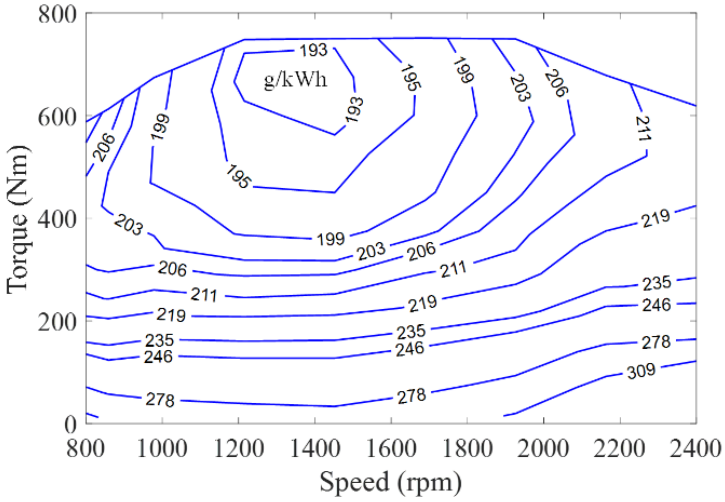

Figure 2.4. Engine BSFC map.

2.2.5 **Clutch modelling**

In PHHV, dry clutch is adopted to transmit engine torque and HPM torque. When clutch is disengaged, clutch torque is 0. When clutch is engaged, clutch torque is determined by engine and HPM torque. When clutch is slipping, clutch torque is determined by the normal force acting on clutch and the clutch structure parameters [101], which can be expressed by following equation:

$$T_{cl} = F_c N_c \mu_c R_c \operatorname{sgn}(\dot{\theta}_{c1} - \dot{\theta}_{c2}) \tag{2.18}$$

where T_{cl} is torque transmitted by clutch, F_c is the normal force acting on clutch. N_c is clutch frictional surface number. μ_c is clutch frictional coefficient, R_c is clutch disc equivalent radius, $\dot{\theta}_{c1}$ is clutch driving disc speed, $\dot{\theta}_{c2}$ is clutch driven disc speed.

2.3 **Hydraulic driving system parameter design**

HPM working efficiency is much affected by its working pressure, displacement and speed. However, most of the current research does not consider all of these factors. HPM working efficiency is only analysed based on one or two factors. Besides, accumulator parameters such as working pressure and gas volume have significant impacts on vehicle dynamic performance and fuel economy. However, its parameters are often selected intuitively or by simple calculations. An effective and practical method to find the most suitable hydraulic driving system parameters is necessary. Only with matched parameters, EMS will be able to fulfil its potential and the maximal PHHV fuel economy could be

attained. In this section, hydraulic driving system parameters are designed according to vehicle power analysis.

With high power density, hydraulic driving system gets more energy benefits in city used medium and heavy duty vehicles with frequent starting and braking [18, 102]. Therefore, a medium duty truck which is widely revised to refuse collection vehicle is selected as the original vehicle. Hydraulic driving system is added to its driveshaft to build a PHHV. The original vehicle parameters are shown in Table 2.1. Hydraulic driving system parameters are designed based on the original vehicle parameters and the typical urban driving cycle CTUDC.

Table 2.1. Original vehicle parameters.

Symbol	Parameter	Value	Unit
M_G	Gross vehicle mass	10700	kg
M_C	Cab chassis mass	3300	kg
f_r	Road rolling resistance coefficient	0.018	-
A_J	Vehicle frontal area	5.63	m^2
C_D	Air drag coefficient	0.7	-
ρ_{air}	Air density	1.2255	kg/ m^3
R_w	Tyre dynamic radius	0.439	m
L	Wheelbase	4.06	m
i_J	Main reducer gear ratio	4.55	-
i_g	AMT gear ratio	$1^{st}=6.62$, $2^{nd}=4.1$ $3^{rd}=2.36$, $4^{th}=1.53$ $5^{th}=1$, $6^{th}=0.72$	-

2.3.1 **HPM parameter design**

To find suitable HPM parameters, power analysis is necessary to obtain the vehicle torque demand and power demand during normal urban working conditions. As mentioned before, hydraulic driving system helps reduce fuel consumption by recovering braking energy and reusing the recovered energy for vehicle launching and driving, as such these platforms attain more energy benefits with working conditions that require frequent braking and launching. The typical urban driving cycle CTUDC is selected as a

representative of PHHV urban working conditions. The profile of CTUDC is shown in Figure 2.5.

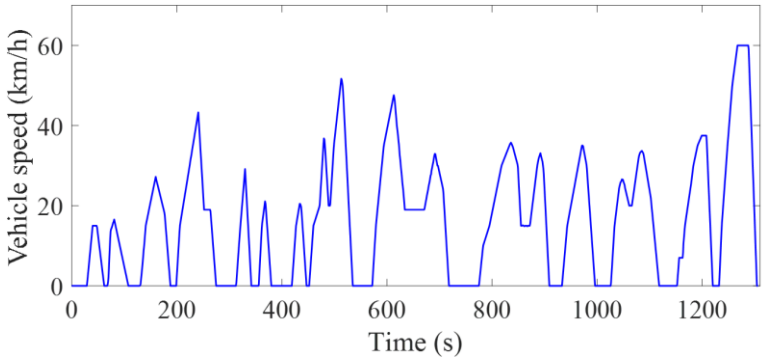

Figure 2.5. Profile of CTUDC.

Power analysis is conducted with half load condition in which vehicle mass is 7000 kg. The wheel torque demand and power demand of PHHV during CTUDC are shown in Figure 2.6. It could be found at most of the time, PHHV power demand is lower than 100 kW. However, torque demand is quite high during acceleration and deceleration events.

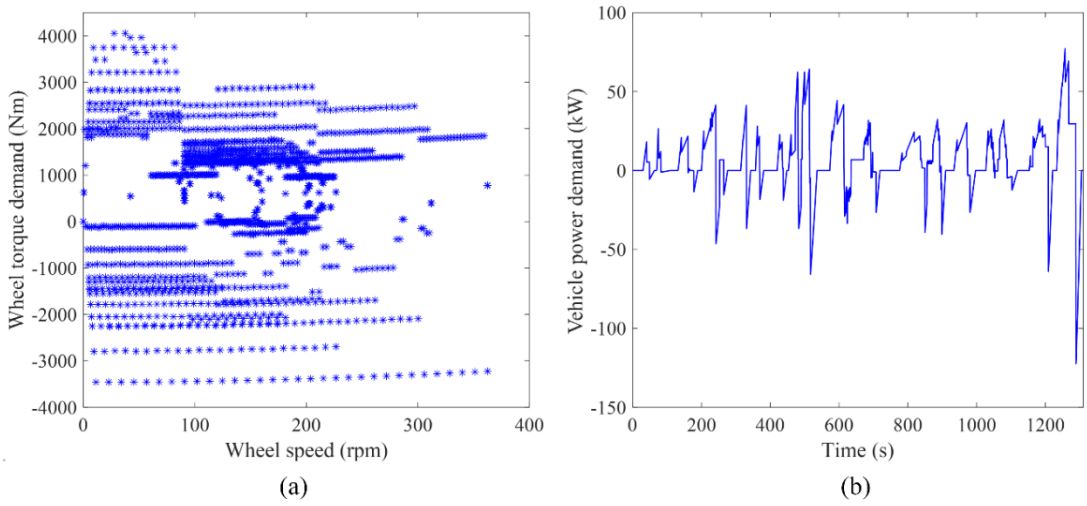

Figure 2.6. PHHV power analysis results.

In PHHV powertrain, only one gear is adopted to reduce the system complexity, which restricts the ability to adjust HPM torque. Furthermore, HPM torque is proportional to its working pressure as described in equation (2.15). Working pressure varies a lot as oil flows into and out of HPA. So HPM should be chosen with oversized displacement and power than is required by power analysis to guarantee the torque availability under lower working pressure conditions. A HPM on the market is selected and its parameters are shown in Table 2.2. HPM efficiency with 20%, 60% and 100% of its maximum

displacement is shown in Figure 2.7. HPM gear ratio is designed as 2 to coordinate with vehicle speed.

Table 2.2. HPM parameters.

Parameter	Value	Unit
Maximum displacement	107	cm^3/rev
Nominal working pressure	40	MPa
Peak working pressure	45	MPa
Maximum operating speed	3550	rpm
Maximum output torque	681	Nm
Maximum power	253	kW
HPM gear ratio	2	-

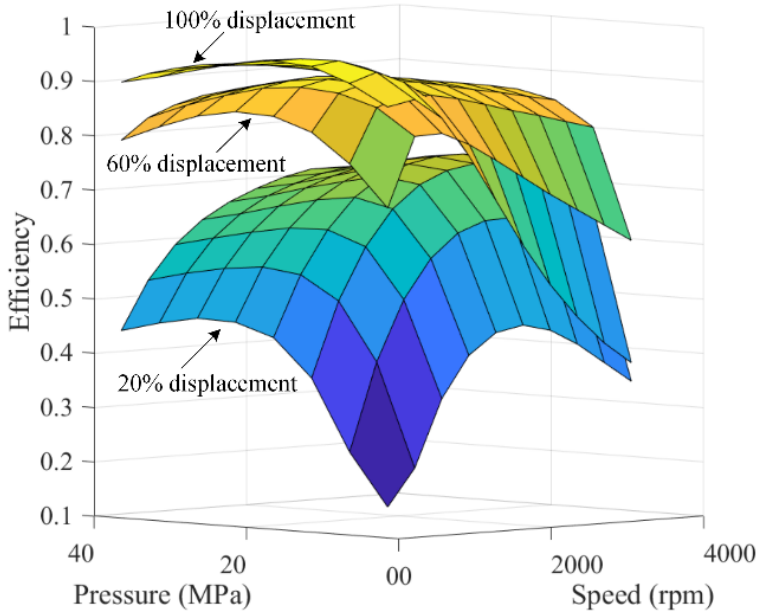

Figure 2.7. HPM efficiency maps.

2.3.2 **Accumulator parameter design**

From Figure 2.7, it is shown that HPM efficiency varies a lot under different working pressure, speed and displacement, so suitable accumulator parameters should be selected to maximize HPM dynamic performance and minimize losses. The parameters include accumulator gas volume and working pressure. In hydraulic driving system, LPA is only used to store oil. So it is only charged with a low pressure to prevent HPM cavitation [26, 103]. For HPA, there are two parameters needed to be designed: the minimum working

pressure and the corresponding inert gas volume at the minimum pressure. These parameters affect HPM working efficiency and PHHV fuel economy. So PHHV fuel consumption with different minimum HPA working pressure and corresponding gas volume at this pressure are investigated. Results are shown in Figure 2.8. It could be found that PHHV minimizes its fuel consumption if the minimum working pressure is between 10 MPa to 18 MPa. This pressure is the high efficiency region of HPM, as shown in Figure 2.7.

At the same minimum working pressure, when gas volume increases, PHHV fuel consumption decreases. The reason is that with larger gas volume, HPA pressure could be more stable at the HPM high efficiency region. However, larger gas volume requires larger accumulator installation space and increases accumulator cost, which are drawbacks for PHHV application and commercialization. Besides, higher HPA working pressure provides higher HPM torque, which improves vehicle dynamic performance and is especially important during regenerative braking in reducing the use of mechanical braking components. Equation (2.15) demonstrates that HPM torque is proportional to its working pressure. When HPA energy is used up for vehicle launching and driving, HPA is normally with its minimum pressure when braking starts. To provide adequate torque for regenerative braking, a certain HPA minimum pressure should also be maintained.

By compromising the accumulator size, PHHV fuel economy and regenerative braking requirement, the minimum HPA working pressure is chosen as 17 MPa, and the corresponding gas volume at this pressure is 70 L.

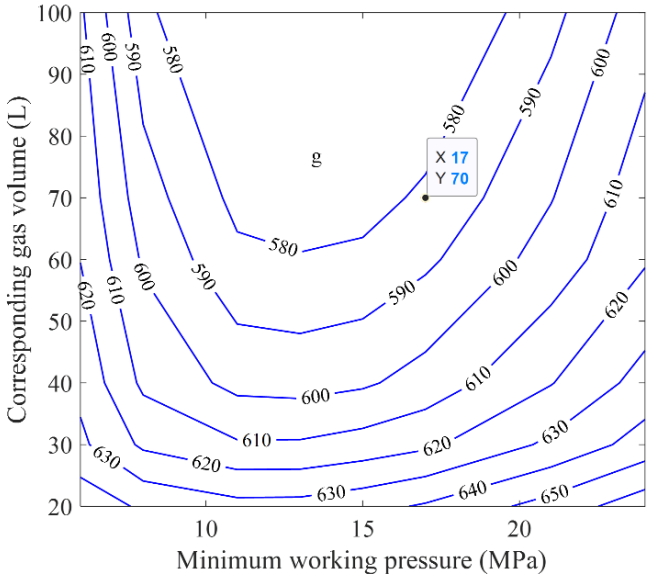

Figure 2.8. PHHV fuel consumption during CTUDC with different HPA parameters.

2.4 **Summary**

In this chapter, PHHV powertrain structure and working principle are introduced with the modelling of powertrain components. Hydraulic driving system parameters are designed through vehicle power analysis based on the typical urban driving cycle CTUDC. During parameter design process, all of the HPM working pressure, displacement and speed which affect HPM efficiency are considered. The designed parameters include HPM size, HPM gear ratio, HPA minimum working pressure and corresponding gas volume at this pressure. Vehicle dynamic performance, fuel economy, manufacturing cost and installation space are compromised during parameter selection.

Chapter 3 Energy management strategy design

3.1 Introduction

Among various PHHV EMS, rule-based EMS is practical and widely used. Rule-based control strategy is normally designed according to powertrain parameters and vehicle working conditions, such as energy storage efficiency map, power source torque characteristics, transmission gear ratio, driver torque demand and vehicle speed. Because the rules are designed ahead, their effect is limited when vehicle works in various conditions. The global optimization control strategy could achieve the maximum energy efficiency towards a known driving cycle. However, vehicle routine is hard to be known in advance. Therefore, global optimization is not suitable for practical applications. Global optimization is often conducted through DP optimization and the results are used as benchmark to evaluate the effects of other EMS [104-106].

To investigate the maximal PHHV fuel economy potential, DP optimization is firstly adopted in this section. Then, based on the DP optimization results, a rule-based EMS is designed and evaluated.

3.2 PHHV fuel consumption analysis based on DP optimization

In this research, the target of DP optimization is to minimize the PHHV fuel consumption during CTUDC, as described by following equation:

$$j = \sum_{n=0}^{N-1} L\left(X(n), U(n)\right) + \gamma\left(P_{h\_N} - P_{h\_0}\right) \tag{3.1}$$

where j is cost function to be minimized. N is DP optimization steps, X is the state variable which is HPA pressure. U are the control variables including HPM displacement and AMT gear. $L\left(X,U\right)$ is PHHV instantaneous fuel consumption determined by X and U. $\gamma\left(P_{h\_N} - P_{h\_0}\right)$ is a penalty function to restrict the final HPA pressure to be consistent with its initial pressure , where γ is penalty factor, P_h is HPA pressure.

State variable at step $n+1$ is determined by the state variable and the control variables at step n, which is described as following:

$$X(n+1) = f\left(X(n), U(n)\right) \tag{3.2}$$

The minimum fuel consumption could be obtained by solving the following recursive equations:

For (*N*-1)-th step:

$$j(N-1)=\min_{U(N-1)}\left(L\left(X(N-1),U(N-1)\right)+\gamma\left(P_{h\_N}-P_{h\_0}\right)\right) \tag{3.3}$$

For n-th $\left(0\le n<N-1\right)$ step:

$$j(n)=\min_{U(n)}\left(L\left(X(n),U(n)\right)+j(n+1)\right) \tag{3.4}$$

where $j(N-1)$ is the minimum fuel consumption at step *N*-1 when the control variables $U(N-1)$ are applied on the state variable $X(N-1)$. $j(n)$ is the minimum fuel consumption from *n*-th step to (*N*-1)-th step.

There are constraints on the state variable and the control variables which are determined by PHHV powertrain components physical characteristics. These constraints should be satisfied at all the time:

$$\begin{aligned}
&V_{m_\min}\le V_m\le V_{m_\max}\\
&P_{h_\min}\le P_h\le P_{h_\max}\\
&n_{e_\min}\le n_e\le n_{e_\max}\\
&T_{e_\min}\le T_e\le T_{e_\max}\\
&n_{h_\min}\le n_h\le n_{h_\max}\\
&T_{h_\min}\le T_h\le T_{h_\max}
\end{aligned} \tag{3.5}$$

where n_h is HPM speed.

Based on DP optimization, PHHV fuel consumption during CTUDC is obtained as shown in Figure 3.1. As a comparison, fuel consumption of original vehicle is also calculated by DP optimization and shown in Figure 3.1. Original vehicle is the vehicle PHHV refitted from, so it has the same parameters as PHHV. Results show that fuel consumption is 776.4 g in original vehicle and 563.2 g in PHHV, indicating a fuel consumption reduction of 27.5%.

PHHV working mode during CTUDC is obtained by analyzing engine torque and HPM torque at each step, as shown in Figure 3.2. It is illustrated that engine driving accounts for most of the vehicle driving. Hybrid driving mostly happens with small engine torque. At these points, HPM is the main driving unit. Although engine charging accounts for 21.7% of all working modes, it could be found that most of the engine charging mode happens with small engine torque. In these scenarios, HPM provides negative torque to

recover braking energy and engine torque is used to adjust HPM torque to high efficiency area.

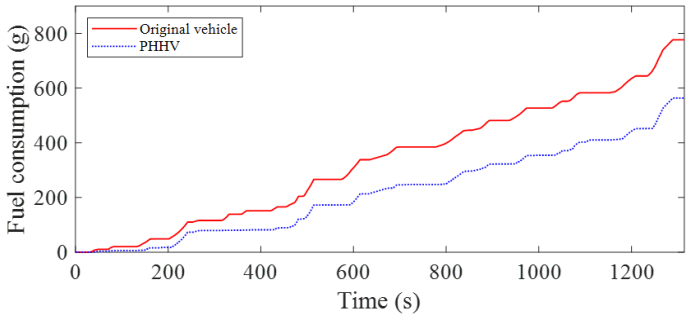

Figure 3.1. Fuel consumption of PHHV and original vehicle.

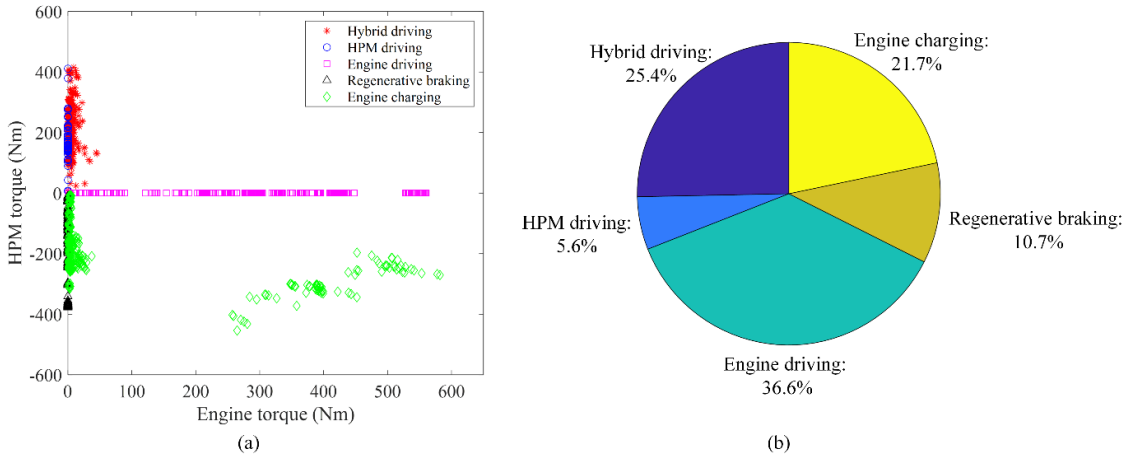

Figure 3.2. PHHV driving mode obtained by DP optimization, (a) Engine torque and HPM torque, (b) Percentage of each driving mode.

3.3 **Rule-based EMS design**

3.3.1 **Driving torque allocation strategy design**

The optimal PHHV fuel economy potential is obtained by DP optimization. However, DP optimization is a global optimization method and requires prior knowledge of the driving condition which is hard to be satisfied in real applications. So a practical rule-based EMS is designed based on DP optimization results.

Due to low energy density of accumulator, engine is not used to charge HPA to reserve its space for regenerative braking. During vehicle launching and driving, HPM functions independently if it can meet the driver torque demand. When HPM torque doesn't satisfy the driver torque demand, engine is used to drive vehicle together with HPM. If HPA energy is used up, HPM doesn't work and only engine drives vehicle.

3.3.2 **Regenerative braking control strategy design**

During braking, braking force is composed of mechanical braking force provided by braking discs and regenerative braking force provided by HPM:

$$\begin{cases} F_b = F_{bf} + F_{br} \\ F_{br} = F_{brm} + F_{brh} \end{cases} \tag{3.6}$$

where F_b is total braking force, F_{bf} is front wheel braking force which is all provided by mechanical braking, F_{br} is rear wheel braking force, F_{brm} is rear wheel mechanical braking force, F_{brh} is hydraulic regenerative braking force.

The maximum available braking force is determined by vertical wheel load and the road adhesion coefficient:

$$F_{b\max} = \varphi F_z \tag{3.7}$$

where $F_{b\max}$ is the maximum available braking force. F_z is vertical wheel load, φ is road adhesion coefficient.

When braking force is greater than the maximum available braking force, wheel will be locked. Front vertical wheel load and rear vertical wheel load during braking is:

$$\begin{cases} F_{zf} = G(L_b + zH_g)/L \\ F_{zr} = G(L_a - zH_g)/L \\ F_{bf\max} = \varphi F_{zf} \\ F_{br\max} = \varphi F_{zr} \end{cases} \tag{3.8}$$

where F_{zf} is front wheel vertical load, F_{zr} is rear wheel vertical load, $F_{bf\max}$ is the maximum available front wheel braking force, $F_{br\max}$ is the maximum available rear wheel braking force, G is vehicle gravity, L_b is the distance between vehicle center of gravity and rear axle, L_a is the distance between vehicle center of gravity and front axle, H_g is the height of vehicle center of gravity, L is wheelbase, z is braking intensity which is defined as:

$$\frac{dV}{dt} = zg \tag{3.9}$$

When front wheels and rear wheels lock up simultaneously, the braking intensity is equal to the road adhesion coefficient. That is $z = \varphi$ and equation (3.10) can be derived from equation (3.8).

$$\begin{cases} F_{bf} = \varphi G\left(L_b + \varphi H_g\right)/L \\ F_{br} = \varphi G\left(L_a - \varphi H_g\right)/L \end{cases} \tag{3.10}$$

By eliminating φ, the relationship between F_{bf} and F_{br} is described by equation (3.11) and shown as I curve in Figure 3.3.

$$F_{br} = \frac{1}{2}\left[\frac{G}{H_g}\sqrt{L_b^2 + \frac{4H_g L}{G}F_{bf}} - \left(\frac{GL_b}{H_g} + 2F_{bf}\right)\right] \tag{3.11}$$

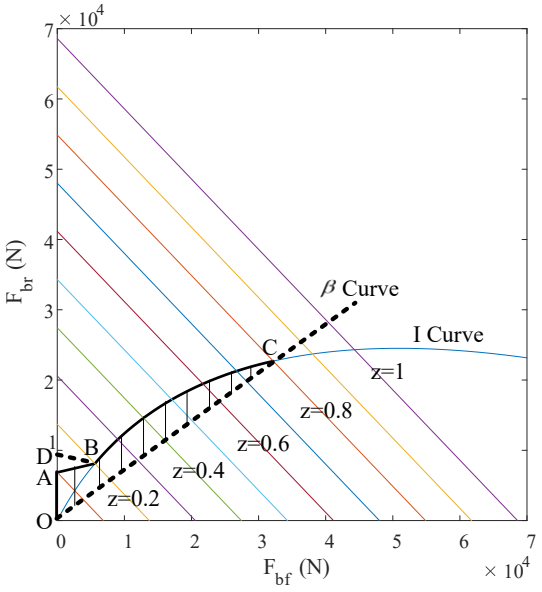

Figure 3.3. Regenerative braking control strategy.

PHHV is a rear wheel driving vehicle. To recover more braking energy, braking force should be allocated to rear wheels as much as it can be without compromising vehicle safety and HPM should be the first option to provide rear wheel braking force. However, if rear wheels are locked before front wheels, vehicle will be in unstable state [107]. That is to say, the braking force distribution line should not be above the I curve in Figure 3.3 generally.

When braking intensity is much less than road adhesion coefficient, braking force could be all allocated to rear wheels without causing wheel lockup. This braking control strategy c increase the braking energy recovery rate [108]. To guarantee adequate braking safety redundancy, a 0.2 road adhesion coefficient is chosen as the boundary to which over hydraulic regenerative braking force could be applied. This is equivalent to operating on low adhesion surfaces such as snow or ice covered roads. The rear wheel lockup curve with 0.2 road adhesion coefficient is shown as line BD in Figure 3.3.

Considering braking safety and braking energy recovery rate, when braking intensity is less than 0.1, braking force is all provided by HPM, shown as line OA in Figure 3.3.

On medium and heavy duty vehicles, the ratio of mechanical braking force between front and rear wheels is normally fixed, shown as the β curve in Figure 3.3.

When braking intensity is higher than 0.2, braking force is distributed to front wheels and rear wheels according to the I curve, which is shown as curve BC in Figure 3.3. In this scenario, front braking force is all provided by mechanical braking. Rear mechanical braking force is determined by front wheel braking force according to the β curve. HPM regenerative braking force compensates for the rest rear braking force between I curve and β curve.

When braking intensity is within 0.1 to 0.2, braking force is distributed along the line AB. Rear wheel mechanical braking force is determined by the β curve and HPM regenerative braking force compensates for the rest rear braking force between I curve and β curve.

When braking intensity is greater than 0.8, only mechanical braking is used for the sake of braking safety. Regenerative braking force is 0 and mechanical braking force is allocated according to the β curve.

Regenerative braking control strategy is shown in Figure 3.3 and also described by equation (3.12) to equation (3.15).

OA: z≤0.1, sole hydraulic regenerative braking:

$$\begin{cases} F_{bf} = 0 \\ F_{brm} = 0 \\ F_{brh} = F_b \end{cases} \tag{3.12}$$

AB: 0.1< z ≤0.2, blended mechanical and hydraulic regenerative braking:

$$\begin{cases} F_{bf} = \dfrac{2(z-0.1)(L_b + 0.2H_g)G}{L} \\ F_{brm} = \dfrac{1-\beta}{\beta} F_{bf} \\ F_{brh} = zG - F_{bf} - F_{brm} \end{cases} \tag{3.13}$$

BC: 0.2< z ≤0.8, blended mechanical and hydraulic regenerative braking:

$$\begin{cases} F_{bf} = z\dfrac{G}{L}\left(L_b + zH_g\right) \\ F_{brm} = \dfrac{1-\beta}{\beta}F_{bf} \\ F_{brh} = z\dfrac{G}{L}\left(L_a - zH_g\right) - F_{brm} \end{cases} \tag{3.14}$$

After C: z>0.8, sole mechanical braking:

$$\begin{cases} F_{bf} = \beta zG \\ F_{brm} = (1-\beta)zg \\ F_{brh} = 0 \end{cases} \tag{3.15}$$

According to the proposed regenerative braking control strategy, the regenerative braking force required for every braking intensity and the regenerative braking force ratio is shown in Figure 3.4. From Figure 3.4(a), the maximum required regenerative braking force is about 6860 N when braking intensity is 0.1.

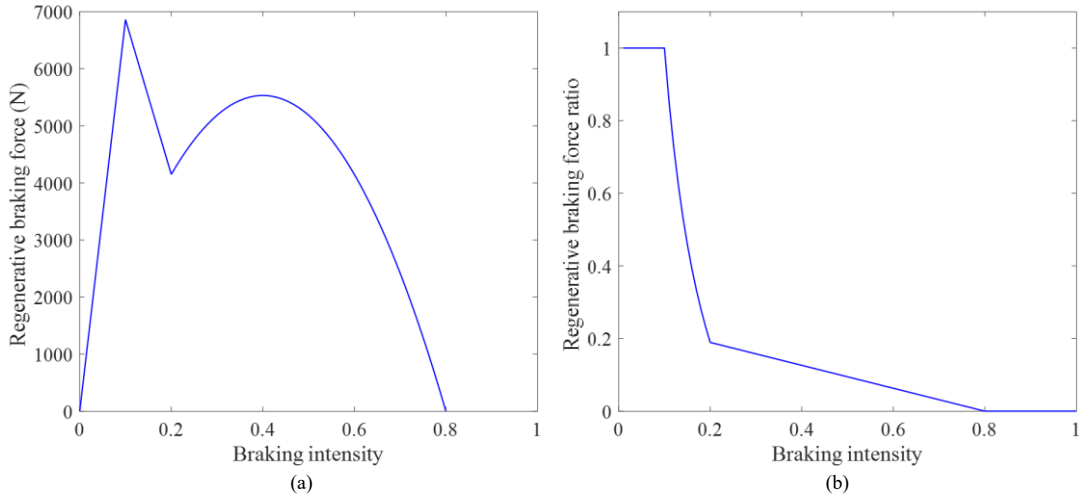

Figure 3.4. (a) Required regenerative braking force against braking intensity, (b) Regenerative braking force ratio against braking intensity.

The rule-based driving torque allocation strategy and regenerative braking control strategy is shown in Figure 3.5. In Figure 3.5, T_{dri} is the driver torque demand.

3.4 **Gear shifting schedule design**

Engine torque is adjusted by AMT to satisfy a larger range of vehicle speed and driver torque demand. Under certain vehicle speed and torque demand, vehicle could work with different gears with which engine has different working points, determined by gear

shifting schedule. Vehicle dynamic performance and fuel economy are greatly affected by gear shifting schedule.

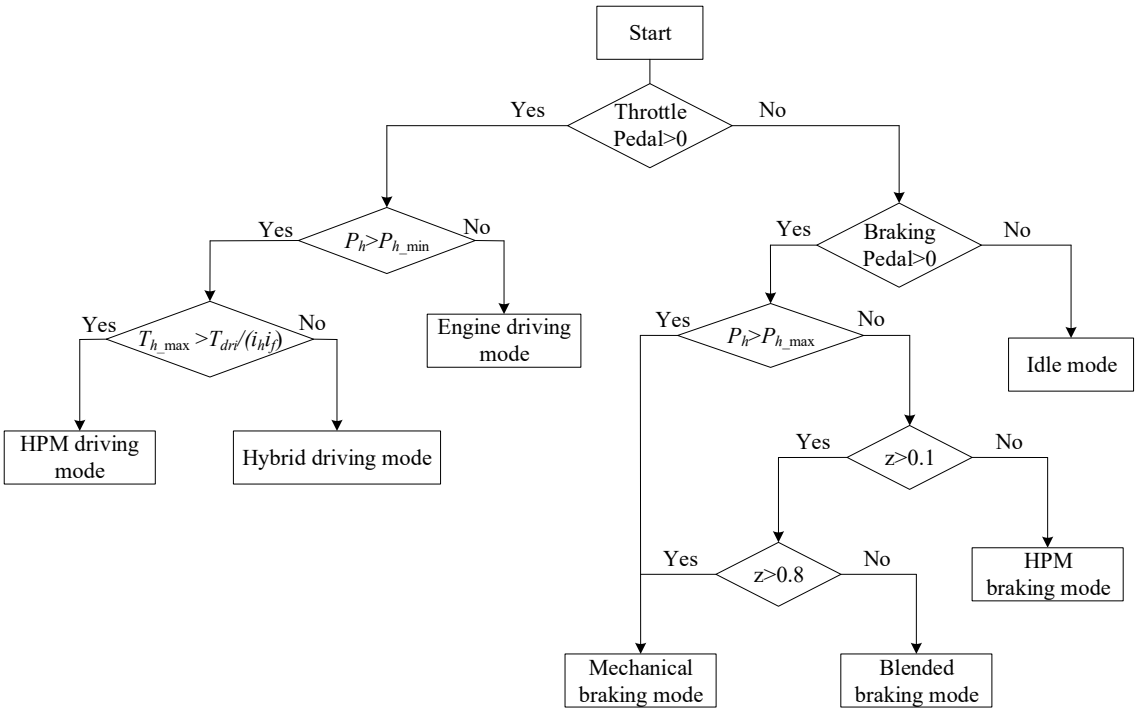

Figure 3.5. Rule-based driving torque allocation and regenerative braking control strategy.

3.4.1 **Economic and dynamic gear shifting schedule design**

Economic gear shifting schedule is designed by comparing engine fuel consumption with different gears. As shown in Figure 3.6(a), the traction force lines of 1st gear and 2nd gear with different throttle are drawn. For a required traction force, the intersection of required traction force line and the 1st gear traction force line determines the throttle at different vehicle speed. For example, point 'a' denotes that if vehicle speed is 5.05 km/h with 1st gear, engine throttle should be 60% to provide 25000 N traction force. Vehicle speed and engine throttle are converted to engine speed and torque. Fuel consumption is determined by interpolation in engine BSFC map and illustrated in Figure 3.6(b). Repeat the same process for different vehicle speed, fuel consumption lines are attained for 1st gear and 2nd gear. Fuel consumption lines of 1st gear and 2nd gear intersect at point 'A'. If vehicle speed is lower than point 'A' vehicle speed, fuel consumption with 1st gear is lower than 2nd gear. If vehicle speed is higher than point 'A' vehicle speed, fuel consumption with 1st gear is higher than 2nd gear. So point 'A' is the gear shifting point of 25000 N traction force. With the same vehicle speed and traction force, engine throttle are different with

different gears, which are depicted as ‘A'’ and ‘A"’ in Figure 3.6(c). ‘A'’ determines the 1st gear to 2nd gear upshifting point and ‘A"’ determines the 2nd gear to 1st gear downshifting point. By adopting different traction force, gear shifting lines of 1st gear and 2nd gear are designed. Gear shifting lines of other gears are also designed in the same method. Figure 3.6(d) depicts the economic gear shifting schedule.

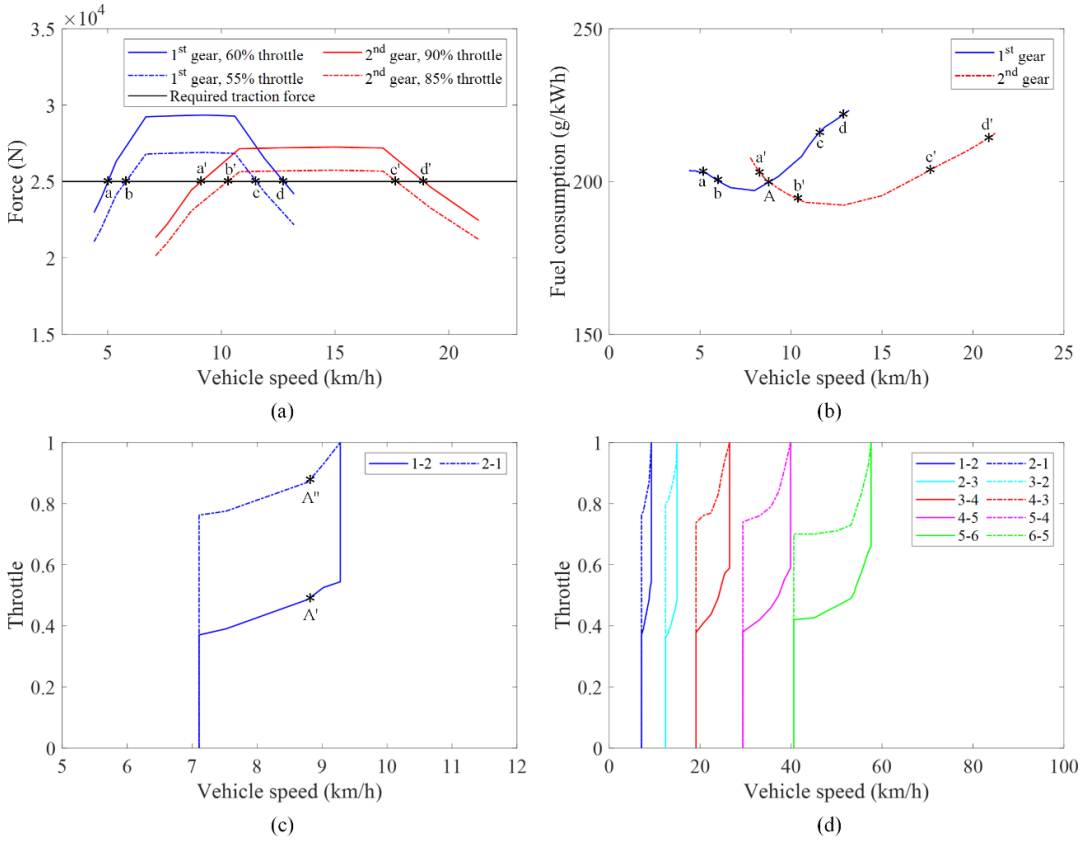

Figure 3.6. Economic gear shifting schedule.

Dynamic gear shifting schedule targets on providing maximal vehicle acceleration under each throttle. Vehicle acceleration is described by:

$$a = \frac{1}{\delta M R_w}\left(T_e i_g i_f \eta_e - T_L\right) \tag{3.16}$$

Gear shifting schedule between 1st gear and 2nd gear is introduced as an example of dynamic gear shifting schedule design. Under the same throttle, such as 20%, vehicle acceleration with 1st gear and 2nd gear are drawn respectively in Figure 3.7(a). Looking at a same vehicle speed, if vehicle acceleration with 1st gear is higher than 2nd gear, 1st gear should be used at this vehicle speed and engine throttle, and vice versa. The intersection of acceleration lines is the gear shifting point. If there is no intersection which means 1st gear acceleration is greater than 2nd gear acceleration at all speed, 1st gear should be used

until engine speed reaches its maximum limit. The same comparison is conducted with different throttle and the intersections are connected. The line is 1st gear and 2nd gear shifting line. In this research, 1st gear acceleration is always greater than 2nd gear acceleration, so gear shifting should be conducted at the maximum vehicle speed with 1st gear. Gear shifting schedules of other gears are designed with the same method which is shown in Figure 3.7(b). Figure 3.7(b) demonstrates that to achieve the best dynamic performance, vehicle should work with the lowest possible gears.

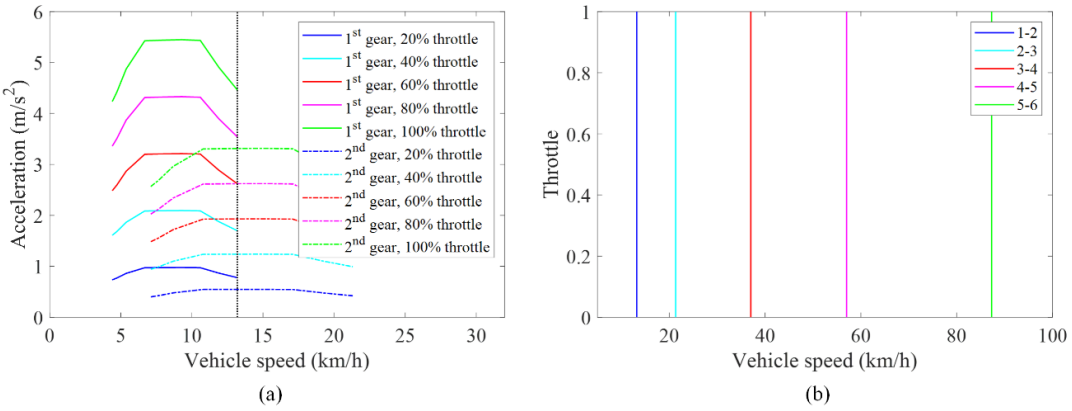

Figure 3.7. Dynamic gear shifting schedule.

Comparing economic and dynamic gear shifting schedules, dynamic gear shifting schedule tends to use lower gears which have larger gear ratios and provide higher driving torque. In contrast, economic gear shifting schedule tends to use higher gears at much lower vehicle speed, which saves fuel consumption but degrades vehicle dynamic performance.

3.4.2 **Gear shifting schedule design based on DP optimization**

In this section, gear shifting schedules are designed based on DP optimization results. The gear position distribution obtained by DP during CTUDC is categorized in Figure 3.8. It could be found that gear positions are mostly divided by vehicle speed at low throttle working condition. This indicates gear shifting schedule could be designed according to vehicle speed at low throttle. However, upshifting of higher gears are postponed at high throttle. It is because, at high throttle, more driving torque is required. Lower gears provide larger driving torque while higher gears couldn't provide enough torque. So upshifting needs to be delayed at high throttle to achieve better vehicle dynamic performance. A two parameters gear shifting schedule is designed based on above analysis, as shown in Figure 3.9. Comparing with economic and dynamic gear

shifting schedules, fuel economy is paid more attention to when throttle is small. At larger throttle which means higher traction force is demanded by driver, gear shifting is delayed to improve vehicle dynamic performance. So DP optimization based gear shifting schedule gets a balanced vehicle fuel economy and dynamic performance. The upshifting schedules are adjusted to offset the downshifting schedules to avoid excessive gear shifting [2, 109].

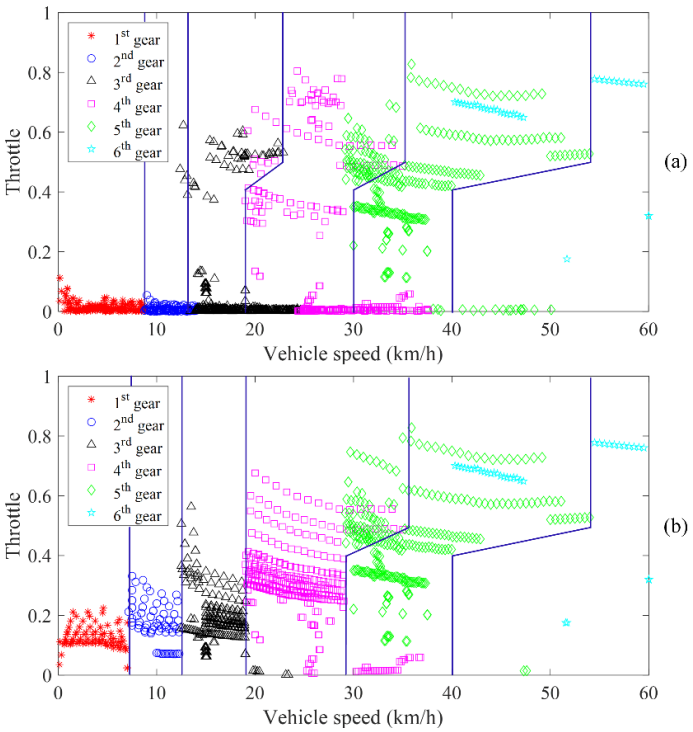

Figure 3.8. Gear position distribution obtained by DP, (a) PHHV, (b) Original vehicle.

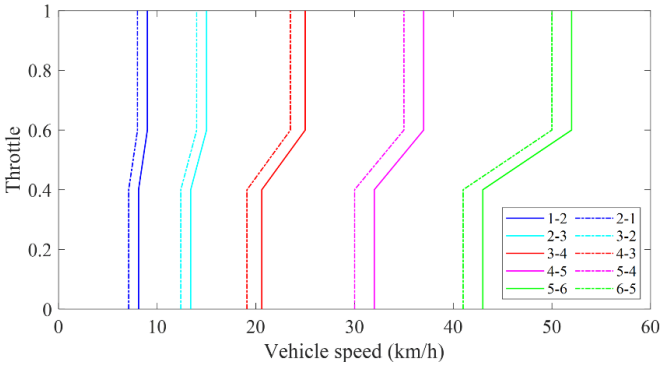

Figure 3.9. Gear shifting schedule based on DP optimization.

3.5 **PHHV fuel consumption analysis with rule-based EMS**

To verify PHHV fuel economy under the proposed rule-based EMS, a PHHV simulation model is built with Matlab/Simulink. An original vehicle simulation model is also built

as a comparison for PHHV. Through simulation, fuel consumption of PHHV and original vehicle during CTUDC with rule-based EMS is attained, as shown in Figure 3.10. It is shown that original vehicle consumes 787.3 g of fuel while PHHV consumes only 581.7 g of fuel.

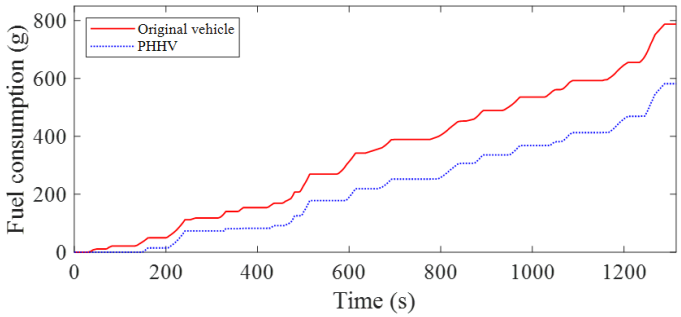

Figure 3.10. Comparison of fuel consumption during CTUDC.

HPA pressure during CTUDC is shown in Figure 3.11. The HPA end pressure is 36.42 MPa which is higher than its initial pressure of 30 MPa. It could be treated as HPA is charged by engine.

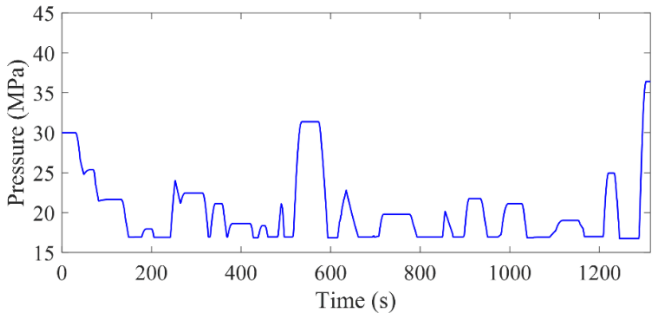

Figure 3.11. HPA pressure during CTUDC.

The energy stored in HPA is transformed into equivalent fuel saving so that PHHV fuel consumption is deducted. The equivalent fuel saving is calculated by following equation:

$$Equ\_fuel = E_{HPA} eff_{HPM} BSFC_{Eng} \tag{3.17}$$

where Equ_fuel is the equivalent fuel saving of the energy stored in HPA at the end of the driving cycle, E_{HPA} is the energy stored in HPA at the end of the driving cycle which is 0.0553 kWh from 30 MPa to 36.42 MPa. eff_{HPM} is the average HPM efficiency during the whole driving cycle which is calculated as 0.77. $BSFC_{Eng}$ is the average engine BSFC during the whole driving cycle which is calculated as 232.9 g/kWh. Finally, the energy stored in the HPA is equivalent to 9.9 g fuel saving.

The final fuel consumption of two vehicles is listed in Table 3.1. In PHHV, the equivalent fuel saving is deducted. It is demonstrated that PHHV could reduce fuel consumption by 27.4% with rule-based EMS. Comparing with DP results, PHHV fuel consumption is increased by 1.53%, which demonstrates that rule-based EMS attains both fuel economy and practicality. Original vehicle fuel consumption with rule-based EMS is very close to DP optimization, which demonstrates the gear shifting schedule extracted from DP optimization is effective and efficient.

Table 3.1. PHHV and original vehicle fuel consumption comparison.

	Original vehicle	PHHV	Reduction rate
Fuel consumption (DP) (g)	776.4	563.2	27.5%
Fuel consumption (Rule-based) (g)	787.3	571.8	27.4%

Figure 3.11 shows HPA pressure increases during braking and decreases during launching and driving. During the whole driving cycle, HPA pressure is less than the maximum working pressure of 40 MPa, which means HPA capacity is enough for these driving conditions. HPA mostly works between 17 MPa and 23 MPa, which is the high efficiency region of HPM. So HPM working efficiency is increased and PHHV fuel economy is improved.

Figure 3.12 shows PHHV and benchmark vehicle engine working points. It is found engine working points in PHHV is sparser than in original vehicle especially in the area between 50 Nm and 150 Nm, which means engine is less used in PHHV. The reason is that in PHHV, HPM is used for part of the vehicle launching and driving. But in original vehicle, engine has to drive vehicle all the time.

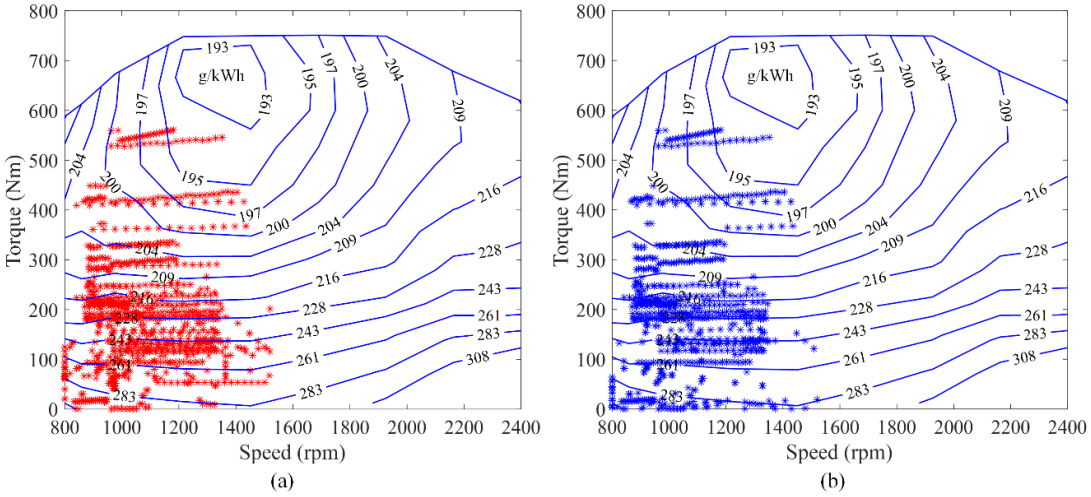

Figure 3.12. Engine working points, (a) Original vehicle, (b) PHHV.

Figure 3.13 shows the engine torque of PHHV and original vehicle during the whole driving cycle. It could also be found there are many times when engine in PHHV doesn't work while engine in original vehicle has to output torque to drive vehicle. It is shown in Figure 3.13 that in PHHV, engine is replaced by HPM to launch vehicle. During vehicle launching, engine speed is low where engine efficiency is relatively lower. So avoiding using engine to launch vehicle brings significant benefits to reduce fuel consumption.

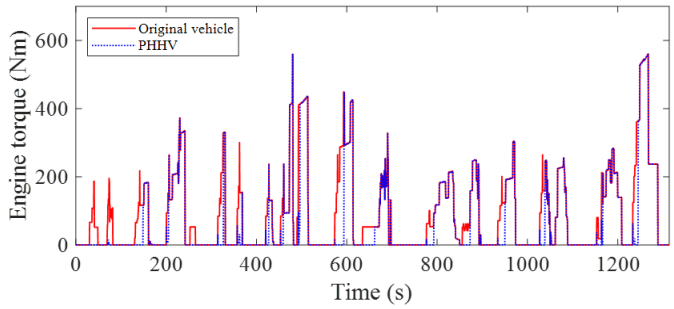

Figure 3.13. Engine torque during CTUDC by rule-based EMS.

HPM torque is shown in Figure 3.14. In Figure 3.14, positive HPM torque means HPM is used for vehicle launching and driving while negative HPM torque means HPM is used for regenerative braking. Figure 3.14 demonstrates that HPM torque is smaller than its maximum torque, which verifies that HPM satisfies vehicle torque and power demand. From HPM efficiency map, HPM has higher efficiency with higher displacement. So HPM should not be too much oversized otherwise it will work under smaller displacement with which it has relatively lower efficiency.

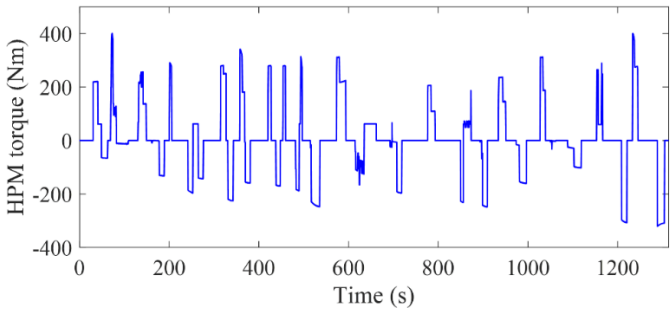

Figure 3.14. HPM torque during CTUDC.

As shown in Figure 3.15, HPM efficiency is higher than 0.75 most of the time. This illustrates that HPM works with proper pressure and displacement, verifying HPA parameters are suitable for this vehicle.

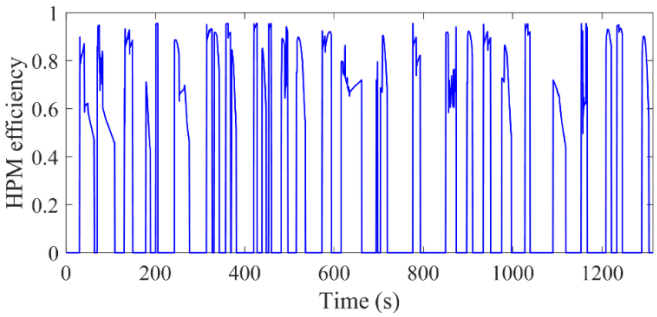

Figure 3.15. HPM working efficiency during CTUDC.

Gear position during the driving cycle is shown in Figure 3.16. It is demonstrated that excessive gear shifting is successfully avoided by the offset between downshifting and upshifting schedules.

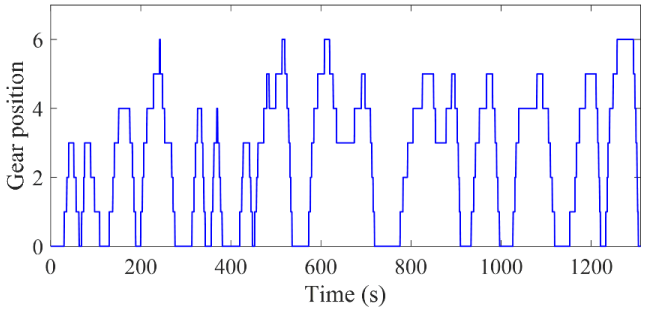

Figure 3.16. Gear position during CTUDC.

PHHV fuel consumption attained by rule-based EMS is slightly higher than DP optimization. The main reason is that the engine charging mode is cancelled in rule-based EMS. Besides, in DP optimization, braking force is provided by HPM as much as it can be to explore the optimal fuel economy. However, in practical rule-based EMS, braking safety and braking force allocation between front wheels and rear wheels are considered. Braking force allocation under rule-based EMS is shown in Figure 3.17. It is shown that mechanical braking is only used between 1289 s and 1305 s when PHHV decelerates from 60 km/h to 0 rapidly. During this period, braking intensity is greater than 0.1 so mechanical braking is included for safety consideration.

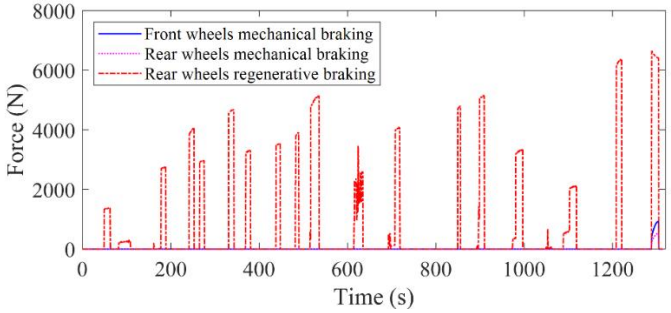

Figure 3.17. Braking force allocation by rule-based EMS.

Most of the braking energy is recovered by the designed regenerative braking control strategy as shown in Figure 3.18. The total kinetic energy generated in braking is 1.33 kWh and 1.03 kWh is recovered, indicating a recovering rate of 77.4%.

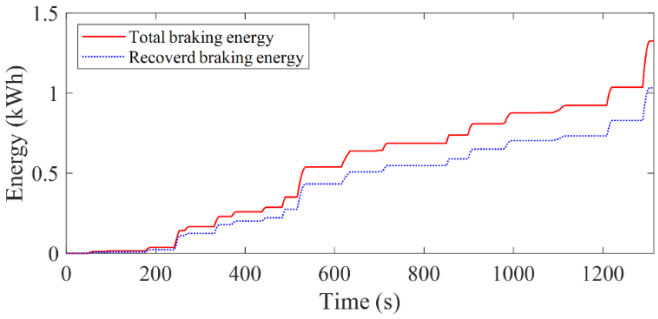

Figure 3.18. Regenerative braking results.

3.6 **PHHV fuel consumption analysis with different vehicle mass**

Hydraulic driving system parameters are selected based on half load condition with which vehicle mass is 7000 kg. From no load to full load conditions, vehicle mass varies from 3300 kg to 10700 kg. It is necessary to analyze PHHV fuel consumption under different vehicle mass. Figure 3.19 shows the fuel consumption comparison with different vehicle mass.

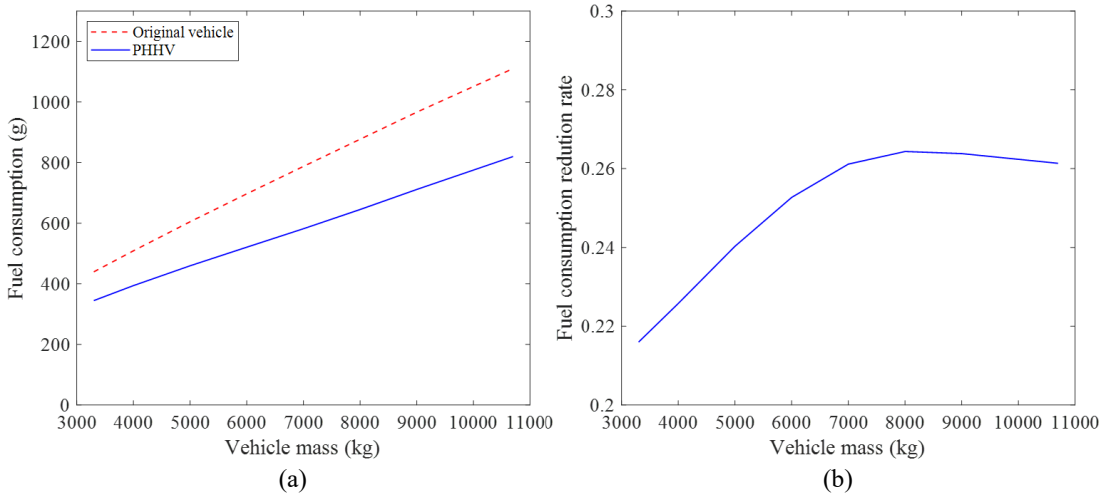

(a) (b)

Figure 3.19. Fuel consumption comparison with different vehicle mass

From Figure 3.19, PHHV gets good fuel economy from no load to full load conditions. It could be found at low vehicle mass, PHHV energy saving benefit is relatively lower. The reason is that with low vehicle mass, HPM is more likely to work with low displacement and low pressure with which the overall efficiency is relatively low. With large vehicle mass, PHHV energy saving benefit also decreases slightly. This is because more

hydraulic torque is required for regenerative braking for large vehicle mass. HPM is not able to provide enough braking torque so that mechanical braking takes more share of braking and the regenerative braking potential is not fully realized. Besides, with large vehicle mass, more braking energy is generated. When HPA is fully charged and can't do regenerative braking, braking energy is wasted by mechanical braking.

3.7 **Summary**

This chapter verifies PHHV fuel economy by DP optimization and rule-based EMS. With the designed hydraulic driving system parameters, PHHV has the potential to reduce fuel consumption by 27.5% compared with the original engine driving vehicle. Based on DP optimization results, practical rule-based EMS is designed including driving torque allocation strategy, regenerative braking control strategy and gear shifting schedule.

PHHV achieves better fuel economy than original vehicle by regenerative braking and reusing the recovered energy for vehicle driving. With HPM assisting driving, engine working time is reduced especially during vehicle launching with which engine efficiency is comparatively low. PHHV achieves good energy saving benefit across a complete range of load conditions. To achieve optimal fuel economy, hydraulic driving system should be carefully designed because HPM efficiency is greatly affected by its working pressure, speed and displacement. The distinctive characteristic of HPM that its torque is proportional to its working pressure is worthy of notice. Considering that, the minimum working pressure and gas volume of HPA should be optimized with the compromise of vehicle fuel economy, dynamic performance, mass and cost.

Chapter 4 Powertrain vibration analysis

4.1 Introduction

With the additional hydraulic driving system attached to vehicle driveshaft, the vehicle powertrain vibration characteristics are changed [46]. Besides, HPM also introduces extra excitation to vehicle powertrain [110]. Excessive vibration could degrade driving comfort and potentially cause damage to powertrain. So it is important to study the impact of hydraulic driving system on vehicle powertrain vibration characteristics to make sure the PHHV powertrain vibration is within the safe and comfortable region.

4.2 PHHV powertrain dynamic modelling

4.2.1 PHHV powertrain multi body dynamic model

PHHV could work under three driving modes with clutches engaged or disengaged. The working modes and corresponding clutch states are listed in Table 4.1.

Table 4.1. PHHV working mode.

Mode	Engine clutch state	HPM clutch state
HPM driving mode	Disengaged	Engaged
Engine driving mode	Engaged	Disengaged
Hybrid driving mode	Engaged	Engaged

To study PHHV powertrain vibration characteristics, a multi-body dynamic model is established as shown in Figure 4.1. In this model, engine clutch and HPM clutch are assumed to be in slipping state. PHHV powertrain is modelled as a free-free system and a linear time-invariant system. Compared with engine excitation and HPM excitation, the excitation from gear meshing is much smaller so ignored in modelling. The model is described by equation (4.1) to equation (4.16) [111].

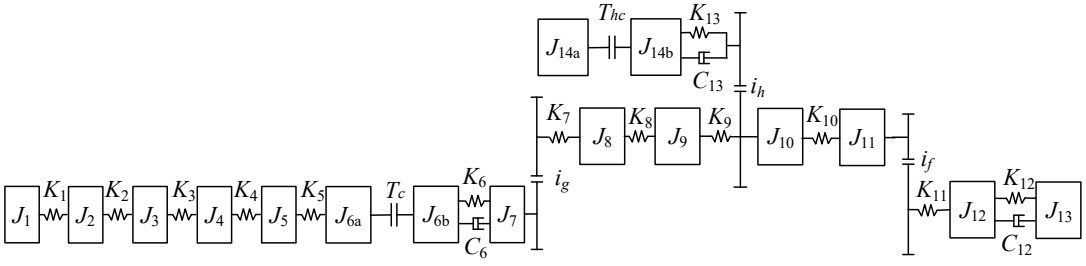

Figure 4.1. PHHV powertrain multi body dynamic model.

$$J_1\ddot{\theta}_1 = K_1(\theta_2 - \theta_1) \tag{4.1}$$

$$J_2\ddot{\theta}_2 = K_2(\theta_3 - \theta_2) - K_1(\theta_2 - \theta_1) \tag{4.2}$$

$$J_3\ddot{\theta}_3 = K_3(\theta_4 - \theta_3) - K_2(\theta_3 - \theta_2) \tag{4.3}$$

$$J_4\ddot{\theta}_4 = K_4(\theta_5 - \theta_4) - K_3(\theta_4 - \theta_3) \tag{4.4}$$

$$J_5\ddot{\theta}_5 = K_5(\theta_6 - \theta_5) - K_4(\theta_5 - \theta_4) \tag{4.5}$$

$$J_{6a}\ddot{\theta}_{6a} = T_c - K_5(\theta_{6a} - \theta_5) \tag{4.6}$$

$$J_{6b}\ddot{\theta}_{6b} = K_6(\theta_7 - \theta_{6b}) + C_6(\dot{\theta}_7 - \dot{\theta}_{6b}) - T_c \tag{4.7}$$

$$J_7\ddot{\theta}_7 = K_7(\theta_8 - \theta_7 / i_g) / i_g - K_6(\theta_7 - \theta_{6b}) - C_6(\dot{\theta}_7 - \dot{\theta}_{6b}) \tag{4.8}$$

$$J_8\ddot{\theta}_8 = K_8(\theta_9 - \theta_8) - K_7(\theta_8 - \theta_7 / i_g) \tag{4.9}$$

$$J_9\ddot{\theta}_9 = K_9(\theta_{10} - \theta_9) - K_8(\theta_9 - \theta_8) \tag{4.10}$$

$$J_{10}\ddot{\theta}_{10} = K_{10}(\theta_{11} - \theta_{10}) - K_9(\theta_{10} - \theta_9) - K_{13}(\theta_{10}i_h - \theta_{14b})i_h - C_{13}(\dot{\theta}_{10}i_h - \dot{\theta}_{14b})i_h \tag{4.11}$$

$$J_{11}\ddot{\theta}_{11} = K_{11}(\theta_{12} - \theta_{11} / i_f) / i_f - K_{10}(\theta_{11} - \theta_{10}) \tag{4.12}$$

$$J_{12}\ddot{\theta}_{12} = K_{12}(\theta_{13} - \theta_{12}) + C_{12}(\dot{\theta}_{13} - \dot{\theta}_{12}) - K_{11}(\theta_{12} - \theta_{11} / i_f) \tag{4.13}$$

$$J_{13}\ddot{\theta}_{13} = -K_{12}(\theta_{13} - \theta_{12}) - C_{12}(\dot{\theta}_{13} - \dot{\theta}_{12}) \tag{4.14}$$

$$J_{14a}\ddot{\theta}_{14a} = T_{hc} \tag{4.15}$$

$$J_{14b}\ddot{\theta}_{14b} = K_{13}(\theta_{10}i_h - \theta_{14b}) + C_{13}(\dot{\theta}_{10}i_h - \dot{\theta}_{14b}) - T_{hc} \tag{4.16}$$

In the equations, J, K and C indicate inertia, stiffness and damping of powertrain components. Their descriptions and values are shown in Table 4.2. θ indicates the angular displacement of each inertia, T_c is engine clutch torque, T_{hc} is HPM clutch torque.

4.2.2 **Engine transient torque modelling**

Engine has many parts including reciprocating pistons and conrods and its working condition is very complicated. It is difficult to exactly describe engine transient torque. Therefore, a simplified cylinder model which includes the indicated torque and the reciprocating inertia torque is adopted in this work [61, 112]. The indicated torque is caused by cylinder pressure and related to crankshaft angle, as described in equation

(4.17). The reciprocating inertia torque is used to express the inertial effect of piston which is related to engine speed and crankshaft angle, as shown in equation (4.18):

$$T_p = \frac{\pi D_p^2}{4} r_c p_g \sin(\zeta)(1 + \frac{r_c}{L_r}\cos(\zeta)) \tag{4.17}$$

$$T_i = m_r r_c^2 \omega_c^2 [\frac{r_c}{4L_r}\sin(\zeta) - \frac{1}{2}\sin(2\zeta) - \frac{3r_c}{4L_r}\sin(3\zeta) - \frac{r_c^2}{4L_r^2}\sin(4\zeta)] \tag{4.18}$$

Table 4.2. Parameters of PHHV powertrain multi body dynamic model.

Symbol	Parameter	Value	Symbol	Parameter	Value
		Inertia (kg·m^2)			
J_1	Engine accessory	0.0117	J_8	AMT output shaft	0.3792
J_2	Piston assembly 1	0.034	J_9	Driveshaft part 1	0.1167
J_3	Piston assembly 2	0.034	J_{10}	Driveshaft part 2	0.1367
J_4	Piston assembly 3	0.034	J_{11}	Main reducer	0.0527
J_5	Piston assembly 4	0.034	J_{12}	Differential to wheel	0.64
J_{6a}	Flywheel	0.615	J_{13}	Vehicle body	1349
J_{6b}	Engine clutch	0.03	J_{14a}	HPM	0.096
J_7	AMT input shaft	0.03567	J_{14b}	HPM clutch	0.03
		Stiffness (Nm/rad)			
K_1	Engine accessory shaft	165000	K_8	Driveshaft part 1	356000
K_2	Shaft between piston 1 and piston 2	1646400	K_9	Driveshaft part 2	356000
K_3	Shaft between piston 2 and piston 3	1646400	K_{10}	Main reducer	1163000
K_4	Shaft between piston 3 and piston 4	1646400	K_{11}	Differential shaft	1302400
K_5	Shaft between piston 4 and flywheel	1667000	K_{12}	Tyre	1332900
K_6	Engine clutch	19480	K_{13}	HPM clutch	1000
K_7	AMT output shaft	255700			
		Damping (Nm·s/rad)			
C_6	Engine clutch	10	C_{13}	HPM clutch	10
C_{12}	Tyre	460			

In the equations (4.17) and (4.18), T_p is engine piston torque, D_p is engine piston diameter, r_c is engine crank radius, p_g is cylinder pressure which is modelled as a lookup table as shown in Figure 4.2(a), L_r is connecting rod length, ζ is engine crankshaft angle, T_i is reciprocating inertia torque, m_r is engine piston reciprocating mass, ω_c is engine crankshaft speed.

Engine torque versus crankshaft angle is attained by combing all the four cylinders torque, as shown in Figure 4.2 (b).

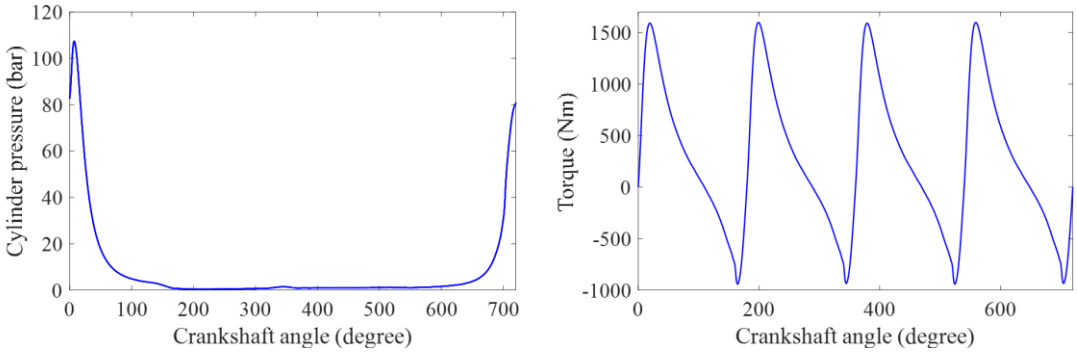

Figure 4.2. Engine characteristics, (a) Cylinder pressure, (b) Transient torque.

4.2.3 **HPM transient torque modelling**

HPM cylinders are divided by the valve plate as shown in Figure 4.3. When HPM rotates, cylinders connect with HPA and LPA alternately. In working process, the pressure in a single cylinder could be described by equation(4.19) [48].

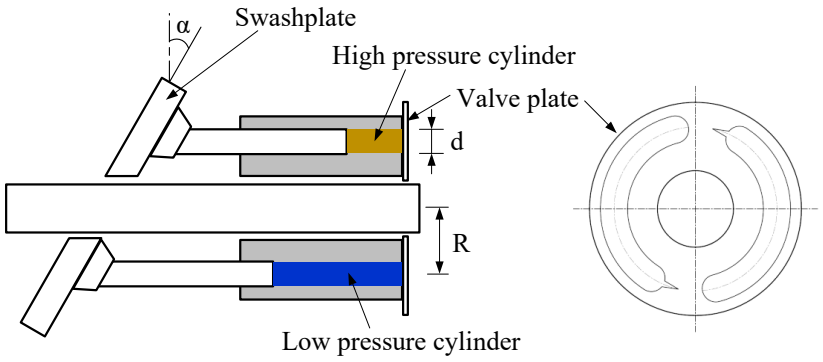

Figure 4.3. Schematic diagram of the HPM swashplate.

$$\frac{dp}{d\varphi_c} = -\frac{\beta_c\left(\frac{\pi d^2}{4}\omega_p R\tan\alpha\sin\varphi_c - Q - Q_l\right)}{\omega_p\left(V_{c0} - R\frac{\pi d^2}{4}(1-\cos\varphi_c)\tan\alpha\right)} \tag{4.19}$$

In the equation, p is oil pressure in cylinder, φ_c is cylinder angular displacement, β_c is cylinder oil bulk modulus, ω_p is cylinder rotational speed, Q is cylinder flowrate, Q_l is cylinder leakage which could be neglected in this research because its influence on pressure is very small [113]. V_{c0} is cylinder volume when swashplate angle is 0. Flowrate is described by equation (4.20):

$$Q = sign(p - p_d) C_d A_d \sqrt{\frac{2}{\rho}|p - p_d|} \tag{4.20}$$

where p_d is pressure of the cylinder connected circuit, C_d is cylinder discharge coefficient, A_d is cylinder discharge area. The cylinder discharge area change in one circle is shown in Figure 4.4(a). Normalized discharge area is the ratio of real time discharge area and the maximum discharge area.

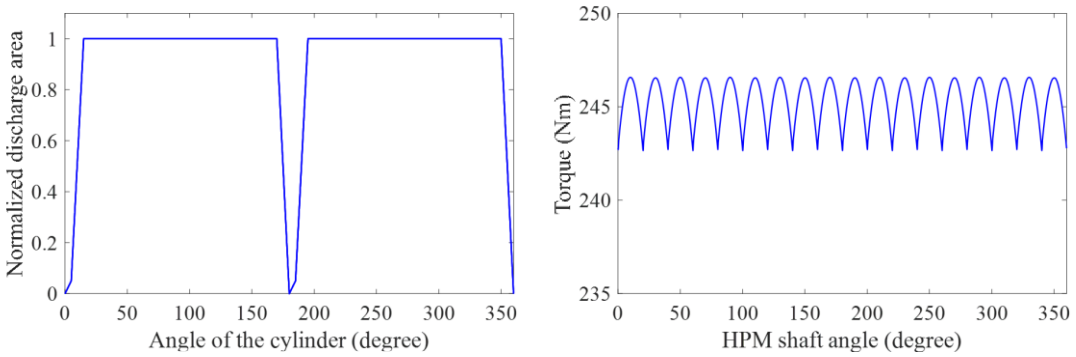

Figure 4.4. HPM characteristics, (a) Cylinder normalized discharge area, (b) transient torque.

The cylinder pressure generates torque on HPM shaft. The total HPM torque could be described by:

$$T_h = \sum_{i=1}^{z_c} \frac{\pi d^2}{4} p_i \tan\alpha R \sin\varphi_{ci} \tag{4.21}$$

HPM toque in one revolution is shown in Figure 4.4(b). It could be found that HPM torque fluctuation is much smaller than engine torque fluctuation.

Frequency analysis of engine torque and HPM torque is shown in Figure 4.5. Engine speed and HPM speed are both set to 900 rpm as examples. It is shown that the maximum engine torque excitation is 309% of its average torque while the maximum HPM torque excitation is only 0.64% of its average torque. This makes it possible to launch vehicle by HPM without causing large vibration at low vehicle speed.

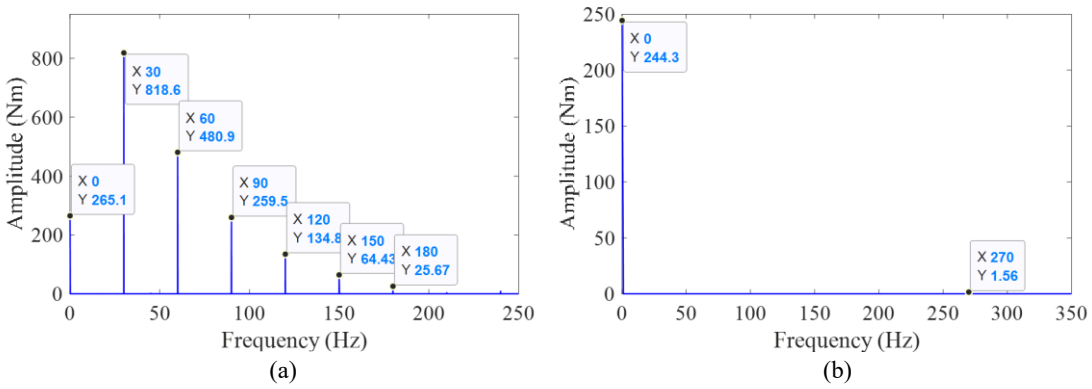

Figure 4.5. Frequency analysis, (a) Engine torque, (b) HPM torque.

4.3 **Vibration analysis and model reduction**

In hybrid driving mode, engine clutch and HPM clutch are all engaged. So engine clutch inertia and flywheel inertia are combined. HPM inertia and HPM clutch inertia are combined. The 16 degree of freedom model becomes a 14 degrees of freedom model, as shown in Figure 4.6.

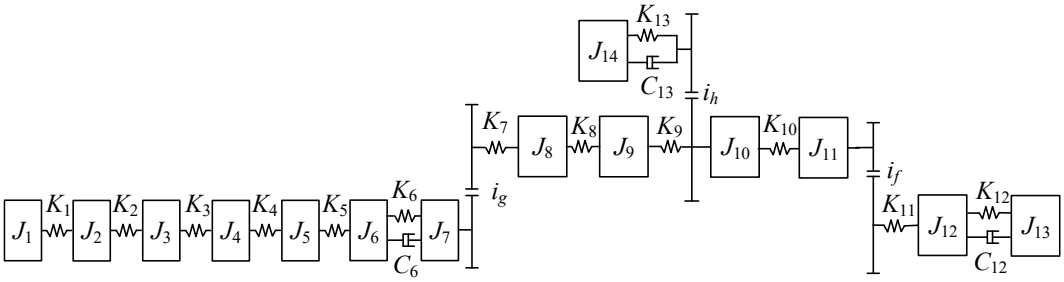

Figure 4.6. Multi body dynamic model of PHHV powertrain in hybrid driving mode.

In Figure 4.6, $J_6 = J_{6a} + J_{6b}$, $J_{14} = J_{14a} + J_{14b}$. The dynamic equations are deduced and described in matrix form in equation (4.22):

$$\mathbf{J}\ddot{\boldsymbol{\theta}} + \mathbf{C}\dot{\boldsymbol{\theta}} + \mathbf{K}\boldsymbol{\theta} = \mathbf{0} \tag{4.22}$$

where

$$\mathbf{J} = diag[J_1, J_2, J_3, ..., J_{12}, J_{13}, J_{14}] \tag{4.23}$$

$$\boldsymbol{\theta} = [\theta_1, \theta_2, \theta_3, ..., \theta_{12}, \theta_{13}, \theta_{14}]^T \tag{4.24}$$

$$\mathbf{C} = \begin{bmatrix}
0 & & & & & & & & & & & & & \\
& 0 & & & & & & & & & & & & \\
& & 0 & & & & & & & & & & & \\
& & & 0 & & & & & & & & & & \\
& & & & 0 & & & & & & & & & \\
& & & & & C_6 & -C_6 & & & & & & & \\
& & & & & -C_6 & C_6 & & & & & & & \\
& & & & & & & 0 & & & & & & \\
& & & & & & & & 0 & & & & & \\
& & & & & & & & & C_{13}i_h^{\,2} & & & & -C_{13}i_h \\
& & & & & & & & & & 0 & & & \\
& & & & & & & & & & & C_{12} & -C_{12} & \\
& & & & & & & & & & & -C_{12} & C_{12} & \\
& & & & & & & & & -C_{13}i_h & & & & C_{13}
\end{bmatrix} \tag{4.25}$$

$$\mathbf{K} = \begin{bmatrix}
K_1 & -K_1 & & & & & & & 0 & \\
-K_1 & K_1+K_2 & -K_2 & & & & & & 0 & \\
& -K_2 & K_2+K_3 & -K_3 & & & & & 0 & \\
& & -K_3 & K_3+K_4 & -K_4 & & & & 0 & \\
& & & -K_4 & K_4+K_5 & -K_5 & & & 0 & \\
& & & & -K_5 & K_5+K_6 & -K_6 & & & \\
& & & & & -K_6 & K_6+K_7/i_g^2 & \ldots\ldots & & \\
& & & & & & -K_7/i_g & & & \\
& & & & & & & & 0 & \\
& & & & & & & & 0 & \\
& & & & & & & & 0 & \\
& & & & & & & & 0 & \\
& & & & & & & & 0 & \\
& & & & & & & & 0 &
\end{bmatrix}$$

$$\begin{bmatrix}
0 & & & & & & & & \\
0 & & & & & & & & \\
0 & & & & & & & & \\
0 & & & & & & & & \\
0 & & & & & & & & \\
0 & & & & & & & & \\
-K_7/i_g & & & & & & & & \\
K_7+K_8 & -K_8 & & & & & & & \\
-K_8 & K_8+K_9 & -K_9 & & & & & & \\
0 & -K_9 & K_9+K_{10}+K_{13}i_h^2 & -K_{10} & & & & -K_{13}i_h & \\
0 & & -K_{10} & K_{10}+K_{11}/i_f^2 & -K_{11}/i_f & & & & \\
0 & & & -K_{11}/i_f & K_{11}+K_{12} & -K_{12} & & & \\
0 & & & & -K_{12} & K_{12} & & & \\
0 & & -K_{13}i_h & & & & & K_{13} &
\end{bmatrix} \tag{4.26}$$

By using the eigenvalue method, the natural frequencies and mode shapes of PHHV powertrain are attained. The natural frequencies are listed in Table 4.3 and the corresponding mode shapes are shown in Figure 4.7 to Figure 4.10. The 0 Hz frequency means a rigid body motion of PHHV powertrain.

Table 4.3. PHHV powertrain natural frequencies in hybrid driving mode.

Order	RBM	1st	2nd	3rd	4th	5th	6th
Frequency(Hz)	0	5	14.2	84.2	138.8	212	325.9
Order	7th	8th	9th	10th	11th	12th	13th
Frequency(Hz)	378.5	437.7	649.2	904.7	1145.3	1710.2	2084.7

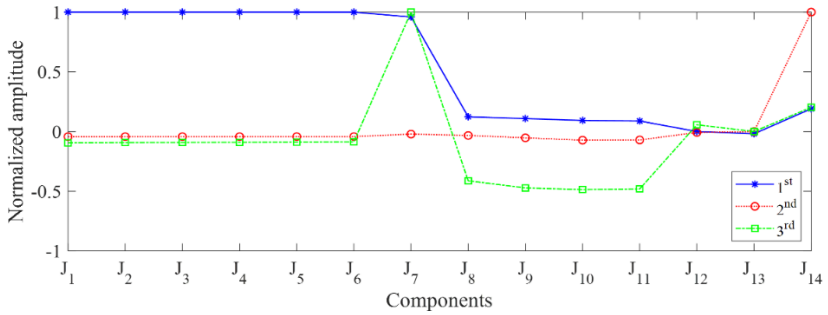

Figure 4.7. 1st to 3rd mode shapes of PHHV powertrain.

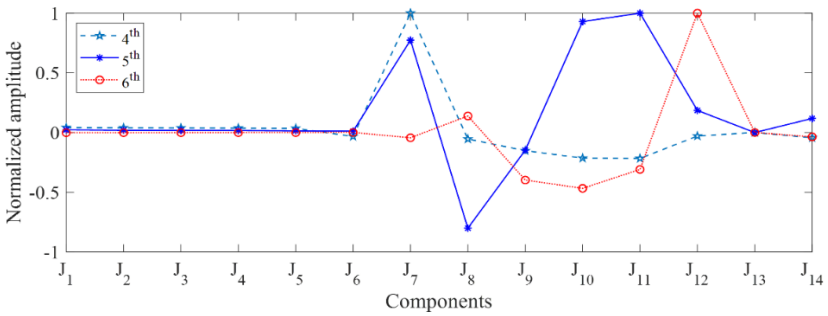

Figure 4.8. 4th to 6th mode shapes of PHHV powertrain.

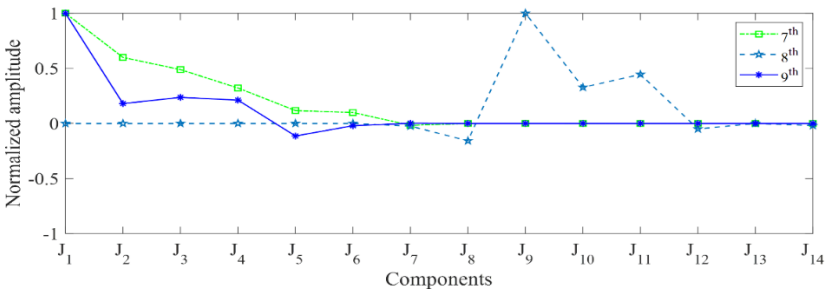

Figure 4.9. 7th to 9th mode shapes of PHHV powertrain.

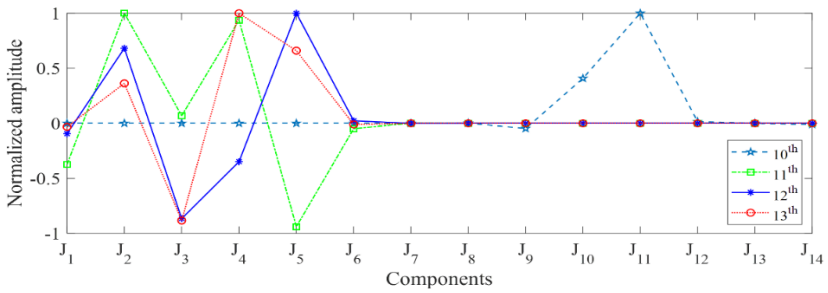

Figure 4.10. 10th to 13th mode shapes of PHHV powertrain.

From Table 4.3, some of the PHHV powertrain natural frequencies are quite high and unlikely to be excited considering the frequency range and amplitude of engine and HPM torque excitation. The mode shapes also illustrate that engine crankshaft and driveshaft are more sensitive to the high frequencies. To focus on the natural frequencies within interest and reduce model complexity [55], the PHHV powertrain 14 degrees of freedom dynamic model is simplified into a 6 degrees of freedom model as shown in Figure 4.11. In the simplified model, engine accessories, engine crankshaft and flywheel are combined. Driveshaft, main reducer and differential are combined. Descriptions and values of the parameters in simplified model are listed in Table 4.4.

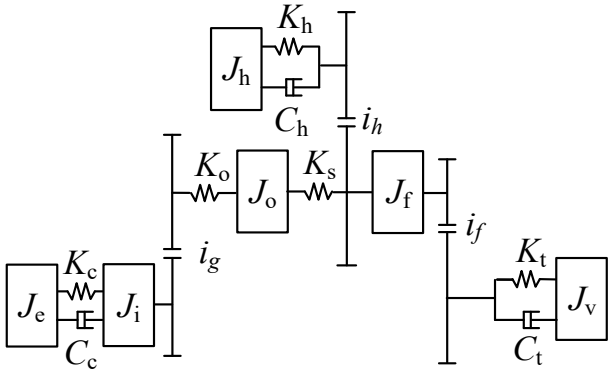

Figure 4.11. Simplified PHHV powertrain model.

4.3.1 **Vibration analysis in hybrid driving mode**

The natural frequencies of the simplified PHHV powertrain model in hybrid driving mode are shown in Table 4.5. Compared with the 14 degrees of freedom model in Figure 4.6, the first 5 natural frequencies are retained. The highest natural frequency of the simplified model is 193.6 Hz which is sufficient to research PHHV powertrain vibration under engine and HPM excitation. As a comparison, the original vehicle powertrain model which doesn't include hydraulic driving system is also built and its vibration

characteristics when engine clutch is engaged are also researched. Its natural frequencies are shown in Table 4.5 as well.

Table 4.4. Parameters of the simplified PHHV powertrain model.

Symbol	Parameter	Value	Symbol	Parameter	Value
		Inertia (kg·m^2)			
J_e	Engine	0.7927	J_f	Main reducer	0.2203
J_c	Engine clutch	0.03	J_v	Vehicle body	1349
J_i	AMT input shaft	0.03567	J_h	HPM	0.126
J_o	AMT output shaft and driveshaft	0.4959			
		Stiffness (Nm/rad)			
K_c	Engine clutch	19480	K_t	Tyre	641200
K_o	AMT output shaft	255700	K_h	HPM clutch	1000
K_s	Driveshaft	178000			
		Damping (Nm·s/rad)			
C_c	Engine clutch	10	C_t	Tyre	460
C_h	HPM clutch	10			

Compared with original vehicle powertrain, there is a new natural frequency in PHHV powertrain which is the 2nd natural frequency of 14.2 Hz. Other PHHV powertrain natural frequencies are close to original vehicle powertrain. The 2nd, 3rd and 4th natural frequencies of original vehicle powertrain become the 3rd, 4th and 5th natural frequencies of PHHV powertrain.

Table 4.5. Natural frequencies of PHHV powertrain (in hybrid driving mode) and Original vehicle powertrain (engine clutch engaged).

PHHV	Order	RBM	1st	2nd	3rd	4th	5th
	Frequency (Hz)	0	5	14.2	84.2	140.5	193.6
Original vehicle	Order	RBM	1st	2nd	3rd	4th	
	Frequency (Hz)	0	5	84	139.6	194.7	

Mode shapes of PHHV powertrain and original vehicle powertrain are shown in Figure 4.12. Mode shapes are normalized and drawn according to the corresponding natural frequencies. The 2nd, 3rd and 4th mode shapes of original vehicle powertrain become the

3rd, 4th and 5th mode shapes of PHHV powertrain. There is one more degree of freedom in PHHV mode shapes caused by HPM.

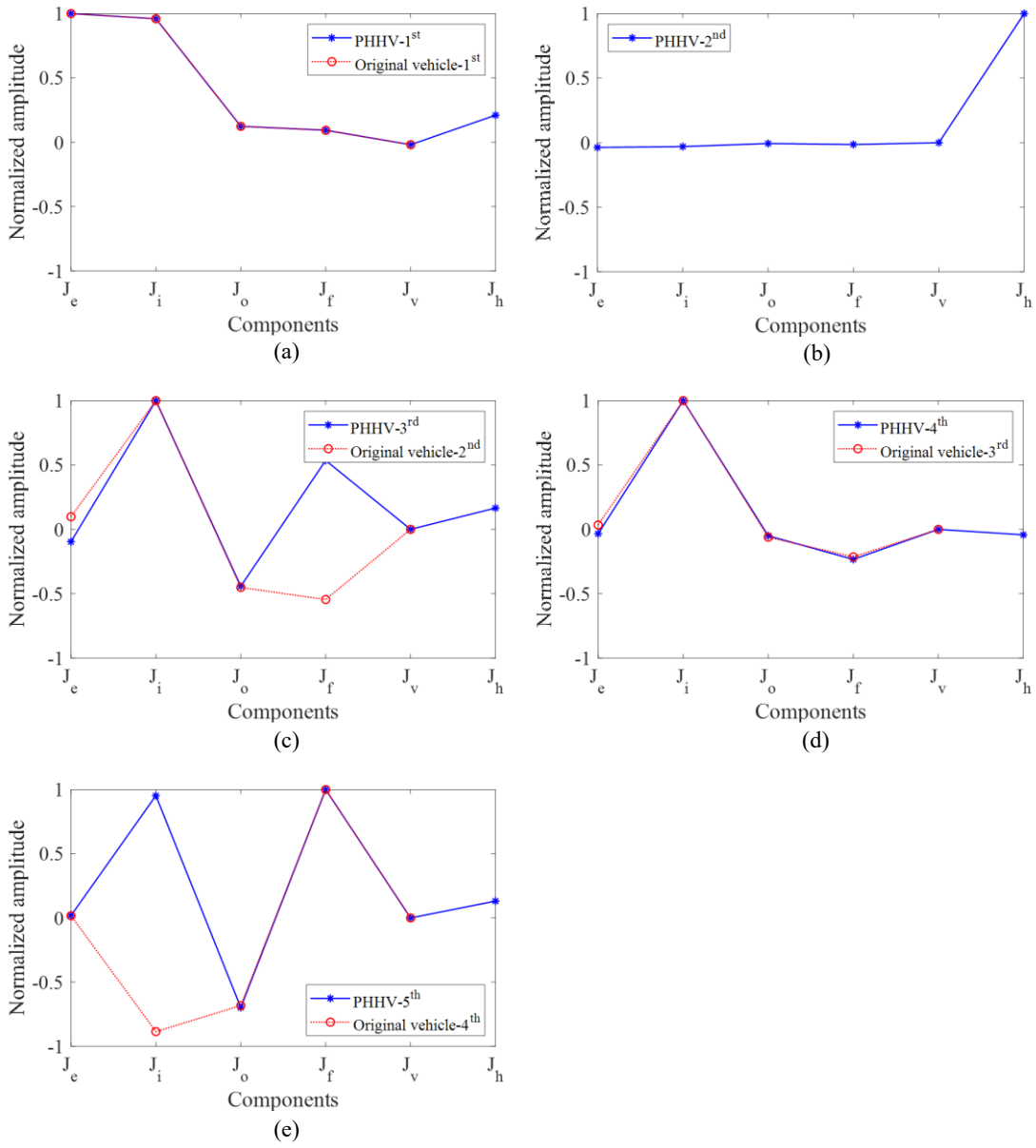

Figure 4.12. Mode shapes of PHHV powertrain (in hybrid driving mode) and original vehicle powertrain (engine clutch engaged).

Figure 4.12(a) and Figure 4.12(d) demonstrates that the 1st and 3rd mode shapes of original vehicle powertrain are almost unchanged. Figure 4.12(b) shows the 2nd mode shape of PHHV powertrain. In this mode shape, HPM has the biggest vibration and other components do not vibrate a lot. This means HPM is much more sensitive to the 2nd natural frequency than other components. The 2nd and 4th mode shapes of original vehicle powertrain are changed by HPM inertia. As shown in Figure 4.12(c), amplitude of the final reducer vibration is not changed but the direction is changed to the opposite

direction. In Figure 4.12(e), amplitude of the AMT input shaft vibration is not changed but the direction is changed to the opposite direction.

4.3.2 **Vibration analysis in HPM driving mode**

In HPM driving mode, engine clutch is disengaged so engine crankshaft inertia and flywheel inertia are not included in PHHV powertrain. PHHV powertrain natural frequencies in this driving mode are shown in Table 4.6 and mode shapes are shown in Figure 4.13. Natural frequencies and mode shapes of original vehicle powertrain with engine clutch disengaged are also shown in Table 4.6 and Figure 4.13 as comparison. Compared with the natural frequencies when engine clutch is engaged, the 1st, 2nd and 3rd natural frequencies of original vehicle powertrain are increased obviously. It could be explained that when engine clutch is disengaged, engine and flywheel inertia are excluded and only clutch inertia remains. This inertia is more sensitive to the 1st, 2nd and 3rd natural frequencies. When inertia reduces, the relative natural frequencies increase.

Table 4.6. Natural frequencies of PHHV powertrain (in HPM driving mode) and Original vehicle powertrain (engine clutch disengaged).

PHHV	Order	RBM	1st	2nd	3rd	4th	5th
	Frequency (Hz)	0	12.9	15	103	178.4	192.8
Original vehicle	Order	RBM	1st	2nd	3rd	4th	
	Frequency (Hz)	0	13.6	102.4	178.8	193.4	

Natural frequencies of PHHV powertrain remain close to original vehicle powertrain in this driving mode. The additional natural frequency caused by HPM is 15 Hz. Figure 4.13 shows that mode shapes of PHHV powertrain and original vehicle powertrain are very similar, which demonstrates that adding a hydraulic driving system doesn't remarkably change original vehicle powertrain mode shapes. In the additional mode shape brought by HPM as shown in Figure 4.13(b), HPM has the largest vibration, which means HPM is very sensitive to the 2nd natural frequency. It should be noticed that engine clutch and AMT input shaft also have considerable vibration in this mode shape, indicating engine clutch and AMT input shaft are sensitive to the 2nd natural frequency. So the frequency response of these two components to HPM excitation with the 2nd natural frequency should be investigated to avoid engine clutch and AMT input shaft failure in HPM driving mode.

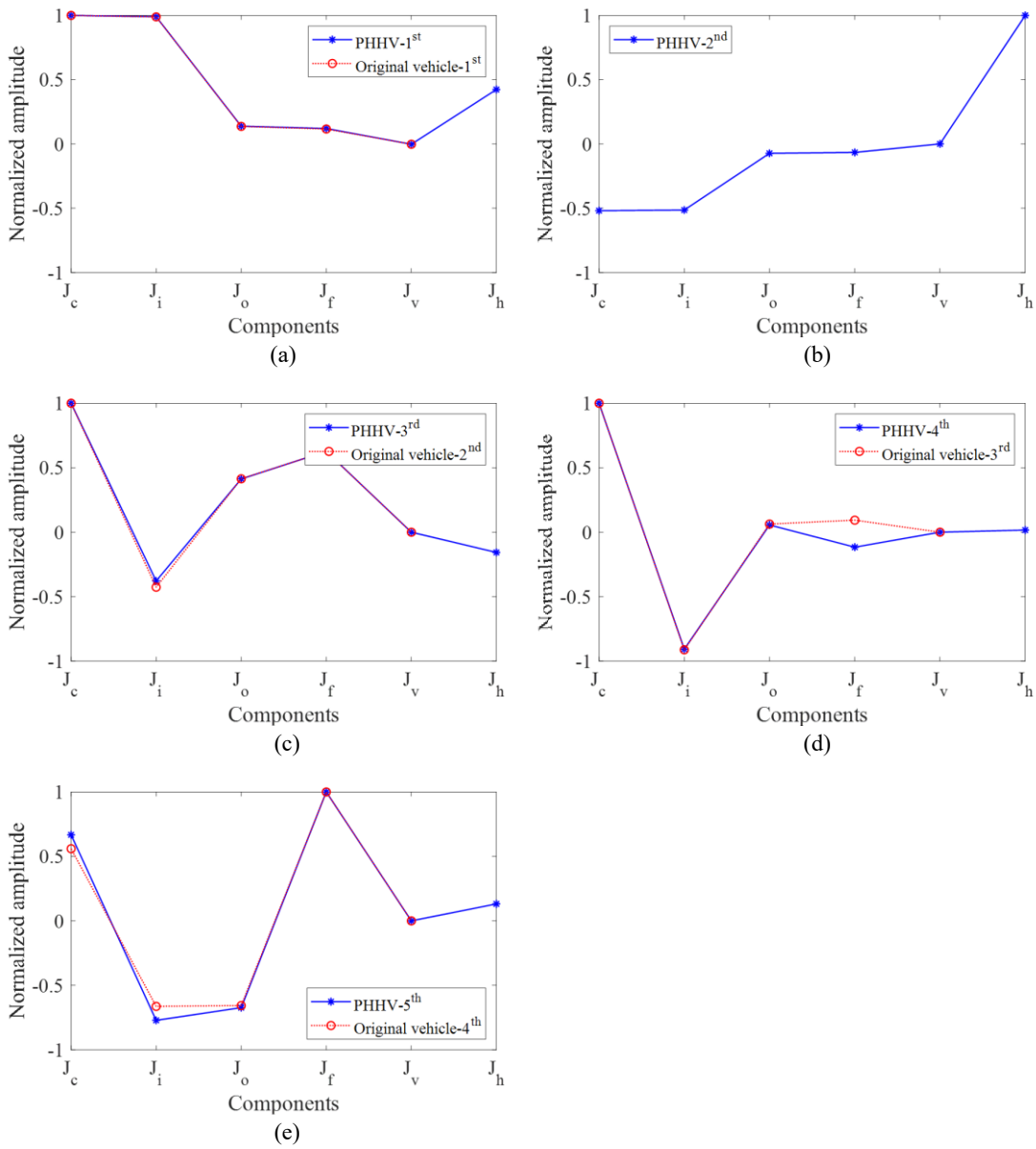

Figure 4.13. Mode shapes of PHHV powertrain (in HPM driving mode) and original vehicle powertrain (engine clutch disengaged).

4.4 **Frequency response analysis**

Various excitations could stimulate PHHV powertrain vibration. But engine torque fluctuation and HPM torque fluctuation are the dominant factors [114, 115]. So the frequency response of PHHV powertrain and original vehicle powertrain under engine torque and HPM torque excitation are investigated in this section.

4.4.1 **Frequency response analysis in hybrid driving mode**

In hybrid mode, engine and HPM are both included in PHHV powertrain, so excitation could come from either of them. Frequency response of PHHV powertrain under engine and HPM excitation is shown in Figure 4.14. As a comparison, frequency response of original vehicle powertrain under engine excitation is also shown in Figure 4.14. In the figure legends, J indicates powertrain components, T_e is engine excitation and T_h is HPM excitation.

In PHHV powertrain, at the 1st natural frequency, frequency response to engine excitation is increased by around 40% compared with original vehicle powertrain. However, considering that in this mode, engine clutch is engaged so engine speed should be higher than its idle speed which is normally higher than 800 rpm. The consequent minimum engine excitation frequency is 26.7 Hz according to engine torque frequency analysis. This frequency is higher than the first natural frequency so the first mode response will never be excited by engine.

The 2nd natural frequency is introduced by HPM inertia. At this frequency, frequency response of PHHV powertrain to engine excitation does not show obvious difference to original vehicle powertrain. At higher natural frequencies, frequency response of PHHV powertrain to engine excitation is reduced to lower than original vehicle powertrain.

HPM torque also introduces excitation to PHHV powertrain. At the 1st natural frequency, PHHV powertrain has a larger response to HPM excitation. But this dangerous scenario is also avoided because in this mode, engine clutch is engaged, so vehicle should have a minimum speed determined by the minimum engine speed and AMT gear ratios. HPM also has a minimum speed according to vehicle speed in this mode. HPM excitation frequency is higher than the 1st natural frequency even with the minimum working speed. For the 2nd natural frequency, frequency response of engine, AMT input shaft and AMT output shaft to HPM excitation are smaller than their response to engine excitation. However, frequency response of final reducer and vehicle body to HPM excitation are higher than their response to engine excitation. It is demonstrated in Figure 4.5 that HPM has much smaller torque fluctuation than engine, so it will not generate significant vibrations to PHHV powertrain.

HPM also vibrates under engine and its own excitation as shown in Figure 4.14(f). At the 1st natural frequency, frequency response of HPM to engine excitation is smaller than

frequency response of engine and AMT input shaft but higher than other components.

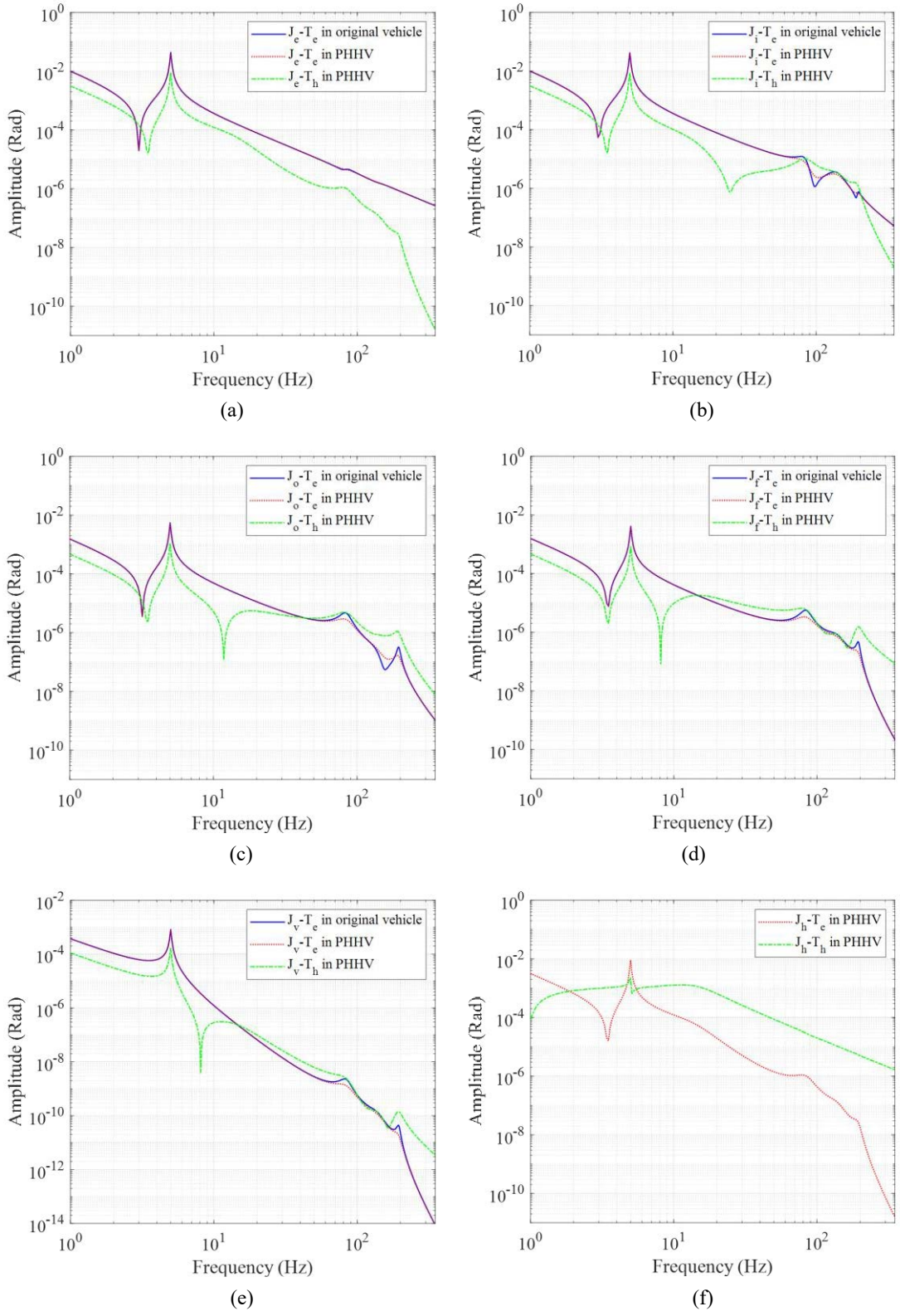

Figure 4.14. Amplitude of frequency response function of PHHV powertrain (in hybrid driving mode) and original vehicle powertrain (engine clutch engaged).

Frequency response of HPM to its own excitation is much smaller than its response to engine excitation. HPM shows significant frequency response to its own excitation at the 2nd natural frequency. However large vibration is also avoided due to the small torque fluctuation of HPM. For higher natural frequencies, HPM does not show significant frequency response to engine excitation or its own excitation.

4.4.2 **Frequency response analysis in HPM driving mode**

In HPM driving mode, there is only HPM excitation to PHHV powertrain. HPM excitation frequency could start from 0 Hz when launching vehicle. Frequency response of PHHV powertrain to HPM excitation is shown in Figure 4.15. Each component has a big response to HPM excitation at the 1st natural frequency. HPM has considerable frequency response at the 2nd natural frequency while other components do not show significant frequency response at this frequency. For higher natural frequencies, all components have small responses.

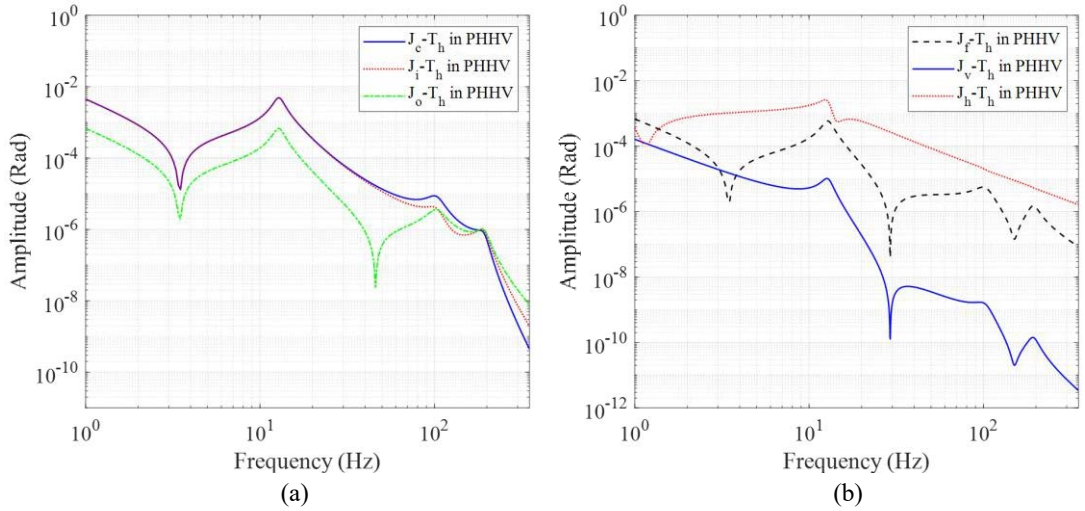

Figure 4.15. Amplitude of frequency response function of PHHV powertrain (in HPM driving mode).

4.4.3 **PHHV powertrain response under normalized engine and HPM excitation**

From above analysis, in PHHV powertrain, frequency response to engine excitation is not changed very much compared with original vehicle, but response to HPM excitation in HPM driving mode is remarkable, especially at the 1st natural frequency. It is necessary to investigate if the original powertrain strength is still qualified after hydraulic driving system is added.

The relationship of HPM speed and engine speed could be described by:

$$n_h = n_e \frac{i_h}{i_g} \tag{4.27}$$

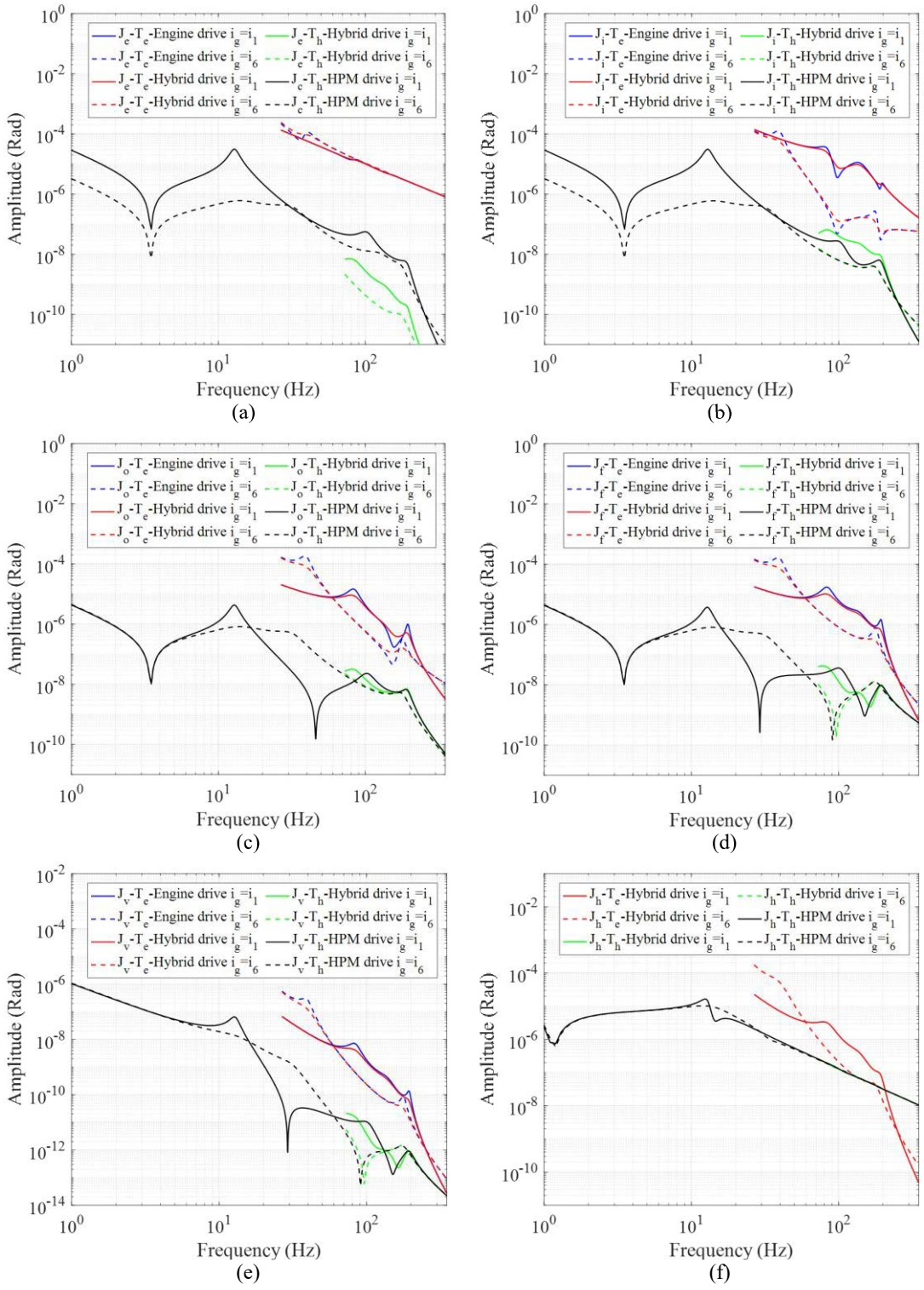

Figure 4.16. PHHV powertrain response under normalized engine excitation and HPM excitation.

In hybrid driving mode, engine clutch is engaged. The minimum engine speed is its idle speed. In this research, the engine idle speed is 800 rpm. So the minimum HPM speed is 241.7 rpm by equation (4.27). The corresponding lowest frequencies of engine excitation and HPM excitation are 26.7 Hz and 72.5 Hz respectively. To attain the angular response of each component in PHHV powertrain and original powertrain, normalized excitations are adopted, which means the average engine torque and HPM torque are considered to be 1 Nm. Results are shown in Figure 4.16. AMT has six gear ratios. The 1st and the 6th gear ratio are shown as representatives. Response with other gear ratios should be between these two gear ratios.

As shown in Figure 4.16, the engine caused vibration in hybrid driving mode doesn't exceed the vibration in engine driving mode, so the original powertrain is still qualified for engine excitation. Due to small HPM torque fluctuation, vibration caused by HPM is very small. This means PHHV powertrain is safe in hybrid driving mode.

In HPM driving mode, the first natural frequency 12.8 Hz could be excited by HPM. From Figure 4.16, PHHV powertrain response to HPM excitation is smaller than the response to engine excitation in original vehicle powertrain. So the original powertrain is still qualified for HPM driving after the modification. At the 2nd natural frequency of 15 Hz which is brought by HPM, only HPM shows obvious resonance but the amplitude is much smaller than the 1st natural frequency. Other components don't show obvious resonance at this natural frequency, which means powertrain vibration is not remarkable in the additional mode shape.

4.5 **Parameter sensitivity analysis of powertrain frequency response**

In PHHV, HPM clutch could be designed with different stiffness. PHHV could also work with different load conditions so have different vehicle mass.

4.5.1 **HPM clutch stiffness sensitivity analysis**

The effect of different HPM clutch stiffness on PHHV powertrain vibration characteristics are analysed in this section. Results are shown in Figure 4.17. With higher HPM clutch stiffness, The PHHV powertrain natural frequency brought by HPM is increased. Figure 4.17(f) shows that if HPM clutch stiffness is reduced, HPM response to its own excitation is increased at frequency lower than the 1st natural frequency. So smaller HPM clutch stiffness brings increased HPM vibration under low frequency HPM

excitation. This indicates a conflict between HPM vibration and other components vibration. In engineering design, a balanced HPM clutch stiffness should be selected. In this research, HPM clutch stiffness is designed as 1000 Nm/rad with a compromise considering HPM vibration and other components vibration.

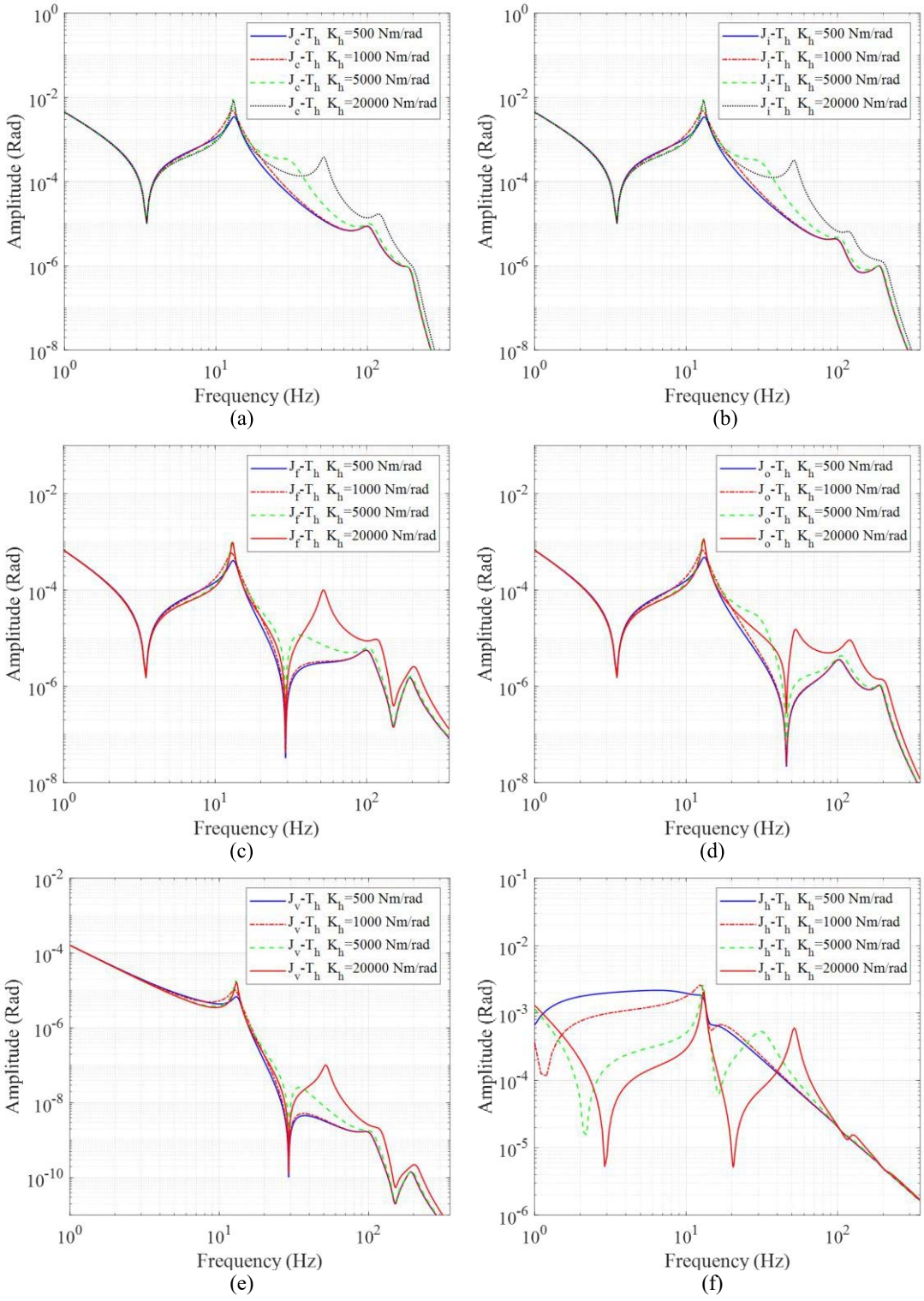

Figure 4.17. Sensitivity analysis with different HPM clutch stiffness.

4.5.2 **Vehicle mass sensitivity analysis**

In this section, PHHV powertrain vibration characteristics are researched with no load, half load and full load respectively. Results are shown in Figure 4.18.

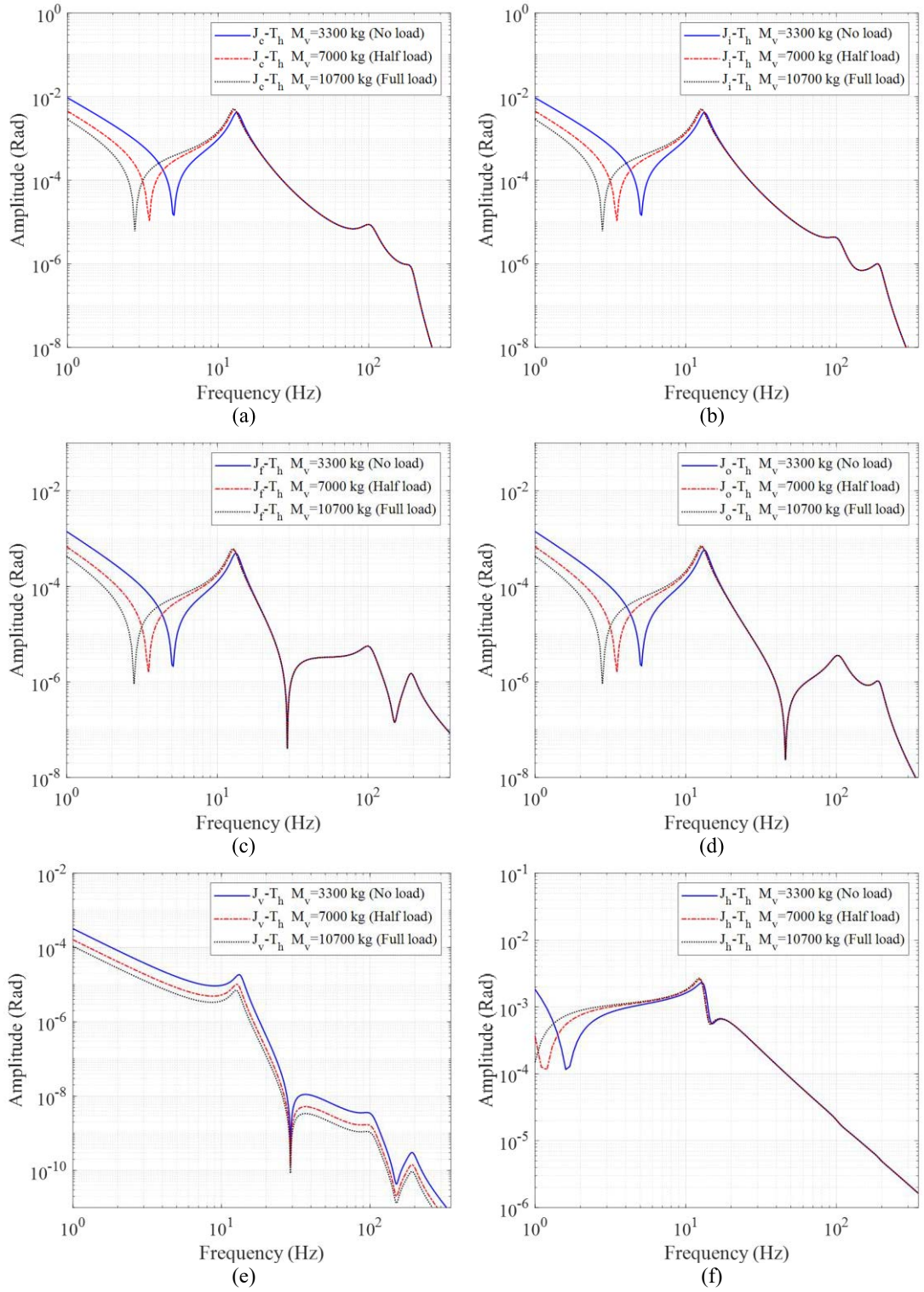

Figure 4.18. Sensitivity analysis with different load conditions.

When vehicle mass is increased, the 1st natural frequency is decreased while other natural frequencies are kept unchanged. The vehicle body response to HPM excitation decreases with bigger vehicle mass. However, for other PHHV powertrain components, their response to HPM excitation increases with vehicle mass.

4.6 **Summary**

In this chapter, a 14 degrees of freedom PHHV powertrain model is built and its natural frequencies and mode shapes are researched. This model is then simplified into a 6 degrees of freedom model to reduce model complexity considering engine and HPM excitation characteristics. Natural frequencies and mode shapes of PHHV powertrain and original vehicle powertrain are compared. It is demonstrated that the additional HPM inertia brings a new natural frequency and a new mode shape to vehicle powertrain. The original vehicle powertrain natural frequencies are not changed too much by HPM. In hybrid driving mode, powertrain response to engine excitation is increased 40% at the 1st natural frequency. But because the minimum engine excitation frequency and HPM excitation frequency are higher than the 1st natural frequency, the first mode shape is never excited. In HPM driving mode, the powertrain frequency response to HPM excitation is quite big at the 1st frequency. However, HPM excitation amplitude is small, so it does not introduce too much vibration to powertrain. Parameter analysis indicates that HPM clutch stiffness has a great influence on PHHV powertrain natural frequencies. It should be designed by compromising HPM vibration and other powertrain components vibration. Different load conditions are considered to investigate the effect of vehicle mass. Simulation results reveal that larger vehicle mass slightly decreases the 1st natural frequency. Vehicle body response to HPM excitation decreases with increasing vehicle mass while other powertrain components response to HPM excitation increases with increasing vehicle mass. From above analysis, original vehicle powertrain strength is still qualified after it is modified into PHHV.

Chapter 5 Mode switching control

5.1 Introduction

To avoid engine working at low efficiency and poor emission regions, HPM is used to launch vehicle. When the hydraulic energy stored in HPA is used up, mode switching is conducted to transfer PHHV from HPM driving mode to engine driving mode. During mode switching, engine is ignited and driving torque is transferred from HPM to engine. After mode switching, vehicle is driven by engine and HPM stops driving vehicle.

5.2 Powertrain modelling for mode switching control

Vehicle is driven by HPM before mode switching. In this scenario, HPM clutch is engaged and engine clutch is disengaged. From vibration analysis in Chapter 4 high order powertrain mode shapes are hard to be excited. So to reduce model complexity, the simplified model is adopted to research the vibration during mode switching, as shown in Figure 5.1. Dynamic equations are developed as shown in (5.1) to (5.7).

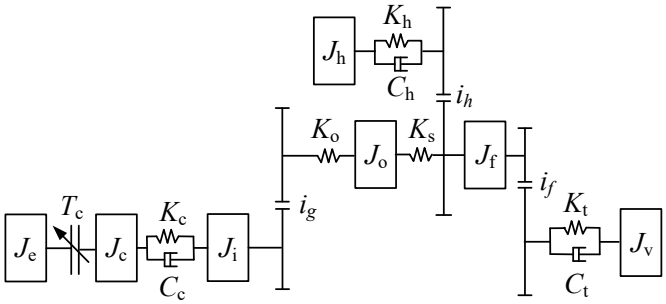

Figure 5.1. PHHV Powertrain dynamic model for mode switching control.

$$J_e\ddot{\theta}_e = T_e - T_c \tag{5.1}$$

$$J_c\ddot{\theta}_c = K_c(\theta_i - \theta_c) + C_c(\dot{\theta}_i - \dot{\theta}_c) + T_c \tag{5.2}$$

$$J_i\ddot{\theta}_i = K_o(\theta_o - \theta_i / i_g)/i_g - K_c(\theta_i - \theta_c) - C_c(\dot{\theta}_i - \dot{\theta}_c) \tag{5.3}$$

$$J_o\ddot{\theta}_o = K_s(\theta_f - \theta_o) - K_o(\theta_o - \theta_i / i_g) \tag{5.4}$$

$$\begin{aligned} J_f\ddot{\theta}_f = {} & K_t(\theta_w - \theta_f / i_f)/i_f + C_t(\dot{\theta}_w - \dot{\theta}_f / i_f)/i_f - K_s(\theta_f - \theta_o) \\ & -K_h(\theta_f i_h - \theta_h)i_h - C_h(\dot{\theta}_f i_h - \dot{\theta}_h)i_h \end{aligned} \tag{5.5}$$

$$J_h\ddot{\theta}_h = T_h + K_h(\theta_f i_h - \theta_h) + C_h(\dot{\theta}_f i_h - \dot{\theta}_h) \tag{5.6}$$

$$J_v\ddot{\theta}_w = -K_t(\theta_w - \theta_f / i_f) - C_t(\dot{\theta}_w - \dot{\theta}_f / i_f) - T_L \tag{5.7}$$

In the equations, J_c is engine clutch inertia, θ_c is engine clutch angular displacement.

5.3 **Mode switching process analysis and control strategy design**

Mode switching is divided into 5 phases as shown in Figure 5.2.

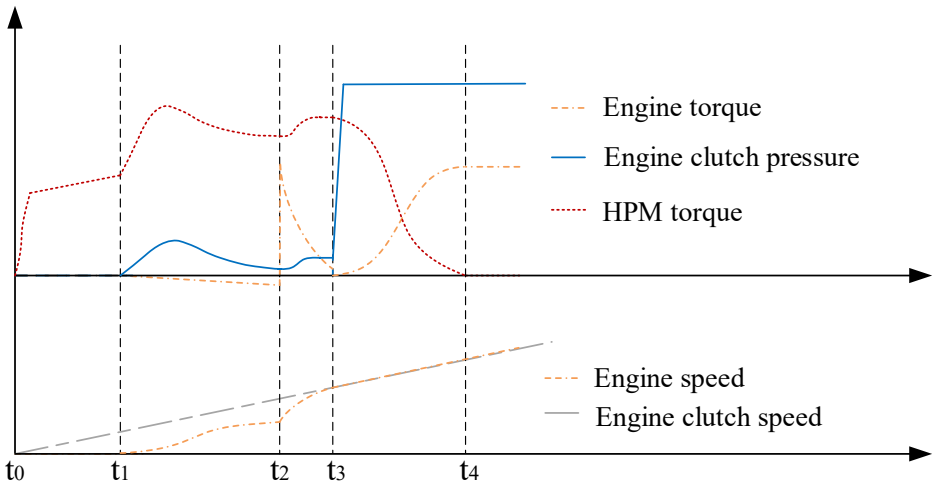

Figure 5.2. Mode switching process.

(1) Phase 1: HPM driving

Phase 1 starts from t_0 and ends at t_1. In this phase, HPM launches vehicle from standstill and drives vehicle. Engine clutch is disengaged and engine doesn't work.

(2) Phase 2: Engine cranking

This phase is from t_1 to t_2. When mode switching condition is satisfied, engine clutch pressure is increased. Engine clutch torque speeds up engine crankshaft. In this phase engine speed is lower than engine clutch speed, so engine clutch torque direction on driveshaft is opposite to clutch rotational direction. Vehicle acceleration tends to be decreased by engine clutch torque. To maintain vehicle dynamic performance, HPM torque is adjusted to compensate for engine clutch torque.

(3) Phase 3: Engine speed regulation

This phase is between t_2 and t_3. When engine speed reaches its ignition speed, engine is ignited then begins speed regulation. After ignition, engine begins to output torque. Engine speed is regulated by both engine torque and engine clutch torque. Engine speed target is the engine clutch speed. During engine speed regulation, engine clutch torque is also adjusted. Before engagement, engine clutch torque is proportional to its pressure. However, after engagement, engine clutch torque is determined by engine torque and

engine crank acceleration. Efforts should be made to achieve consistent engine clutch torque before and after engagement [78]. In this control strategy, engine torque is set to be 0 at the moment when engine clutch is engaged. So after engagement, engine clutch torque is the torque needed for engine crank acceleration. This torque is set as the target engine clutch torque in phase 3.

(4) Phase 4: Engine clutch engagement and torque transfer

Phase 4 starts from t_3 and ends at t_4. When the speed difference between engine and engine clutch is reduced to a target value by engine speed regulation and engine clutch reaches its target torque, start engaging engine clutch. Due to engine speed control accuracy, the speed difference is still too big to engage engine clutch rapidly. Therefore, clutch pressure is increased slowly at the beginning of this phase. When the speed difference reaches a small value, clutch pressure is increased rapidly and engine clutch is fully engaged. Driving torque is transferred from HPM to engine in this phase. Engine torque increases and HPM torque decreases at the same time. Vehicle is driven by engine and HPM simultaneously in this phase.

(5) Phase 5: Engine driving

At t_4, HPM torque reaches 0 and phase 5 starts. In phase 5, HPM doesn't drive vehicle. Vehicle is only driven by engine. Engine torque is determined by driver torque demand.

A flowchart is used to describe the mode switching control strategy, as shown in Figure 5.3.

5.4 **Control strategy design for each phase**

(1) Phase 1 control strategy

In phase 1, HPM launches and drives vehicle independently. Engine torque is 0 and engine clutch pressure is 0. To satisfy driver torque demand, HPM driving mode should have the same vehicle driving torque as engine driving mode. HPM torque and engine torque are:

$$\begin{cases} T_h = \dfrac{T_{dri}}{i_h i_f} \\ T_e = 0 \end{cases} \tag{5.8}$$

In vehicle launching, if the target driver demand torque is applied on vehicle rapidly, powertrain could vibrate heavily under the impulse torque input [116]. To reduce

powertrain vibration, vehicle driving torque changing rate is controlled [117]. In this phase, vehicle is launched by HPM. Throttle changing rate is designed for different launching intentions.

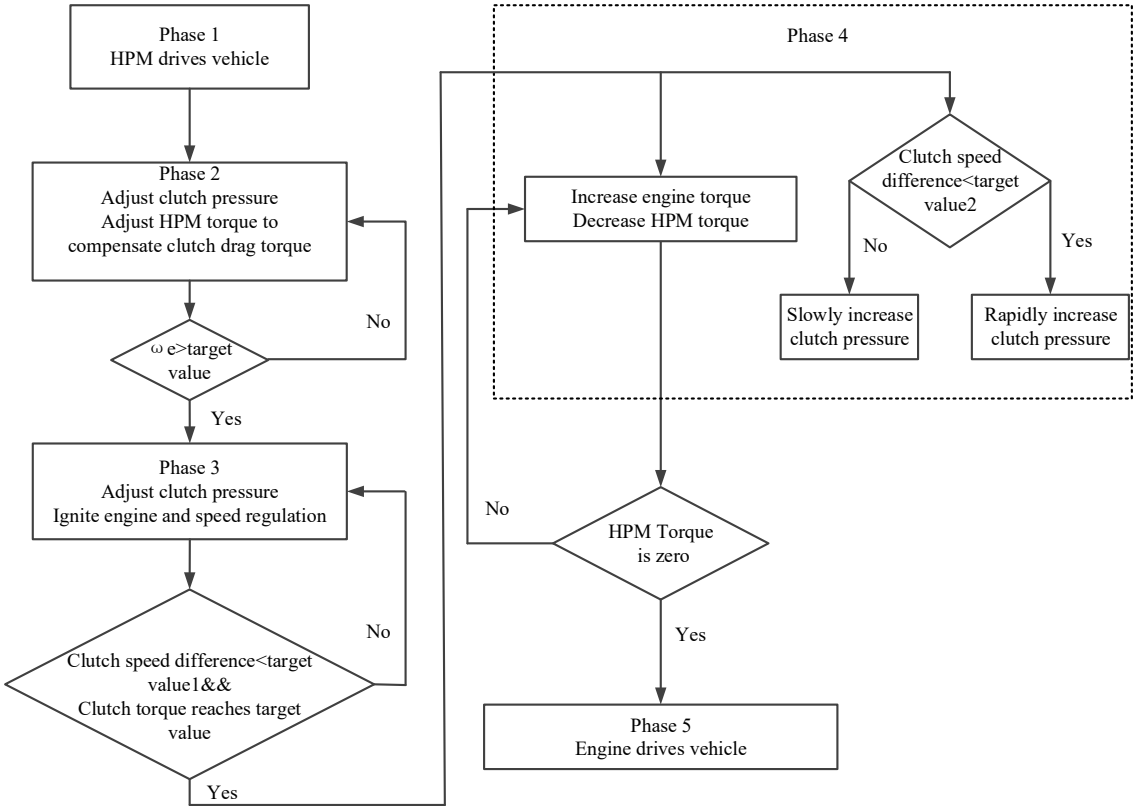

Figure 5.3. Mode switching control strategy.

(2) Phase 2 control strategy

The target of this phase is to start engine with engine clutch torque. In this phase, engine is started by engine clutch and the clutch torque on powertrain is compensated by HPM. Vehicle acceleration is controlled to be constant, as a representative of stable vehicle dynamic performance.

During engine start process, clutch slipping introduces vehicle jerk and clutch frictional work [118]. Vehicle jerk is the derivative of vehicle acceleration. For the convenience of control strategy design, driveshaft is treated as a rigid body [67, 119]. So vehicle jerk is further determined by engine clutch torque and HPM torque changing rate. Vehicle jerk and clutch frictional work are indicated as equation (5.9) and equation (5.10).

$$j_v = \frac{da}{dt} = \frac{\left(\dot{T}_c i_g \eta_e + \dot{T}_h i_h \eta_h\right) i_f}{\delta M R_w} \tag{5.9}$$

$$W_c = \int_{t_{s1}}^{t_{s2}} \left| T_c(\dot{\theta}_c - \dot{\theta}_e) \right| \mathrm{d}t \tag{5.10}$$

where j_v is vehicle jerk, W_c is clutch frictional work. t_{s1} and t_{s2} are the start time and end time of engine clutch slipping process.

Vehicle jerk and clutch frictional work are contradictory targets. Generally, faster clutch engagement process causes higher vehicle jerk but less clutch frictional work, while slower clutch engagement brings lower vehicle jerk and more clutch frictional work. To analyse the conflict between vehicle jerk and clutch frictional work, LQR controller is used in this phase. LQR controller makes compromise among different targets [120-122]. In this section, LQR weighting matrices are selected to reflect different driver intentions on vehicle driving comfort and dynamic performance. According to the equations of vehicle powertrain model, the state variables are selected as equation (5.11):

$$\begin{aligned} x_1 &= \dot{\theta}_e, \\ x_2 &= \dot{\theta}_{er} - \dot{\theta}_e, \\ x_3 &= \dot{\theta}_c - \dot{\theta}_e, \\ x_4 &= T_c \end{aligned} \tag{5.11}$$

where $\dot{\theta}_{er}$ is engine speed target which is set as engine ignition speed in this phase. Vehicle dynamic performance is guaranteed by keeping a constant vehicle acceleration during mode switching. Powertrain is treated as a rigid body for mode switching control strategy design, so engine clutch acceleration is:

$$\ddot{\theta}_c = \frac{a i_f i_g}{R_w} \tag{5.12}$$

Engine clutch torque changing rate is set as the control variable:

$$u = \dot{T}_c \tag{5.13}$$

So, the system state space function is:

$$\dot{\mathbf{X}} = \mathbf{A}\mathbf{X} + \mathbf{B}\mathbf{U} + \mathbf{E} \tag{5.14}$$

in which **X, U, E** are:

$$\mathbf{X} = \left[x_1, x_2, x_3, x_4\right]^T,\ \mathbf{U} = u,\ \mathbf{E} = [0, 0, \ddot{\theta}_c, 0]^T \tag{5.15}$$

The system parameter matrices are shown as following:

$$\mathbf{A}=\begin{bmatrix} 0 & 0 & 0 & \frac{1}{J_e} \\ 0 & 0 & 0 & -\frac{1}{J_e} \\ 0 & 0 & 0 & -\frac{1}{J_e} \\ 0 & 0 & 0 & 0 \end{bmatrix},\ \mathbf{B}=\begin{bmatrix} 0 \\ 0 \\ 0 \\ 1 \end{bmatrix} \tag{5.16}$$

The boundary condition is set as:

$$0 \le T_h \le T_{h\_\max} \tag{5.17}$$

The cost function is shown in equation (5.18). In the cost function, **Q** and **R** are weighting matrices which reflect driver intentions. In this research, vehicle jerk and clutch frictional work are investigated so weighting matrices elements are selected as equation (5.19). In matrix **Q**, $q_{34}=q_{43}$.

$$j=\frac{1}{2}\int_{t_{i2}}^{t_{f2}}\left[\mathbf{X}^T\mathbf{Q}\mathbf{X}+\mathbf{U}^T\mathbf{R}\mathbf{U}\right]dt \tag{5.18}$$

$$\mathbf{Q}=\begin{bmatrix} 0 & 0 & 0 & 0 \\ 0 & q_{22} & 0 & 0 \\ 0 & 0 & 0 & q_{34} \\ 0 & 0 & q_{43} & 0 \end{bmatrix},\ \mathbf{R}=r \tag{5.19}$$

With the selected **Q** and **R**, the cost function is:

$$j=\frac{1}{2}\int_{t_{i2}}^{t_{f2}}\left[q_{22}(\dot{\theta}_{er}-\dot{\theta}_e)^2+2q_{34}(\dot{\theta}_c-\dot{\theta}_e)T_c+r\dot{T}_c^2\right]dt \tag{5.20}$$

In equation (5.20), j is cost function. t_{i2} and t_{f2} are the start time and end time of LQR control process, $q_{22}(\dot{\theta}_{er}-\dot{\theta}_e)^2$ represents the requirement of adjusting engine speed to its target speed. If q_{22} is larger, engine speed should be adjusted to its target value faster. $q_{34}(\dot{\theta}_c-\dot{\theta}_e)T_c$ represents the requirement of clutch frictional work. Larger q_{34} requires lower clutch frictional work. $r\dot{T}_c^2$ represents the requirement of restricting engine clutch torque changing rate which affects vehicle jerk. Larger r requires engine clutch torque to change slower, which helps to decrease vehicle jerk. The values of weighting matrices elements determine the requirements on different targets.

In LQR control, the control variable **U** is attained by state feedback, as shown in equation (5.21):

$$\mathbf{U}=\text{-}\mathbf{R}^{-1}\mathbf{B}^T\mathbf{G}\mathbf{X} \tag{5.21}$$

$\mathbf{G}$ is attained through solving the following Riccati equation [123]:

$$\mathbf{0} = -\mathbf{GA} - \mathbf{A}^T\mathbf{G} + \mathbf{GBR}^{-1}\mathbf{B}^T\mathbf{G} - \mathbf{Q} \tag{5.22}$$

(3) Phase 3 control strategy

At t_3, engine speed reaches its ignition speed $\dot{\theta}_{er}$ so engine is ignited. After ignition, engine speed is regulated by engine torque and engine clutch torque simultaneously. The target of this phase is to reduce the difference between engine speed and engine clutch speed.

PID controller is adopted to control engine torque. The control strategy is shown in Figure 5.4. The difference between target engine speed and actual engine speed is set as PID input. PID output is the required engine torque which is combined with engine clutch torque to regulate engine speed.

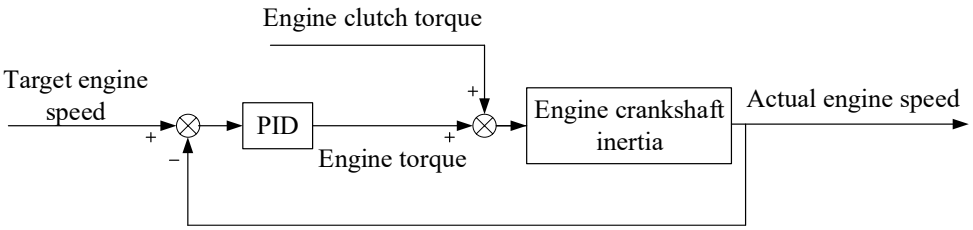

Figure 5.4. Engine speed control strategy.

Before engagement, engine clutch torque is proportional to the normal force acting on it. After engagement, engine clutch torque is determined by engine torque. Sudden clutch torque change can cause impact and vibration on vehicle powertrain, which degrades vehicle driving comfort. So engine clutch torque before and after engagement should be kept consistent [78]. The engine clutch torque needed for engine crankshaft acceleration after engagement is described as:

$$T_{ctar} = J_e \frac{a}{R_w} i_g i_f \tag{5.23}$$

where T_{ctar} is the target engine clutch torque after engagement.

Engine clutch torque should transfer to its target value smoothly to avoid powertrain impact, so a third order polynomial is adopted to design the trajectory of engine clutch torque changing from its initial value to target value [124]:

$$T_c = T_{ctar} + (T_{cinit} - T_{ctar})(1 - 3\frac{(t - t_{i3})^2}{\Delta t^2} + 2\frac{(t - t_{i3})^3}{\Delta t^3}) \tag{5.24}$$

where T_{cinit} is the engine clutch torque at the beginning of phase 3. t_{i3} is the initial time of phase 3. Δt is the designed time range for the third order polynomial. At the end of engine clutch torque control, engine clutch torque is T_{ctar}.

(4) Phase 4 control strategy

At the beginning of phase 4, engine speed regulation and engine clutch torque adjustment are both finished. Engine clutch pressure is slowly then rapidly increased. At the same time, vehicle driving torque is transferred from HPM to engine. To reduce powertrain impact and vehicle jerk, output shaft torque should change smoothly [125]. The third order polynomials are used to design HPM torque and engine torque transfer trajectories. The engine reference torque at time *t* is:

$$T_e = \frac{3\Delta T_e (t - t_{i4})^2}{\Delta t_4^{\,2}} - \frac{2\Delta T_e (t - t_{i4})^3}{\Delta t_4^{\,3}} \tag{5.25}$$

The HPM reference torque at time *t* is:

$$T_h = \Delta T_h + \frac{2\Delta T_h (t - t_{i4})^3}{\Delta t_4^{\,3}} - \frac{3\Delta T_h (t - t_{i4})^2}{\Delta t_4^{\,2}} \tag{5.26}$$

where ΔT_e is the difference between engine target torque and its initial torque in phase 4. Engine target torque is determined by driver torque demand. t_{i4} is the initial time of phase 4. Δt_4 is the time range designed for torque transfer. ΔT_h is the difference between HPM target torque and its initial toque. HPM target torque in this phase is 0.

(5) Phase 5 control strategy

In phase 5, vehicle is only driven by engine. Engine torque is determined by driver torque demand. HPM doesn't work and its torque is 0.

$$\begin{cases} T_h = 0 \\ T_e = \dfrac{T_{dri}}{i_g i_f} \end{cases} \tag{5.27}$$

5.5 **Vehicle speed control strategy**

During mode switching, vehicle dynamic performance is maintained by using HPM to compensate for engine clutch torque. Vehicle dynamic performance is indicated by a constant acceleration [78]. Vehicle acceleration is captured at the beginning of mode switching. The target vehicle speed during mode switching is described as:

$$V_{tar} = V_{in} + a_{in}\Delta t_m \tag{5.28}$$

where V_{tar} is the target vehicle speed, V_{in} is the vehicle speed at the beginning of mode switching, a_{in} is the vehicle acceleration at the beginning of mode switching. Δt_m is the time from the beginning of mode switching.

To follow the target vehicle speed, feedforward and feedback control strategy is designed. In the strategy, feedforward HPM torque is set as driver torque demand. PID controller is used for feedback control. The difference between target vehicle speed and actual vehicle speed is set as the input of PID controller, and the output of PID controller is the feedback HPM torque, final HPM torque is the combination of feedforward HPM torque and feedback HPM torque. The vehicle speed control strategy is shown in Figure 5.5.

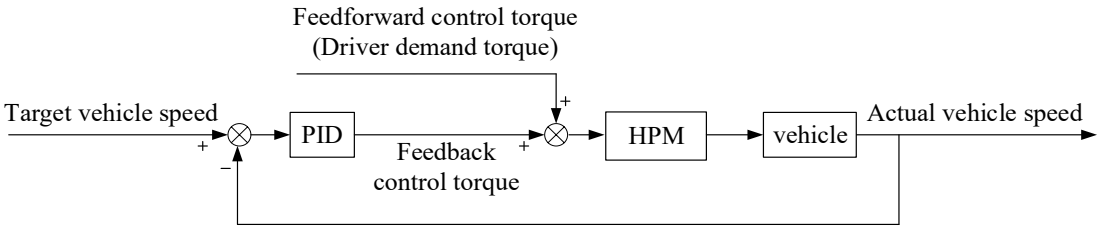

Figure 5.5. Vehicle speed control strategy.

5.6 **Simulation and analysis**

To verify the proposed mode switching control strategy, a simulation model is built in Matlab/Simulink. Simscape is used to build powertrain model and control strategy is realized with the help of Stateflow.

5.6.1 **Hydraulic launching process analysis**

Hydraulic launching process in phase 1 is shown in Figure 5.6. K is used to represent the maximum throttle changing rate, which is defined as the derivative of throttle. It is shown that with bigger maximum throttle changing rate, vehicle driving torque increases faster, which causes higher vibration to powertrain. Powertrain vibration is indicated by driveshaft speed fluctuation. Although rapidly changing torque degrades driving comfort, which is demonstrated by higher vehicle jerk in Figure 5.6(c), it helps to improve vehicle dynamic performance which is demonstrated by faster increased vehicle speed in Figure 5.6(d).

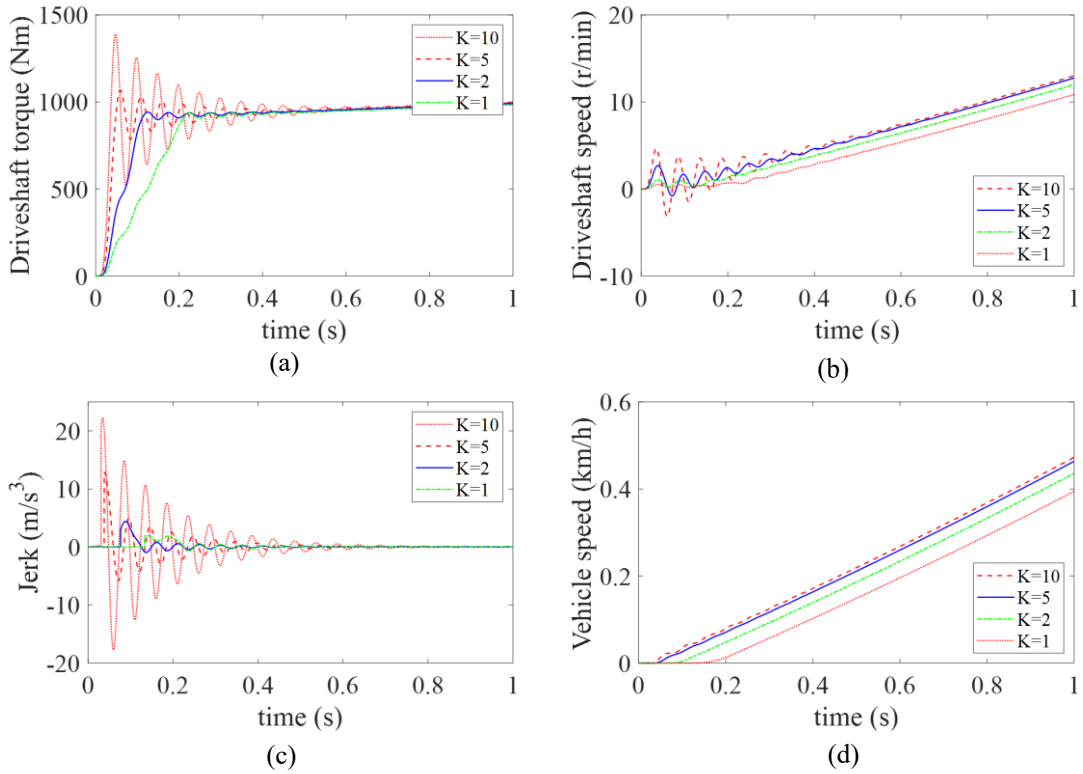

Figure 5.6. Simulation results of hydraulic launching process.

5.6.2 **Demonstration of mode switching control strategy performance**

Mode switching process simulation results are shown in Figure 5.7. Mode switching starts at 8.1 s. Engine clutch begins to engage by increasing clutch pressure, and engine crankshaft is accelerated. At the same time, HPM torque is increased to compensate engine clutch torque. Due to different torque response time of engine and HPM, driveshaft torque slightly changes and causes an impact on powertrain, which is illustrated by the fluctuating vehicle acceleration in Figure 5.7(d).

When engine speed reaches the threshold at 9.05 s, engine is ignited and starts speed regulation. Engine clutch torque is transferred to its target value following a three order polynomial. As shown in Figure 5.7(a), engine clutch reaches its target torque earlier than engine speed regulation. Then clutch pressure is kept constant until engine speed regulation is finished. In other scenarios, engine speed regulation can be faster than engine clutch torque control.

At 9.31 s, engine clutch torque control and engine speed regulation are both finished, so engine clutch is engaged. In phase 3, the target engine clutch torque is set to be the torque required for accelerating engine crank after engine clutch engagement, and the engine

clutch torque is compensated by HPM at the same time. Engine clutch engagement causes powertrain vibration, which is reflected by vehicle acceleration fluctuation in Figure 5.7(d). Engine torque and HPM torque are coordinately controlled in phase 4.

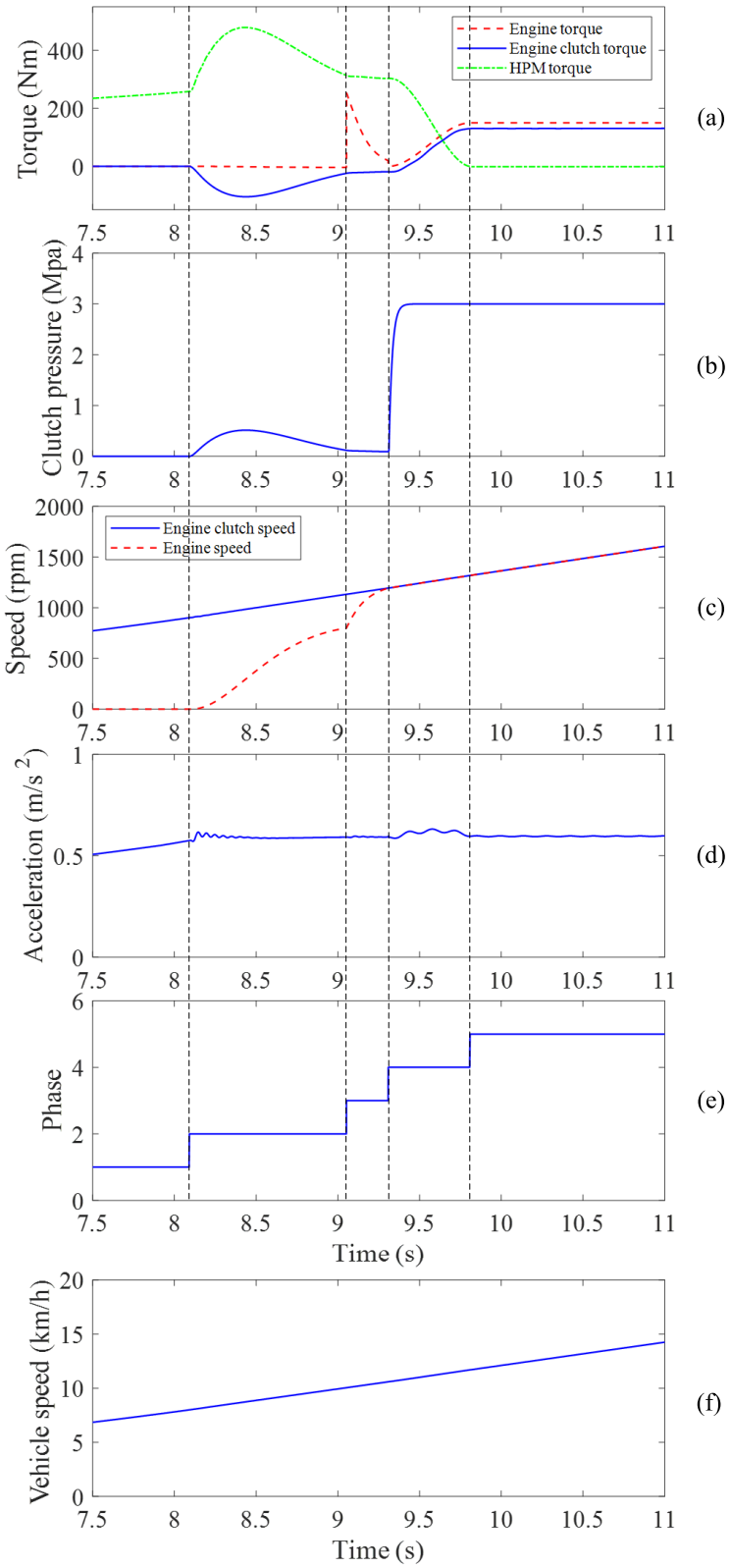

Figure 5.7. Simulation results of mode switching.

At 9.81 s, vehicle driving torque is all transferred from HPM to engine. Mode switching process is finished, and vehicle is driven by engine solely. Figure 5.7(d) shows that vehicle acceleration is maintained during mode switching, which means good vehicle dynamic performance. Figure 5.7(f) illustrates the continuously increasing vehicle speed, which also demonstrates the vehicle dynamic performance during mode switching.

5.6.3 **Vehicle speed control effect during mode switching**

To maintain vehicle dynamic performance and realize smooth mode switching, feedforward and PID feedback control strategy is adopted for vehicle speed control. The strategy is compared with only feedforward control, and results are shown in Figure 5.8. It is illustrated that with feedback control, vehicle speed is closer to the desired speed while speed error is relatively higher with only feedforward control.

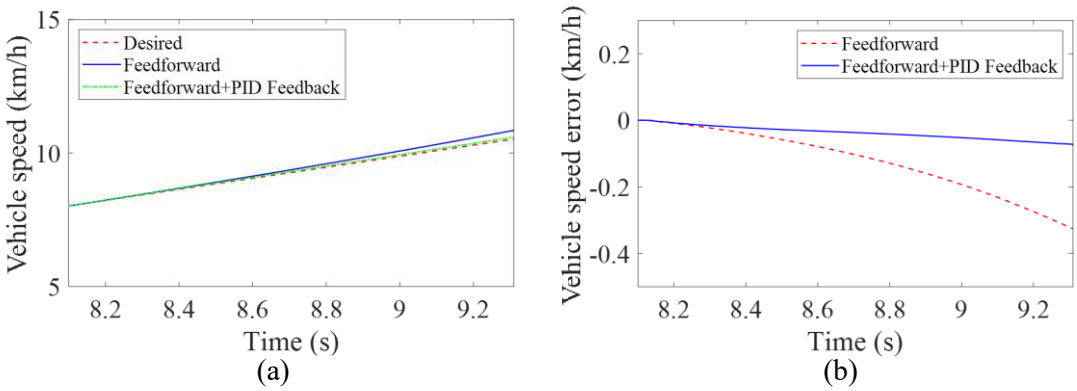

Figure 5.8. Vehicle speed control effect during mode switching.

5.6.4 **LQR control during engine speed up process**

LQR controller is used to compromise vehicle jerk and clutch frictional work during engine speed up process. Results are shown in Figure 5.9 and Figure 5.10. As shown in Figure 5.9, clutch torque changing rate and peak clutch torque are both reduced with increasing r. Engine clutch speed fluctuation is considerably higher when r =1, and decreases when r is increased. This is because when r =1, engine clutch torque increases faster. Higher clutch torque changing rate introduces more vibration on vehicle powertrain. Figure 5.10(a) and Figure 5.10(b) illustrate that slower engine clutch engagement brings less vehicle jerk while faster engine clutch engagement brings less clutch frictional work. Mode switching time is also increased due to lower clutch torque. Figure 5.10(c) and Figure 5.10(f) demonstrate the vehicle dynamic performance in all

cases. Hydraulic energy consumption is reduced with faster mode switching. This is worth to noticing in PHHV, considering the low energy density of accumulator.

The comparison gives several solutions for different driver intentions. Bigger *r* puts more demands on restricting vehicle jerk, which improves vehicle driving comfort during mode switching process. Smaller *r* allows engine clutch to engage faster so mode switching process can be finished quicker.

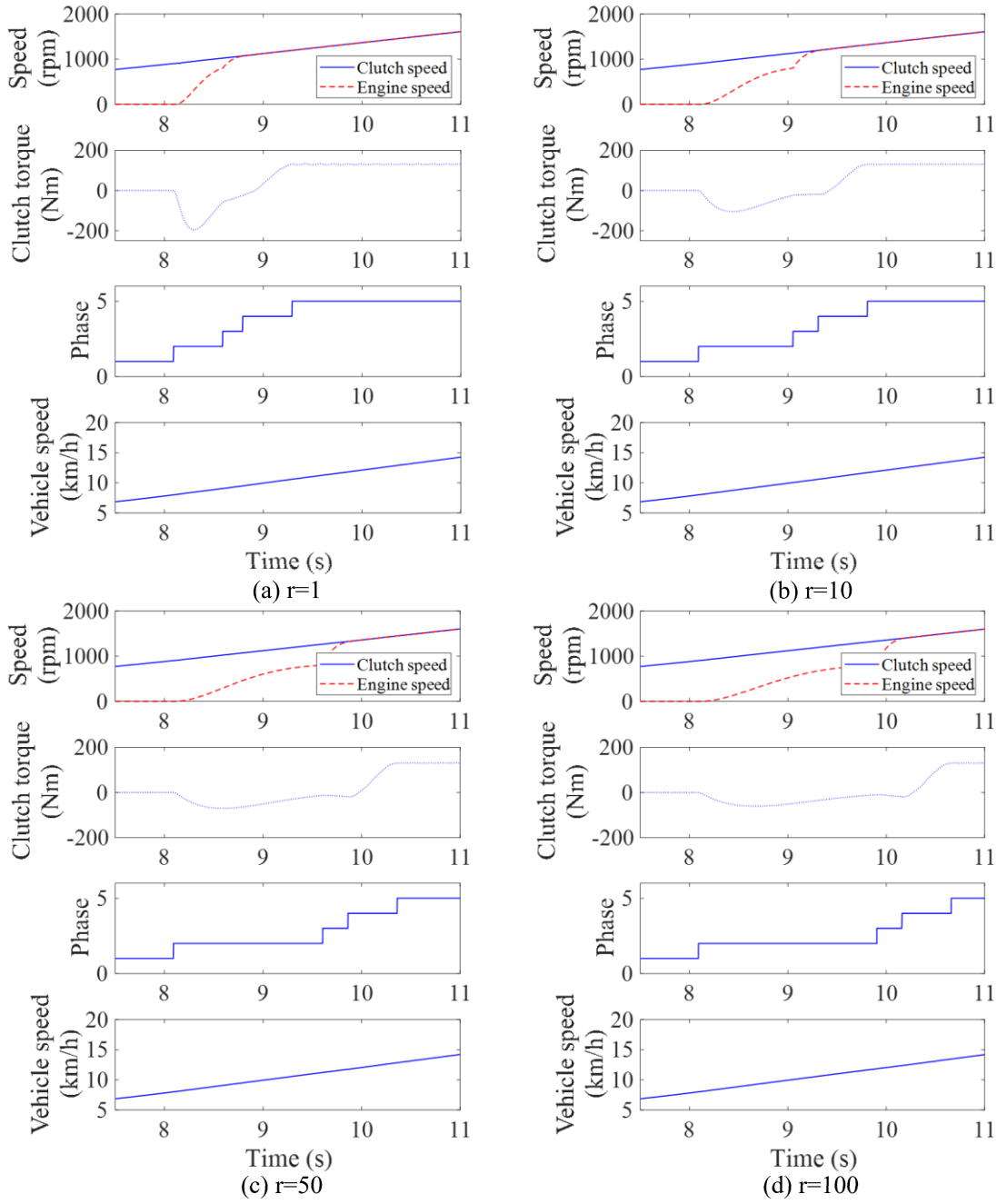

Figure 5.9. Mode switching process with different driver intention.

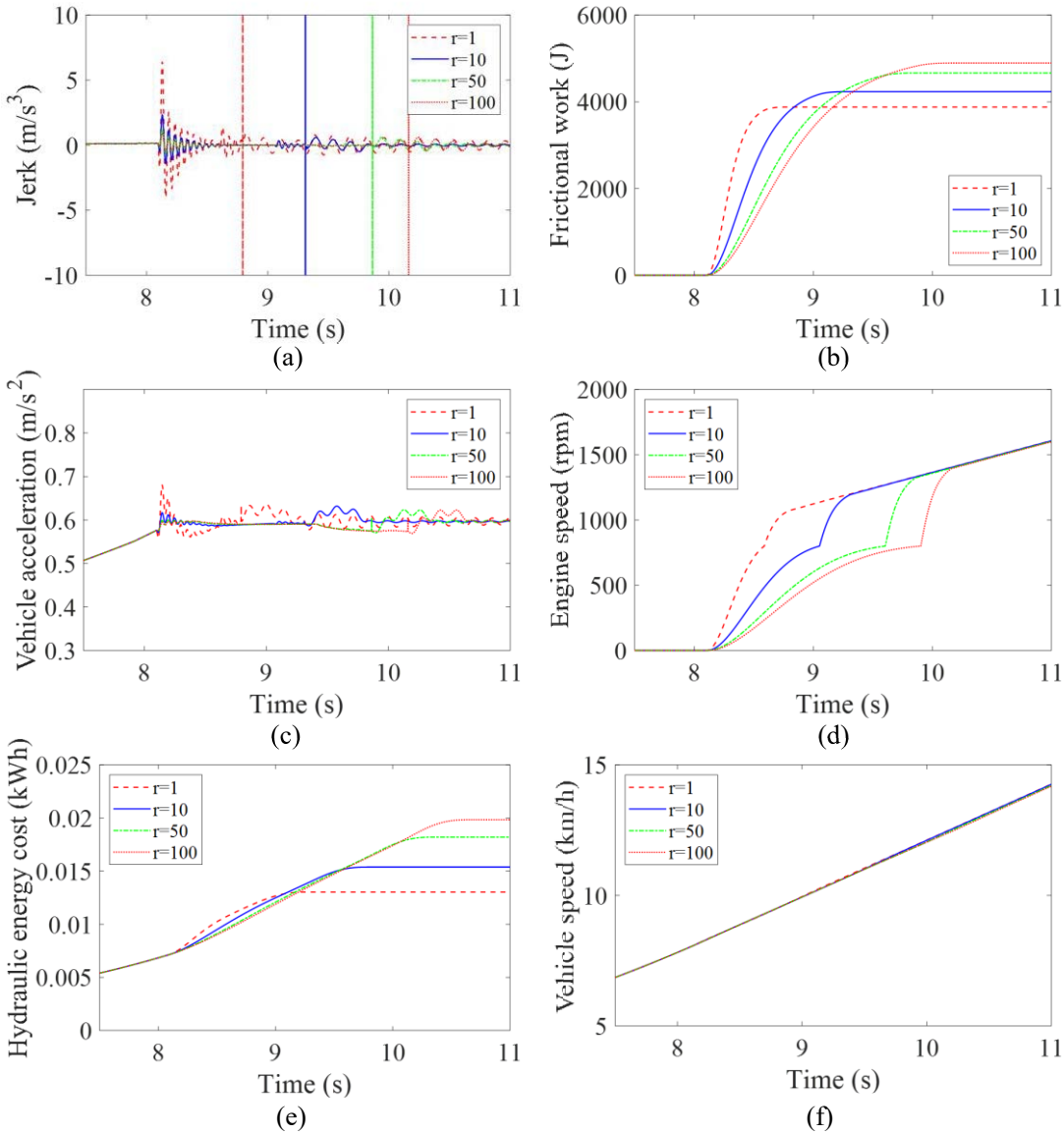

Figure 5.10. Comparison of mode switching quality.

5.7 **Summary**

In this chapter, PHHV launching and mode switching control strategy is proposed. In the control strategy, engine is started by HPM through engine clutch, and vehicle dynamic performance is maintained by HPM torque compensation. During hydraulic launching, throttle changing rate is controlled to reduce powertrain vibration. Based on LQR controller, vehicle jerk, clutch frictional work and hydraulic energy consumption can be compromised according to driver intention. It is concluded that faster mode switching brings better vehicle dynamic performance while slower mode switching brings better driving comfort. To maintain a constant vehicle acceleration during mode switching,

feedforward and feedback vehicle speed control strategy is used. With a constant vehicle acceleration, engine clutch torque is controlled to satisfy the engine acceleration requirement, so sudden driving torque change before and after engine clutch engagement is avoided.

Chapter 6 Power on gear shifting control

6.1 Introduction

In PHHV, the original engine driving powertrain is equipped with AMT. Engine clutch has to be disengaged to conduct gear shifting, so vehicle driving torque is cut off during gear shifting. The torque interruption degrades vehicle dynamic performance. Besides, it also causes excessive vibration to vehicle powertrain, which decreases vehicle driving comfort. In PHHV, HPM could be used to compensate driving torque during gear shifting.

6.2 Powertrain modelling for power on gear shifting control

Based on the modelling and vibration analysis in Chapter 4 a PHHV powertrain dynamic model is built as shown in Figure 6.1 to research powertrain vibration and vehicle dynamic performance during gear shifting. This model is described by equation (6.1) to equation (6.8):

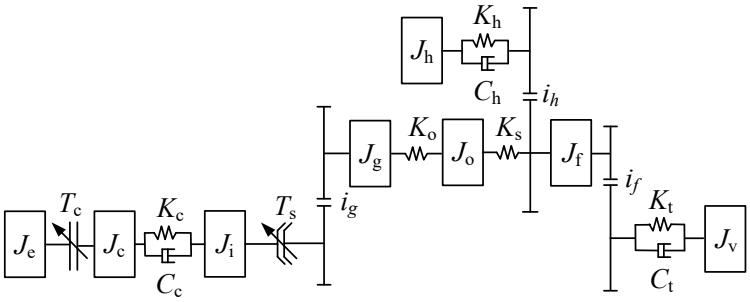

Figure 6.1. PHHV powertrain model for power on gear shifting control.

$$J_e\ddot{\theta}_e = T_e - T_c \tag{6.1}$$

$$J_c\ddot{\theta}_c = K_c(\theta_i - \theta_c) + C_c(\dot{\theta}_i - \dot{\theta}_c) + T_c \tag{6.2}$$

$$J_t\ddot{\theta}_i = T_s - K_c(\theta_i - \theta_c) - C_c(\dot{\theta}_i - \dot{\theta}_c) \tag{6.3}$$

$$J_g\ddot{\theta}_g = K_o(\theta_o - \theta_g) - T_s i_g \tag{6.4}$$

$$J_o\ddot{\theta}_o = K_s(\theta_f - \theta_o) - K_o(\theta_o - \theta_g) \tag{6.5}$$

$$\begin{aligned} J_f\ddot{\theta}_f = {} & K_t(\theta_w - \theta_f / i_f)/i_f + C_t(\dot{\theta}_w - \dot{\theta}_f / i_f)/i_f - K_s(\theta_f - \theta_o) \\ & -K_h(\theta_f i_h - \theta_h)i_h - C_h(\dot{\theta}_f i_h - \dot{\theta}_h)i_h \end{aligned} \tag{6.6}$$

$$J_h\ddot{\theta}_h = T_h + K_h(\theta_f i_h - \theta_h) + C_h(\dot{\theta}_f i_h - \dot{\theta}_h) \tag{6.7}$$

$$J_v\ddot{\theta}_w = -K_t(\theta_w - \theta_f / i_f) - C_t(\dot{\theta}_w - \dot{\theta}_f / i_f) - T_L \tag{6.8}$$

where J_g is AMT gears inertia. θ_g is angular displacement of AMT gears on output shaft. T_s is synchronizer torque.

6.3 **Power on gear shifting control strategy design**

Before gear shifting, engine drives vehicle according to the diver torque demand:

$$T_e = \frac{T_{dri}}{i_g i_f} \tag{6.9}$$

During power on gear shifting process, HPM replaces engine to provide vehicle driving torque when engine clutch is disengaged. In this step, engine torque is gradually decreased and HPM torque is increased simultaneously. Engine torque and HPM torque are combined at driveshaft. Thus to keep vehicle dynamic performance, driveshaft torque should be maintained during gear shifting. In torque transfer phase, engine and HPM torque changing rates satisfy the following equation:

$$\Delta T_h = \frac{\Delta T_e i_g}{i_h} \tag{6.10}$$

Rapid driving torque variation causes vibration to vehicle powertrain. So third order polynomials are adopted to control the toque transfer process [126]. Engine torque and HPM torque trajectories during torque transfer process are dominated by equation (6.11) and equation (6.12) , as shown in Figure 6.2.

$$T_e = T_{ei} - \frac{3T_{ei}(t-t_i)^2}{\Delta t^2} + \frac{2T_{ei}(t-t_i)^3}{\Delta t^3} \tag{6.11}$$

$$T_h = \left(\frac{3T_{ei}(t-t_i)^2}{\Delta t^2} - \frac{2T_{ei}(t-t_i)^3}{\Delta t^3} \right) \frac{i_g}{i_h} \tag{6.12}$$

In the equations, T_{ei} is the engine torque when torque transfer process starts, Δt is the time range designed for torque transfer, t_i is the time when torque transfer process starts.

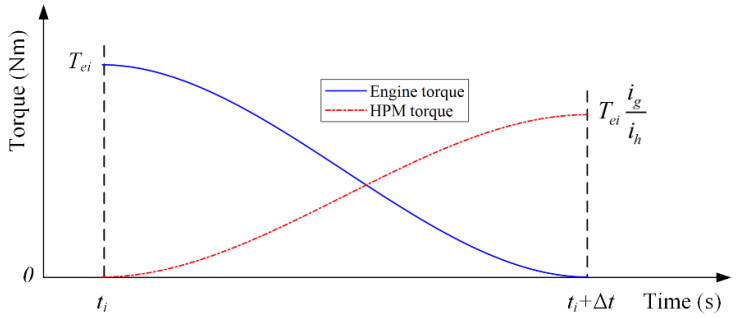

Figure 6.2. Trajectories of engine and HPM torque during torque transfer.

When engine torque is reduced to zero, engine clutch is disengaged. Then, synchronizer is disengaged from the original gear and engaged to the target gear. After gear shifting is finished, engine clutch is engaged again and engine torque is restored.

During engine clutch engagement process, engine clutch torque also works on vehicle powertrain so it should be compensated by HPM otherwise it will generate impact on vehicle powertrain:

$$T_h = \frac{T_{dri}}{i_f i_h} - T_c \frac{i_g}{i_h} \tag{6.13}$$

As previously mentioned in mode switching control, engine clutch torque is controlled by its normal force when slipping but determined by engine torque when engaged. If engine clutch torque changes a lot before and after engagement, significant vibration will occur on vehicle powertrain. Therefore, LQR controller is again adopted here for engine clutch engagement control.

In LQR control, the state variables are selected as:

$$\mathbf{X} = [\dot{\theta}_e - \dot{\theta}_c, T_e, T_c, T_e - T_c]^T \tag{6.14}$$

The control variables are selected as:

$$\mathbf{U} = [\dot{T}_e, \dot{T}_c]^T \tag{6.15}$$

According to PHHV powertrain model described by equation (6.1) to equation (6.8), the following state space function is attained:

$$\dot{\mathbf{X}} = \mathbf{AX} + \mathbf{BU} + \mathbf{E} \tag{6.16}$$

$$\mathbf{A} = \begin{bmatrix} 0 & \frac{1}{J_e} & -\frac{1}{J_e} & 0 \\ 0 & 0 & 0 & 0 \\ 0 & 0 & 0 & 0 \\ 0 & 0 & 0 & 0 \end{bmatrix}, \ \mathbf{B} = \begin{bmatrix} 0 & 0 \\ 1 & 0 \\ 0 & 1 \\ 1 & -1 \end{bmatrix}, \ \mathbf{E} = \begin{bmatrix} -\ddot{\theta}_c \\ 0 \\ 0 \\ 0 \end{bmatrix} \tag{6.17}$$

The cost function of LQR control is described by:

$$j = \frac{1}{2} \int_{t_{i1}}^{t_{f1}} \left[\mathbf{X}^T \mathbf{Q} \mathbf{X} + \mathbf{U}^T \mathbf{R} \mathbf{U} \right] dt \tag{6.18}$$

where t_{i1} and t_{f1} are the start and finish time of engine clutch engagement process. **Q** and **R** are weighing matrices. In power on gear shifting control, the weighing matrices are selected as following:

$$\mathbf{Q}=\begin{bmatrix} q_{11} & 0 & q_{13} & 0 \\ 0 & 0 & 0 & 0 \\ q_{31} & 0 & 0 & 0 \\ 0 & 0 & 0 & q_{44} \end{bmatrix},\ \mathbf{R}=\begin{bmatrix} r_{11} & 0 \\ 0 & r_{22} \end{bmatrix} \tag{6.19}$$

With the weighing matrices, the cost function is attained as equation (6.20). $q_{11}(\dot{\theta}_e-\dot{\theta}_c)^2$ aims to reduce the engine and engine clutch speed difference. $q_{13}(\dot{\theta}_e-\dot{\theta}_c)T_c$ aims to reduce clutch frictional work. $q_{44}(T_e-T_c)^2$ aims to reduce the engine clutch torque difference before and after engagement. $r_{11}\dot{T}_e^2$ aims to restrict engine torque changing rate. $r_{22}\dot{T}_c^2$ aims to restrict engine clutch torque changing rate to reduce powertrain vibration. q_{11}, q_{13}, q_{31}, q_{44}, r_{11} and r_{22} are weighing factors. $q_{13}=q_{31}$. Lager weighing factor means stronger intention of restricting the corresponding variable.

$$j=\frac{1}{2}\int_{t_{i1}}^{t_{f1}}\left[q_{11}(\dot{\theta}_e-\dot{\theta}_c)^2+2q_{13}(\dot{\theta}_e-\dot{\theta}_c)T_c+q_{44}(T_e-T_c)^2+r_{11}\dot{T}_e^2+r_{22}\dot{T}_c^2\right]dt \tag{6.20}$$

The LQR control variables are determined by equation (6.21):

$$\mathbf{U}=-\mathbf{R}^{-1}\mathbf{B}^T\mathbf{G}\mathbf{X} \tag{6.21}$$

where **G** is the feedback matrix and is obtained by solving the Riccati equation:

$$\mathbf{0}=-\mathbf{G}\mathbf{A}-\mathbf{A}^T\mathbf{G}+\mathbf{G}\mathbf{B}\mathbf{R}^{-1}\mathbf{B}^T\mathbf{G}-\mathbf{Q} \tag{6.22}$$

HPM torque is transferred back to engine after engine clutch is engaged. The third order polynomial is used to mitigate powertrain vibration. Power on upshifting control strategy is illustrated in Figure 6.3 as a flowchart.

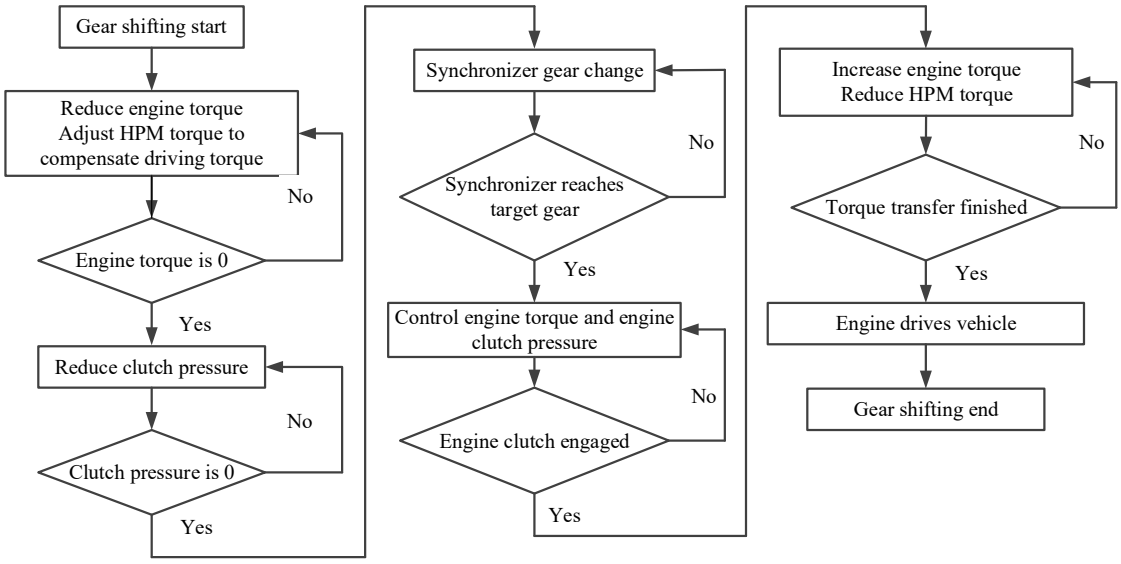

Figure 6.3. Power on upshifting control strategy.

Power on downshifting process is similar to power on upshifting process as shown in Figure 6.5. However, in downshifting process, the target gear has a larger gear ratio, which means engine speed should be increased after gear shifting. So engine torque is used for its speed regulation. PID controller is adopted for engine speed regulation during power on downshifting, as shown in Figure 6.4:

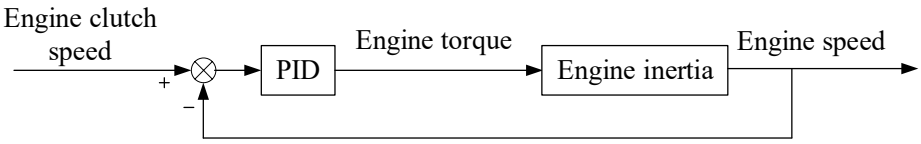

Figure 6.4. Engine speed regulation control strategy.

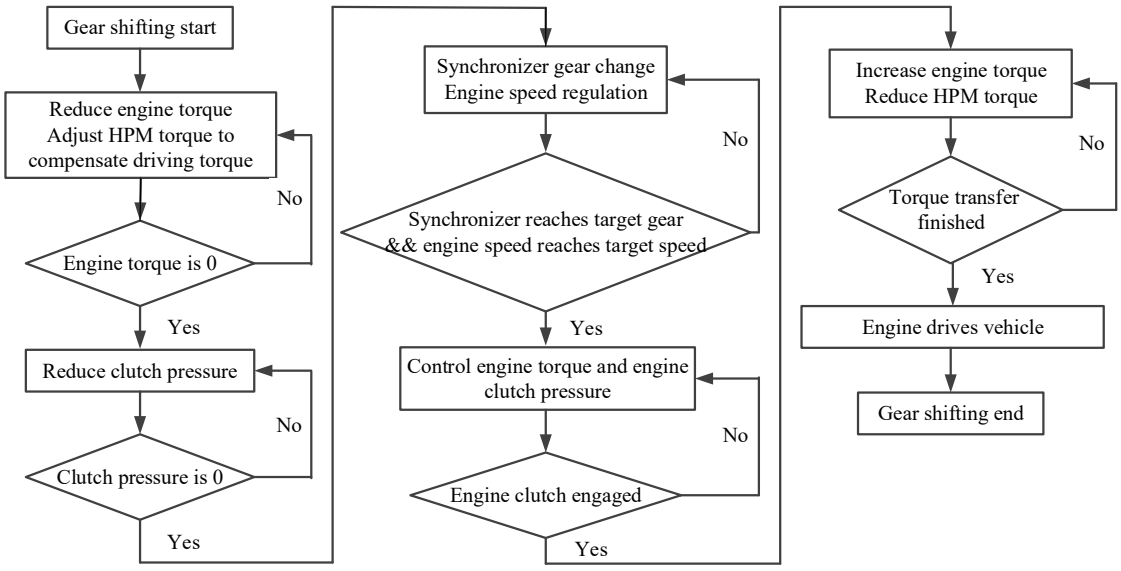

Figure 6.5. Power on downshifting control strategy.

6.4 **Power on gear shifting simulation and analysis**

PHHV simulation model is built with Matlab/Simulink and power on gear shifting is simulated to validate the power on gear shifting control strategy. The 3rd gear to 4th gear upshifting and the 6th gear to 5th downshifting are simulated and analyzed as representatives of power on gear shifting. Simulation results are shown in Figure 6.6 and Figure 6.7.

From Figure 6.6(a), when upshifting starts, engine torque decreases and HPM torque increases. So vehicle driving torque is maintained. When torque transfer is finished, engine clutch is disengaged. Then, synchronizer is disengaged from the 3rd gear and engaged to the 4th gear. Figure 6.6(c) depicts the engine clutch speed synchronization

process. At the beginning of synchronization, AMT input shaft speed is same as the 3rd gear speed and then adjusted by the synchronizer cone clutch torque. The synchronizer cone clutch torque causes slight vibration to vehicle powertrain, which can be found from the fluctuating gear speeds in Figure 6.6(c). When AMT input shaft speed equals the 4th gear speed, synchronizer is engaged to the 4th gear. Because the 3rd gear has higher gear ratio than the 4th gear, AMT input shaft speed is reduced after gear change. Engine speed has to be reduced to engage engine clutch. As shown in Figure 6.6(b), engine clutch pressure is increased under the control of LQR controller and engine speed is reduced by engine clutch torque. Engine clutch pressure decreases to a small value when engine and engine clutch speeds are close. So that engine clutch torque doesn't change a lot after clutch engagement and large vehicle powertrain vibration is avoided. Engine clutch torque also works on vehicle powertrain, which brings extra driving torque to vehicle. So HPM torque is reduced to maintain a stable vehicle dynamic performance. The stable vehicle acceleration in Figure 6.6(f) demonstrates the effectiveness of HPM torque control on stabilizing vehicle dynamic performance.

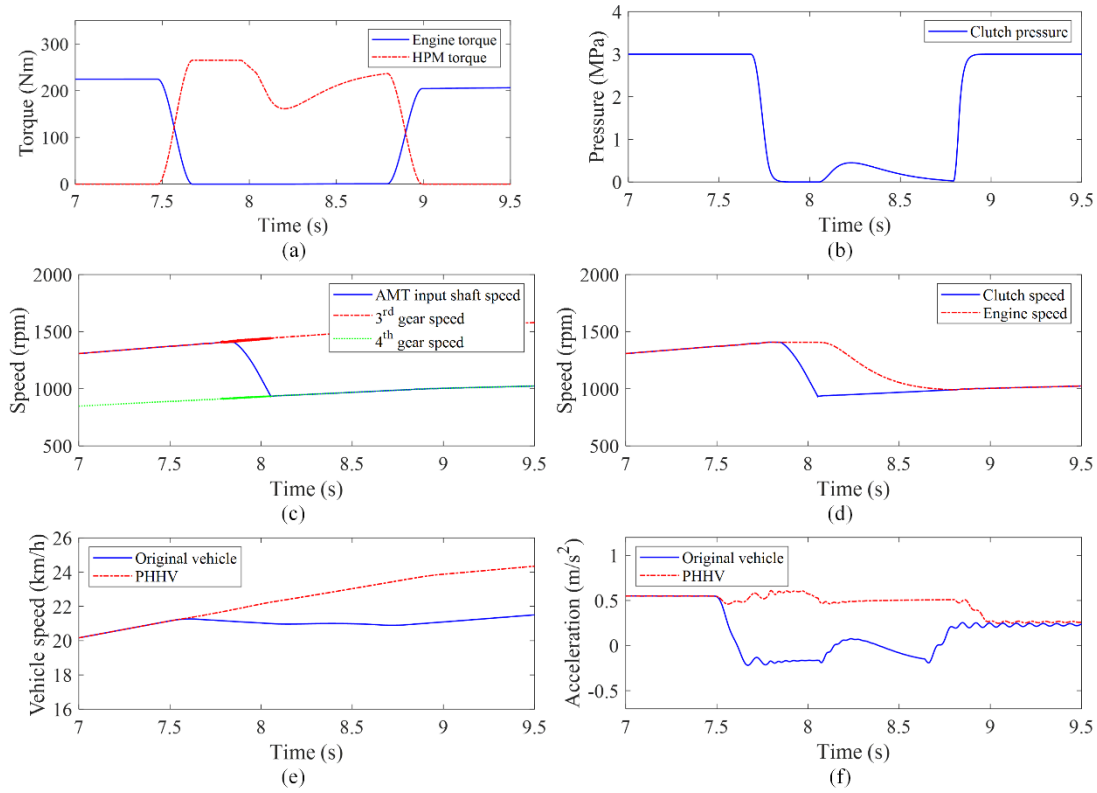

Figure 6.6. 3rd gear to 4th gear upshifting process.

PHHV dynamic performance during gear shifting is compared with the original vehicle. In original vehicle, there is no torque compensation during gear shifting, so vehicle

dynamic performance is degraded due to torque interruption. Figure 6.6(f) illustrates that PHHV acceleration is maintained during gear shifting while the original vehicle acceleration drops remarkably. Vehicle speed in Figure 6.6(e) also demonstrates that PHHV speed keeps increasing owning to torque compensation, but original vehicle speed is decreased due to resistance.

Figure 6.7 shows the 6th gear to the 5th gear downshifting process which is used to demonstrate the high speed overtaking scenario. During downshifting process, HPM is also used to compensate for driving torque to maintain vehicle dynamic performance. As mentioned before, in downshifting, engine clutch speed is higher than engine speed after synchronizer is engaged to the target gear, so engine torque is used for its own speed regulation. When engine speed and engine clutch speed are synchronized, engine clutch pressure increases under the control of LQR controller. Because the speed difference has been cancelled by engine speed regulation, engine clutch is engaged in a very short time. From Figure 6.7(f), it is found that during power on gear shifting, PHHV acceleration is maintained but the original vehicle dynamic performance is deteriorated due to torque interruption.

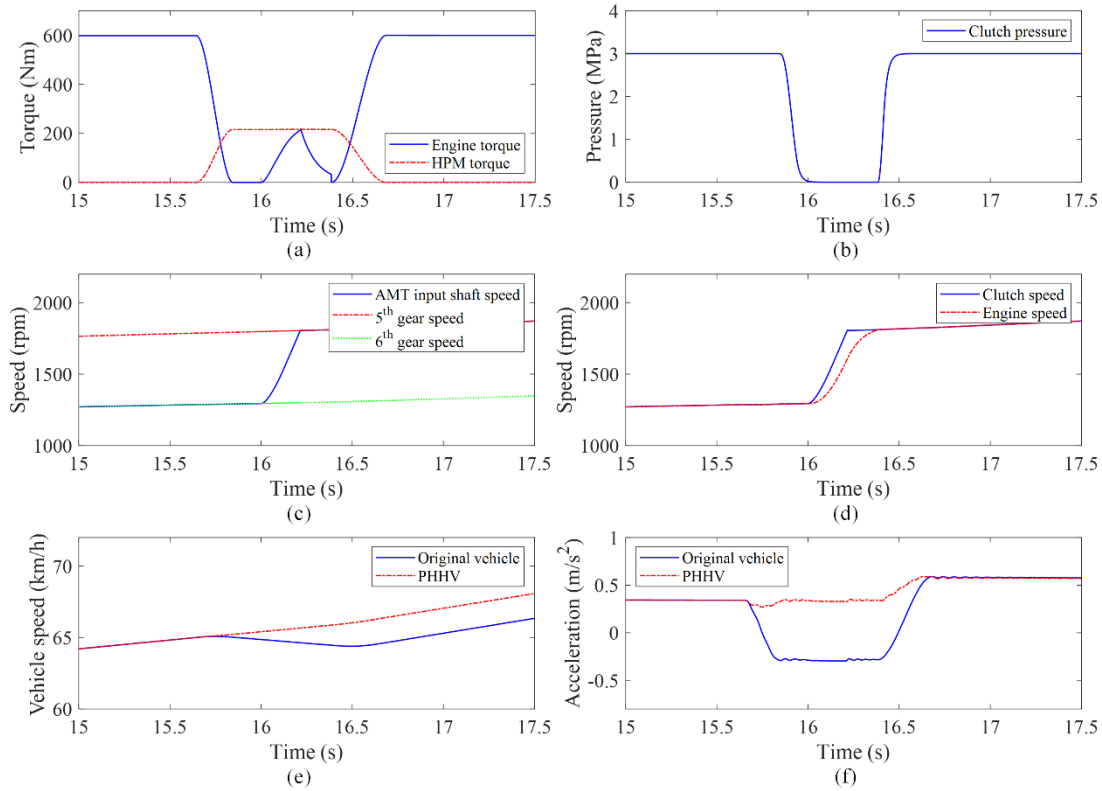

Figure 6.7. 6th gear to 5th gear downshifting process.

6.5 Powertrain state estimation based on EKF

6.5.1 EKF state estimator design

During power on gear shifting process as well as mode switching process, engine clutch engagement control is the most complicated part. In engine clutch engagement process, engine torque, engine clutch torque and HPM torque need to be coordinately controlled by LQR controller. To implement LOR controller, engine torque, engine speed, engine clutch torque, engine clutch speed, HPM torque and vehicle speed should be known as state feedback. In real vehicle applications, clutch torque and speed couldn't be measured directly. Engine speed, HPM speed, AMT input shaft speed and wheel speed could be measured by onboard sensors. Engine torque and HPM torque could be calibrated by engine throttle and by HPM swashplate angle which are also measurable [127, 128]. However, the measured values contain noise which affects control effect. Engine torque and HPM torque uncertainties also introduce transfer noise to gear shifting control process [129]. In this part, EFK is used to estimate engine clutch states and reduce the noise effect.

In engine clutch engaging process, synchronizer is engaged, so PHHV model in Figure 6.1 is described by the following equation:

$$\mathbf{J}\ddot{\boldsymbol{\theta}} + \mathbf{C}\dot{\boldsymbol{\theta}} + \mathbf{K}\boldsymbol{\theta} = \mathbf{T} \tag{6.23}$$

In equation (6.23), the matrices are:

$$\mathbf{J} = diag\left[J_e, J_c, J_i + \frac{J_g}{i_g^2}, J_o, J_f, J_h, J_v \right],\ \boldsymbol{\theta} = [\theta_e, \theta_c, \theta_i, \theta_o, \theta_f, \theta_h, \theta_w]^T$$

$$\mathbf{C} = \begin{bmatrix} 0 & 0 & 0 & 0 & 0 & 0 & 0 \\ 0 & C_c & -C_c & 0 & 0 & 0 & 0 \\ 0 & -C_c & C_c & 0 & 0 & 0 & 0 \\ 0 & 0 & 0 & 0 & 0 & 0 & 0 \\ 0 & 0 & 0 & 0 & \frac{C_t}{i_f^2} + C_h i_h^2 & -C_h i_h & -\frac{C_t}{i_f} \\ 0 & 0 & 0 & 0 & -C_h i_h & c_h & 0 \\ 0 & 0 & 0 & 0 & -\frac{C_t}{i_f} & 0 & c_t \end{bmatrix},\ \mathbf{T} = \begin{bmatrix} T_e - T_c \\ T_c \\ 0 \\ 0 \\ 0 \\ T_h \\ -T_L \end{bmatrix}$$

$$\mathbf{K}=\begin{bmatrix} 0 & 0 & 0 & 0 & 0 & 0 & 0 \\ 0 & K_c & -K_c & 0 & 0 & 0 & 0 \\ 0 & -K_c & K_c+\dfrac{K_o}{i_g^2} & -\dfrac{K_o}{i_g} & 0 & 0 & 0 \\ 0 & 0 & -\dfrac{K_o}{i_g} & K_o+K_s & -K_s & 0 & 0 \\ 0 & 0 & 0 & -K_s & K_s+\dfrac{K_t}{i_f^2}+K_h i_h^2 & -K_h i_h & -\dfrac{K_t}{i_f} \\ 0 & 0 & 0 & 0 & -K_h i_h & K_h & 0 \\ 0 & 0 & 0 & 0 & -\dfrac{K_t}{i_f} & 0 & K_t \end{bmatrix}$$

In EKF state estimator design, the state variables are selected as:

$$\boldsymbol{x}=\left[\boldsymbol{\theta},\dot{\boldsymbol{\theta}},T_e,T_c,T_h\right]^T \tag{6.24}$$

The control variables are augmented as:

$$\boldsymbol{u}=\left[\dot{T}_e,\dot{T}_c,\dot{T}_h\right]^T \tag{6.25}$$

According to the powertrain dynamic model, the state space function is described as:

$$\dot{\boldsymbol{x}}=\boldsymbol{a}\boldsymbol{x}+\boldsymbol{b}\boldsymbol{u}+\boldsymbol{v} \tag{6.26}$$

$$\begin{gathered}\boldsymbol{a}=\begin{bmatrix} \mathbf{0}_{7\times7} & \mathbf{I}_{7\times7} & \mathbf{0}_{7\times3} \\ -\mathbf{J}^{-1}\mathbf{K} & -\mathbf{J}^{-1}\mathbf{C} & \mathbf{J}^{-1}\mathbf{N} \\ & \mathbf{0}_{3\times17} & \end{bmatrix},\ \boldsymbol{b}=\begin{bmatrix} & 1 & 0 & 0 \\ \mathbf{0}_{3\times13} & 0 & 1 & 0 \\ & 0 & 0 & 1 \end{bmatrix}^T,\ \boldsymbol{v}=\begin{bmatrix} \mathbf{0}_{13\times1} \\ -T_L/J_v \\ \mathbf{0}_{3\times1} \end{bmatrix}, \\ \mathbf{N}=\begin{bmatrix} 1 & 0 & 0 & 0 & 0 & 0 & 0 \\ -1 & 1 & 0 & 0 & 0 & 0 & 0 \\ 0 & 0 & 0 & 0 & 0 & 1 & 0 \end{bmatrix}^T\end{gathered} \tag{6.27}$$

From the LQR controller, the augmented control variables are determined by the state variables as described in following equation:

$$\begin{gathered}\boldsymbol{u}=\begin{bmatrix} \dot{T}_e \\ \dot{T}_c \\ \dot{T}_h \end{bmatrix}=\begin{bmatrix} \mathbf{U} \\ \dot{T}_h \end{bmatrix}=\begin{bmatrix} -\mathbf{R}^{-1}\mathbf{B}^T\mathbf{G}(1,:) \\ -\mathbf{R}^{-1}\mathbf{B}^T\mathbf{G}(2,:) \\ \mathbf{R}^{-1}\mathbf{B}^T\mathbf{G}(2,:)\,i_g/i_h \end{bmatrix}\mathbf{X}=\boldsymbol{s}\boldsymbol{m}\boldsymbol{x}, \\ \boldsymbol{m}=\begin{bmatrix} & 1 & -1 & 0 & 0 & 0 & 0 & 0 & 0 & 0 & 0 \\ \mathbf{0}_{4\times7} & 0 & 0 & 0 & 0 & 0 & 0 & 0 & 1 & 0 & 0 \\ & 0 & 0 & 0 & 0 & 0 & 0 & 0 & 0 & 1 & 0 \\ & 0 & 0 & 0 & 0 & 0 & 0 & 0 & 1 & -1 & 0 \end{bmatrix},\boldsymbol{s}=\begin{bmatrix} -\mathbf{R}^{-1}\mathbf{B}^T\mathbf{G}(1,:) \\ -\mathbf{R}^{-1}\mathbf{B}^T\mathbf{G}(2,:) \\ \mathbf{R}^{-1}\mathbf{B}^T\mathbf{G}(2,:)\,i_g/i_h \end{bmatrix}\end{gathered} \tag{6.28}$$

The state space function could be converted to:

$$\dot{\boldsymbol{x}} = (\boldsymbol{a} + \boldsymbol{bsm})\boldsymbol{x} + \boldsymbol{v}(\boldsymbol{x}) + \boldsymbol{l} \tag{6.29}$$

where $\boldsymbol{l}$ is the process noise caused by model uncertainties. It is defined as white Gaussian noise with zero mean and covariance matrix of $\boldsymbol{L}$.

The measurable PHHV powertrain states are selected as the output variables as shown in equation (6.30) and the output function is described by equation (6.31).

$$\boldsymbol{y} = \left[\dot{\theta}_e, \dot{\theta}_i, \dot{\theta}_h, \dot{\theta}_w, T_e, T_h\right]^T \tag{6.30}$$

$$\boldsymbol{y} = \mathbf{H}\boldsymbol{x} + \boldsymbol{w} \tag{6.31}$$

where $\boldsymbol{y}$ are output variables, $\mathbf{H}$ is output matrix as shown in equation (6.32). $\boldsymbol{w}$ denotes the measurement noise which is modelled as white Gaussian noise with zero mean and covariance matrix of $\boldsymbol{W}$.

$$\mathbf{H} = \begin{bmatrix} & 1 & 0 & 0 & 0 & 0 & 0 & 0 & 0 & 0 & 0 \\ & 0 & 0 & 1 & 0 & 0 & 0 & 0 & 0 & 0 & 0 \\ \mathbf{0}_{6\times 7} & 0 & 0 & 0 & 0 & 0 & 1 & 0 & 0 & 0 & 0 \\ & 0 & 0 & 0 & 0 & 0 & 0 & 1 & 0 & 0 & 0 \\ & 0 & 0 & 0 & 0 & 0 & 0 & 0 & 1 & 0 & 0 \\ & 0 & 0 & 0 & 0 & 0 & 0 & 0 & 0 & 0 & 1 \end{bmatrix} \tag{6.32}$$

To implement EKF, the state space function and output function are discretized. EKF includes prediction process and correction process [130]. In prediction process, the predicted posterior state variables $\hat{\boldsymbol{x}}_{k+1}$ are computed based on the prior state variables:

$$\hat{\boldsymbol{x}}_{k+1} = f\left(\boldsymbol{x}_k\right) \tag{6.33}$$

The predicted error covariance matrix $\hat{\mathbf{P}}_{k+1}$ is computed by the prior error covariance matrix $\mathbf{P}_k$ and the Jacobian matrix deduced from the linearization of state space function, as described in equation (6.34) and equation (6.35).

$$\hat{\mathbf{P}}_{k+1} = \mathbf{F}_k \mathbf{P}_k \mathbf{F}_k^T + \boldsymbol{L} \tag{6.34}$$

$$\mathbf{F}_k = \left.\frac{\partial f}{\partial \boldsymbol{x}}\right|_{\boldsymbol{x}_k} = \boldsymbol{a} + \boldsymbol{bsm} - \left.\frac{\partial T_L}{J_v \partial \boldsymbol{x}}\right|_{\boldsymbol{x}_k} \tag{6.35}$$

In the correction process, the EKF filter gain $\mathbf{K}_{k+1}$ is attained from the predicted error covariance matrix and the output matrix as well as the measurement noise covariance matrix:

$$\mathbf{K}_{k+1} = \hat{\mathbf{P}}_{k+1}\mathbf{H}^T\left(\mathbf{H}\hat{\mathbf{P}}_{k+1}\mathbf{H}^T + \boldsymbol{W}\right)^{-1} \tag{6.36}$$

The state variables at step k+1 are then computed from the predicted state variables and the measured output variables as described by equation (6.37). The error covariance matrix is updated based on the EKF filter gain and the predicted error covariance matrix as shown in equation (6.38).

$$\boldsymbol{x}_{k+1} = \hat{\boldsymbol{x}}_{k+1} + \mathbf{K}_{k+1}\left(\boldsymbol{y}_{k+1} - \mathbf{H}\hat{\boldsymbol{x}}_{k+1}\right) \tag{6.37}$$

$$\mathbf{P}_{k+1} = \left(\mathbf{I} - \mathbf{K}_{k+1}\mathbf{H}\right)\hat{\mathbf{P}}_{k+1} \tag{6.38}$$

6.5.2 **EKF state estimator simulation and analysis**

EKF is used to estimate the PHHV powertrain state for engine clutch engagement control. Figure 6.8 to Figure 6.10 show the simulation results during upshifting from 3rd gear to 4th gear as an example. In LQR controller, engine speed, engine torque, engine clutch speed, engine clutch torque and HPM torque are required as state feedback. Wheel speed is observed as an indicator of vehicle dynamic performance. Figure 6.8 shows engine state estimation results. The measured value, model computed value and EKF estimated value are compared. In real application, sensors measure the states of powertrain components and the obtained signals are the real values accompanied by noise. So in simulation, the real components' states are firstly obtained directly from model which is defined as the model value in figures. Then noise is added to model value to represent sensor noise in real application. So the simulated measured signals are constructed which is defined as the measured value in figures. EKF is applied based on the measured value and the estimated states are obtained which are defined as the EKF estimated value in figures. It could be found the measured engine speed and torque fluctuates significantly due to noise. With the help of EKF, engine speed and torque are corrected to be close to the real value. The small speed error and torque error between the model computed value and EKF estimated value demonstrate the EKF effectiveness. Figure 6.9 shows EKF is capable of HPM torque and wheel speed estimation. Engine clutch speed and torque couldn't be measured directly so need to be estimated by other measurable states. Figure 6.10 illustrates engine clutch speed and torque are estimated correctly which provides proper powertrain states for LQR controller.

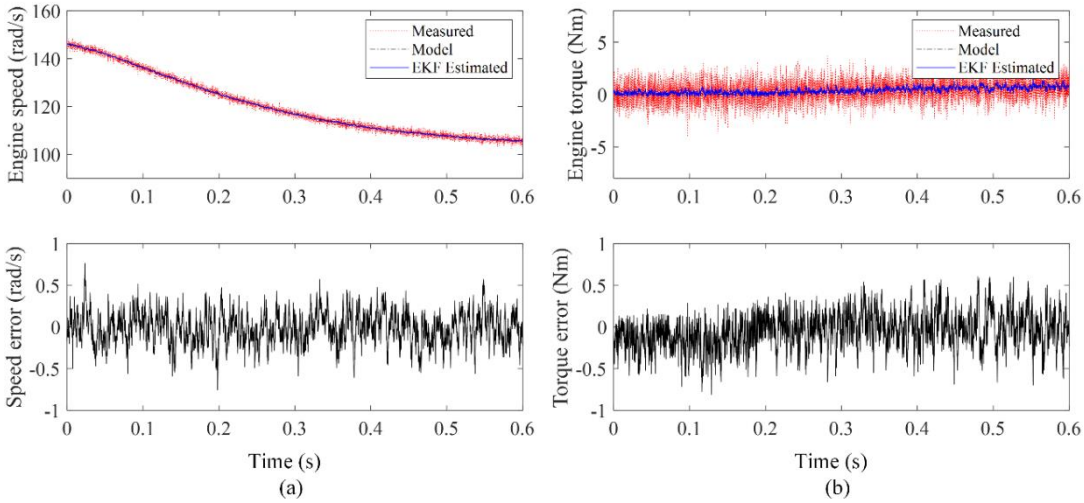

Figure 6.8. Engine state estimation, (a) Speed, (b) Torque.

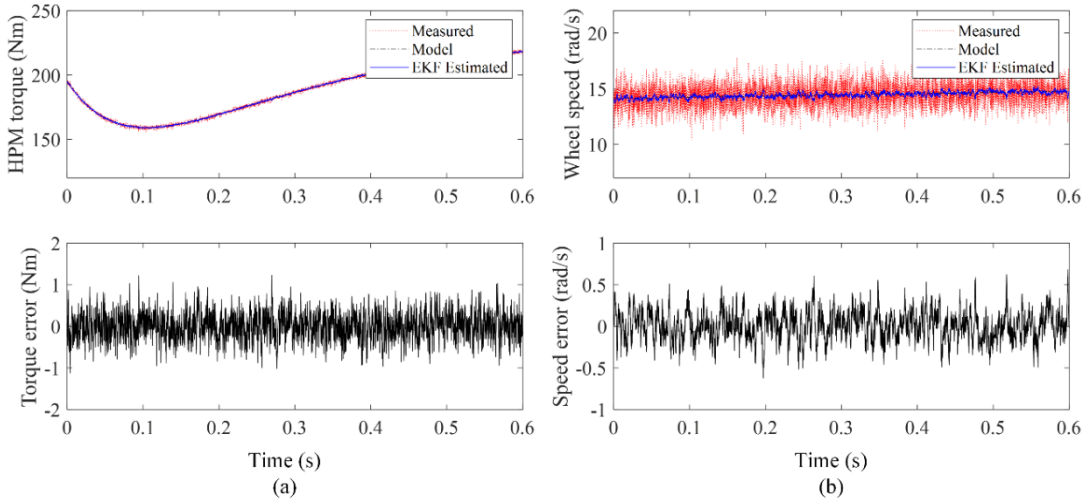

Figure 6.9. (a) HPM torque estimation, (b) Wheel speed estimation.

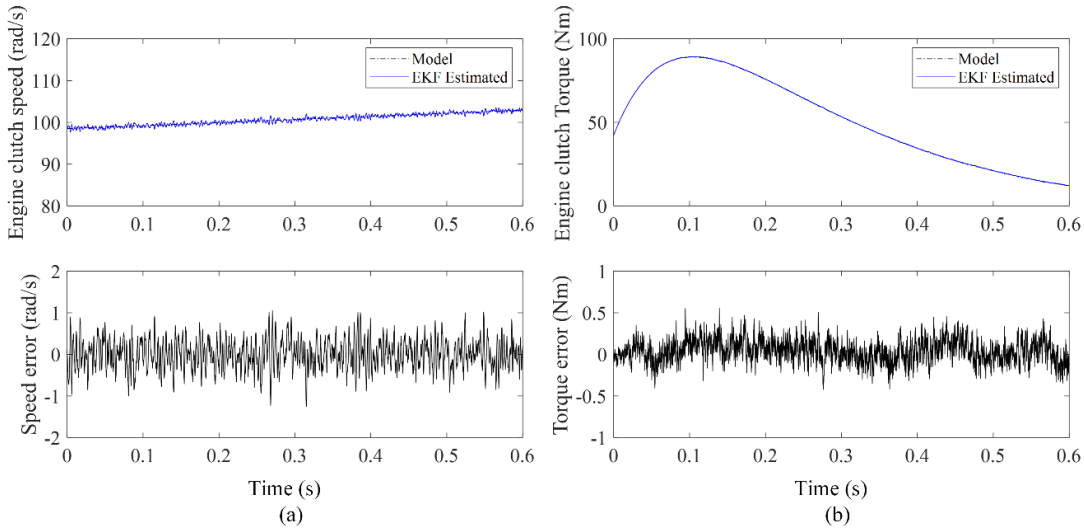

Figure 6.10. Engine clutch state estimation, (a) Speed, (b) Torque.

6.6 **HPM torque compensation capability analysis during power on gear shifting**

HPM working pressure determines its capability for torque compensation. During working condition, HPM working pressure could range from 17 MPa to 40 MPa, which means the available HPM torque varies a lot under different accumulator charging states. So it is necessary to investigate the HPM torque compensation capability for power on gear shifting.

6.6.1 **Capability analysis based on designed gear shifting schedule**

According to the designed gear shifting schedule, traction force of all gear shifting points are extracted and shown in Figure 6.11. Traction force need to be compensated during power on gear shifting. The available HPM traction force with maximum and minimum HPA working pressure is drawn in Figure 6.11 and compared with the required traction force. It is shown that when HPM works with its maximum working pressure of 40 MPa, most of the traction force during gear shifting could be compensated by HPM. The 1st gear to 2nd gear upshifting, 2nd gear to 3rd gear upshifting, 3rd gear to 4th gear upshifting and 2nd gear to 1st gear downshifting torque compensation couldn't be fully satisfied at high throttle. When HPM works with the minimum working pressure of 17 MPa, it is capable to compensate for driving torque with lower throttle.

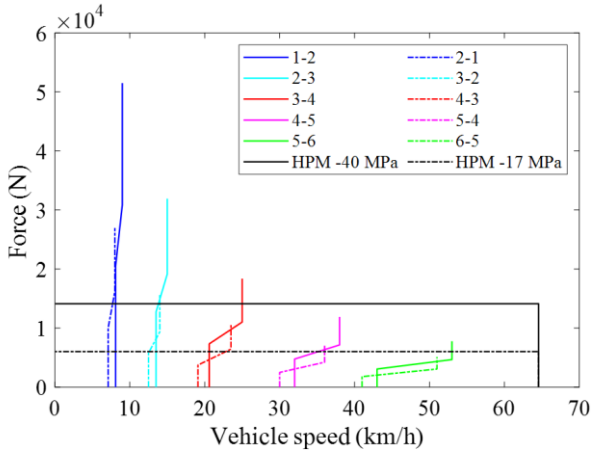

Figure 6.11. Capability analysis based on designed gear shifting schedule.

6.6.2 **Capability analysis based on typical driving cycles**

Above analysis demonstrates that HPM can't maintain vehicle dynamic performance when gear shifting happens at high throttle or high vehicle speed condition. However, in real driving condition, vehicle normally works at modest throttle and speed. So gear shifting during typical driving cycles is analysed to investigate the HPM torque compensation capability for real working conditions. In addition to the CTUDC driving cycle, the UDDS and NEDC driving cycles are also used to analyse the traction force requirement during gear shifting. Based on the designed gear shifting schedule, gear states during each driving cycle are shown in Figure 6.12. Traction force and vehicle speed of the gear shifting points are summarized in Figure 6.13 and compared with the HPM available traction force. It is shown that in typical driving cycles, all of the gear shifting traction force could be compensated by HPM when HPM works with the maximum working pressure. However, its torque compensation capability is affected by lower HPA charging condition.

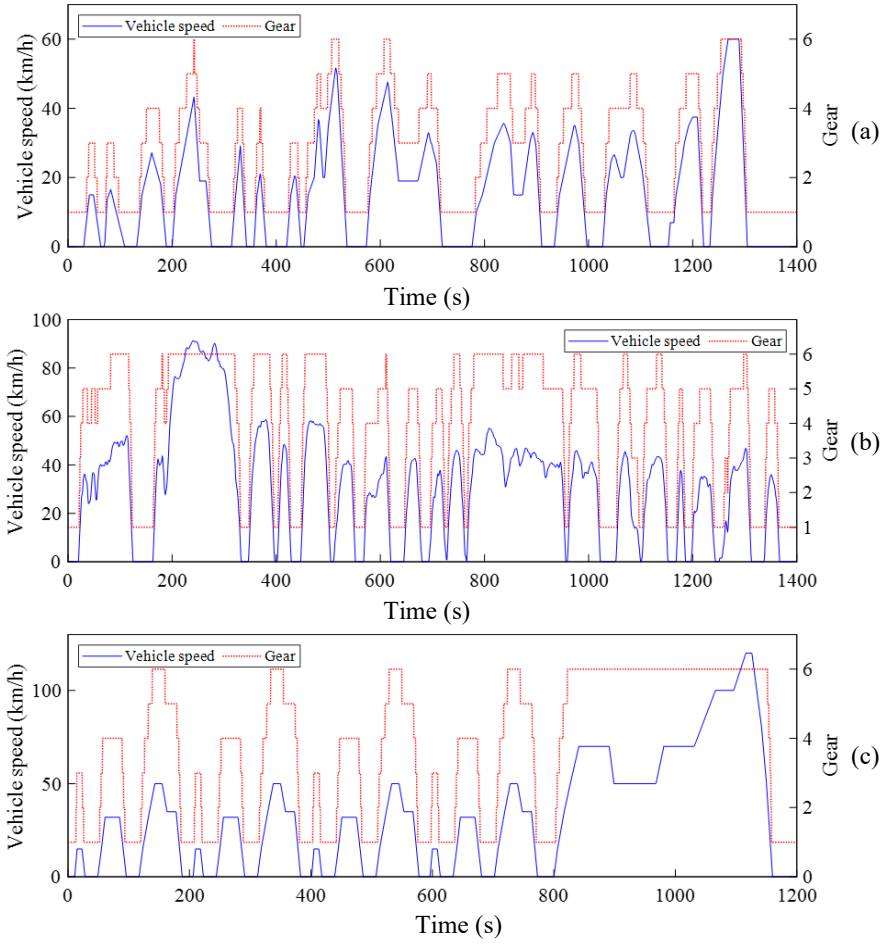

Figure 6.12. Gear state of typical driving cycles, (a) CTUDC, (b) UDDS, (c) NEDC.

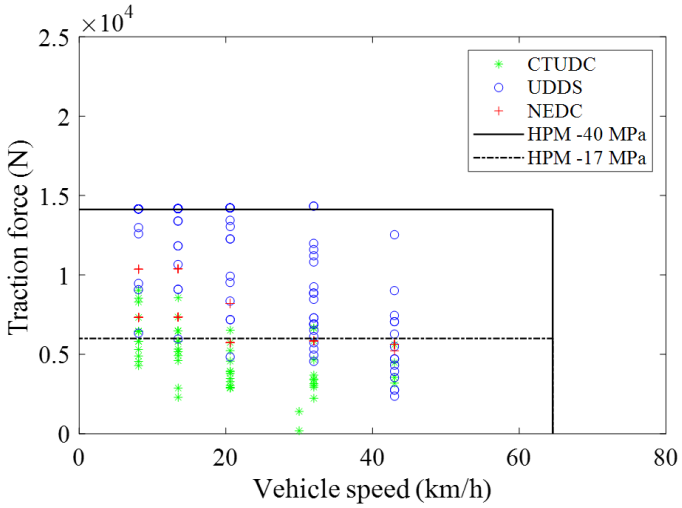

Figure 6.13. Capability analysis based on typical driving cycles.

6.7 **Summary**

In this chapter, PHHV power on gear shifting is researched. During power on gear shifting, LQR controller is used to control engine clutch engagement process which could cause excessive powertrain vibration and deteriorate vehicle driving comfort. Simulation results show that power on gear shifting is successfully conducted based on the designed control strategy. It is demonstrated that vehicle dynamic performance is maintained during gear shifting while the original vehicle experiences torque interruption. EKF is used to estimate PHHV powertrain states which are required by LQR controller for state feedback control. Power analysis of all potential gear shifting according to the gear shifting schedule demonstrates that HPM could compensate for most of the traction force during gear shifting with maximum working pressure. However, if HPA is not fully charged, only the gear shifting with lower throttle could be satisfied. Investigation of typical driving cycles gear shifting proves the HPM capability of torque compensation in real driving conditions which is also affected by its working pressure.

Chapter 7 Case study of an in-wheel drive electric hydraulic hybrid vehicle

7.1 Introduction

Transportation electrification is an important solution for environmental degradation and non-renewable energy shortage. Various electric powertrains have been proposed in academia and industry. At the moment, most of the electric vehicles on the market such as Tesla, Mercedez-Benz EQC, Nissan Leaf and BMW i3 are equipped with single gear transmission owning to the large speed range and low-speed-high-torque characteristics of electric motors [131]. Some electric vehicles use two motors on front axle and rear axle respectively to further improve vehicle dynamic performance [132]. Multi-gear and multi-motor powertrains are widely researched in academia with the motivation of improving electric vehicle energy economy and dynamic performance. AMT [133, 134], Dual clutch transmission [135], Automatic transmission [136, 137] and continuous variable transmission [138, 139] have been implemented on electric vehicles.

In-wheel drive electric vehicle (IEV) in which electric motors are connected to wheels directly has been considered as one of the most important formats of electric vehicles [140]. IEV eliminates all of the intermediate shafts so transmission power loss is cancelled. Vehicle handling and stability performance are significantly improved by torque vectoring control based on quick torque response and outstanding controllability of electric motor [141, 142]. In addition to the attractive advantages of IEV, there are also some unsolved problems which hinder its implementation. Limited installation space makes it difficult for heat dissipation [143]. Vibration caused by increased unsprung mass reduces vehicle driving comfort, deteriorating suspension and motor bearing working conditions, which accelerates the components failure [144].

Inspired by the research on PHHV, HPM has higher power density than electric motor, which means less unsprung mass will be added if HPM is used for in-wheel drive [22, 145]. So vibration problems caused by increased unsprung mass could be mitigated. Besides, HPM is driven by fluids which naturally constitutes the cooling system. Wheels have to work under complicated environment like in water and off-road, which proposes challenges for high voltage electrical system. In contrast, HPM is more reliable in these

complicated working conditions. These advantages make HPM a potential candidate for in-wheel drive [146].

With the motivation of combining the advantages of electrification, HPM and in-wheel drive, this chapter aims to conduct a concept study of an in-wheel drive electric hydraulic hybrid vehicle (IHV). Energy economy and vertical vibration characteristics of IHV are researched and compared with centralized motor drive electric vehicle (CEV) and IEV.

7.2 **Powertrain configurations and working principles**

Configurations of CEV, IEV and IHV are shown in Figure 7.1. In CEV, two central electric motors (CEM) are installed on front axle and rear axle respectively. Single speed transmission is used to adjust CEM speed and torque to coordinate with vehicle maximum speed and dynamic performance demand.

In IEV, in-wheel electric motor (IEM) is used to drive vehicle. In this research, an IEM produced by Protean electric is used for analysis. The IEM parameters such as speed, torque and power are specifically designed for in-wheel drive so it could be directly installed in wheel without any gears for speed and torque adjustment.

In IHV, in-wheel HPM (IHM) are installed to drive vehicle. HPA is used to store energy and LPA is used as a reservoir. During driving, IHM works as motor and oil flows from HPA to LPA. During regenerative braking, IHM works as pump and oil flows from LPA to HPA. In addition to regenerative braking, HPA could also be charged by the central HPM (CHM). In this charging condition, CEM drives CHM to charge HPA. HPA can also be used to charge battery through CHM and CEM.

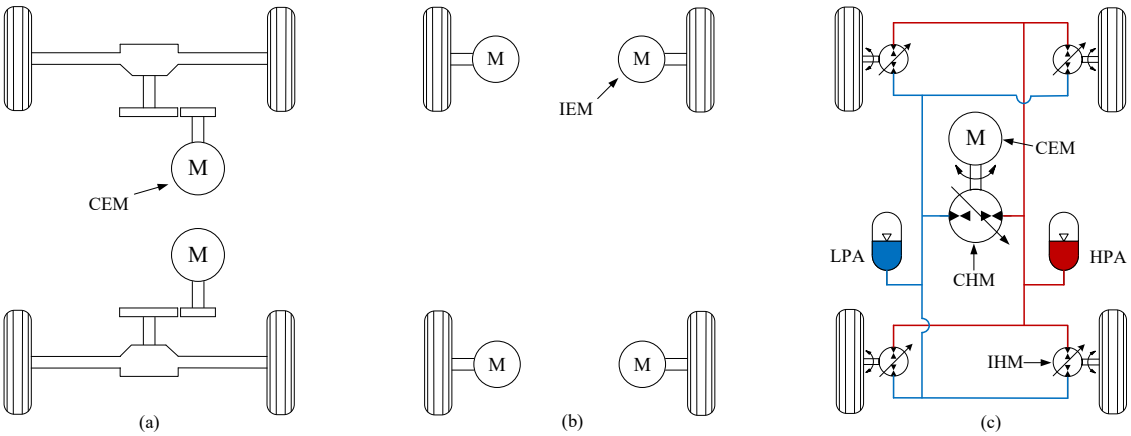

Figure 7.1. Configurations of different vehicles, (a) CEV, (b) IEV, (c) IHV.

7.3 Modelling of vehicle powertrains

7.3.1 Electric motor modelling

The electromagnetic response of power electronics presents higher frequency than that of mechanical powertrain so frequency oscillations from power electronics systems can be overlooked to improve the computation efficiency and simplify the control problems [147]. The maximum electric motor torque is modelled as a lookup table regarding to motor speed. The real-time electric motor torque according to driver command can be expressed as:

$$T_m = \alpha_p T_{m\_\max}(\omega_m) \tag{7.1}$$

where α_p is the accelerator pedal opening and $T_{m\_\max}(\omega_m)$ is the maximum electric motor torque at speed ω_m.

7.3.2 Battery modelling

Battery parameters are affected by many factors like temperature, state of charge (SoC) and charging rate. In this research, battery is modelled as an internal resistance model [148, 149]. Battery parameters are obtained from test which could truly reflect the battery characteristics. Based on the model, battery SoC changing rate is described by following equation:

$$\dot{SoC} = \frac{\sqrt{U_{oc}^2 - 4R_b P_b} - U_{oc}}{2Q_{\max} R_b} \tag{7.2}$$

where U_{oc} is battery open circuit voltage, R_b is battery internal resistance, $Q_{\max}$ is battery maximum capacity and P_b is battery power which is calculated by following equation:

$$P_b = \begin{cases} T_m \omega_m / \eta_m & T_m > 0 \\ T_m \omega_m \eta_m & T_m < 0 \end{cases} \tag{7.3}$$

where η_m is electric motor efficiency which is modelled as a 2-D lookup table regarding to electric motor torque and speed.

Figure 7.2 shows battery U_{oc} and R_b against its SoC. In this model, battery characteristics are calibrated with 25 °C temperature.

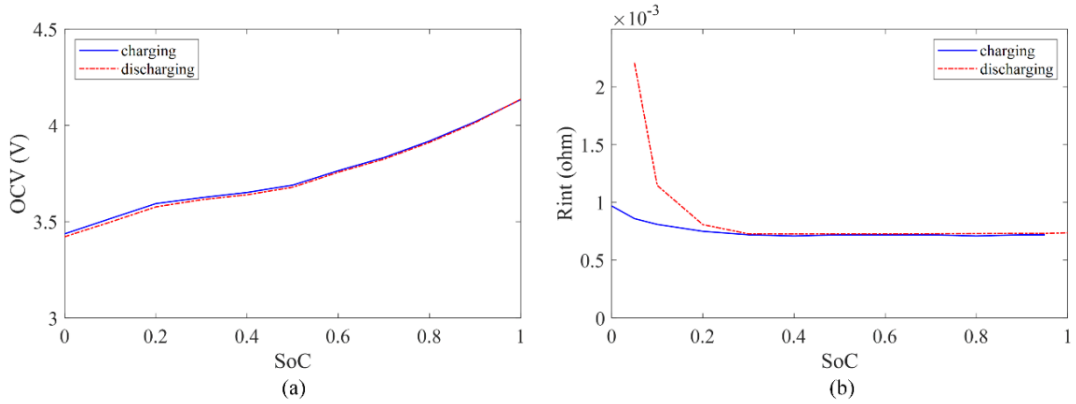

Figure 7.2. Battery characteristics, (a) Open circuit voltage, (b) Internal resistance.

7.4 **Energy management strategy design with DP optimization**

For a new powertrain configuration, it is significant to explore its optimal energy economy, which not only verifies the proposal rationality but also work as a benchmark to evaluate other practical EMS. In this section, DP optimization is adopted to explore the optimal energy economy of each vehicle so that the comparison of energy economy is more convincing. Energy consumption of each vehicle is set as the DP optimization cost function as described in equation (7.4). The target is to find the optimal control input sequence which minimizes the cost function:

$$j = \sum_{n=0}^{N-1} L\left(X(n), U(n)\right) \tag{7.4}$$

In the equation, j is cost function. N is DP optimization steps, X is the state variable, U is the control variable. $L\left(X,U\right)$ is instantaneous energy consumption determined by X and U. In CEV and IEV, the state variable is battery SoC. In IHV, the state variables are battery SoC and HPA pressure. In CEV, the control variables are front CEM torque and rear CEM torque. In IEV, four IEM are adopted so there are potentially four control variables. However, driving torque is normally allocated to left wheels and right wheels evenly to reduce control complexity [150, 151]. Only when there are stability control or steering control requirements, all four IEM are independently controlled to generate yaw moment for vehicle lateral dynamic control.

The state variables at step $n+1$ are determined by the state variables and the control variables at step n, which is described as following:

$$X(n+1) = f\left(X(n), U(n)\right) \tag{7.5}$$

The minimum energy consumption could be obtained by solving the following recursive equations:

For step *N*-1:

$$j(N-1)=\min_{U(N-1)} L\left(X(N-1),U(N-1)\right) \tag{7.6}$$

For step n $(0\le n<N-1)$:

$$j(n)=\min_{U(n)}\left(L\left(X(n),U(n)\right)+j(n+1)\right) \tag{7.7}$$

where $j(N-1)$ is the minimum energy consumption at step *N*-1. $j(N)$ is the minimum total energy consumption from step *n* to step *N*-1.

There are also boundary conditions for the state variables and the control variables.

In CEV, the control variables are front CEM torque T_{f_CEM} and rear CEM torque T_{r_CEM} :

$$U=\left[T_{f\_CEM},\ T_{r\_CEM}\right] \tag{7.8}$$

CEM torque is restricted between the minimum and maximum torque:

$$\begin{aligned} T_{f\_CEM\_\min}\le T_{f\_CEM}\le T_{f\_CEM\_\max}\\ T_{r\_CEM\_\min}\le T_{r\_CEM}\le T_{r\_CEM\_\max}\end{aligned} \tag{7.9}$$

In IEV, there are four IEM. However, driving torque is only allocated between front wheels and rear wheels. Left wheels and right wheels are allocated with the same torque. So the control variables are front IEM torque T_{f_IEM} and rear IEM torque T_{r_IEM} :

$$U=\left[T_{f\_IEM},\ T_{r\_IEM}\right] \tag{7.10}$$

IEM torque is restricted between the minimum and maximum torque:

$$\begin{aligned} T_{f\_IEM\_\min}\le T_{f\_IEM}\le T_{f\_IEM\_\max}\\ T_{r\_IEM\_\min}\le T_{r\_IEM}\le T_{r\_IEM\_\max}\end{aligned} \tag{7.11}$$

Similar to IEV, driving torque is evenly allocated between left wheels and right wheels in IHV. Besides, CEM and CHM are used to transfer energy between battery and HPA. CEM and CHM are decoupled from wheels so their speed and torque could be optimized to achieve the best energy economy. The control variables in IHV are selected as front IHM torque T_{f_IHM} , rear IHM torque T_{r_IHM} , CHM torque T_{CHM} and speed n_{CHM} :

$$U=\left[T_{f\_IHM},\ T_{r\_IHM},\ T_{CHM},\ n_{CHM}\right] \tag{7.12}$$

In IHV, IHM and CHM swashplate angle could only be adjusted between the minimum and maximum values, so they have limited output torque. CHM speed and CEM speed are restricted by their speed limits. HPA pressure P_h should also be maintained between its maximum and minimum values. The boundary conditions in IHV are:

$$\begin{aligned}
&T_{f_IHM_\min} \le T_{f_IHM} \le T_{f_IHM_\max} \\
&T_{r_IHM_\min} \le T_{r_IHM} \le T_{r_IHM_\max} \\
&T_{CHM_\min} \le T_{CHM} \le T_{CHM_\max} \\
&T_{CEM_\min} \le T_{CEM} \le T_{CEM_\max} \\
&n_{CHM_\min} \le n_{CHM} \le n_{CHM_\max} \\
&n_{CEM_\min} \le n_{CEM} \le n_{CEM_\max} \\
&P_{h_\min} \le P_h \le P_{h_\max}
\end{aligned} \tag{7.13}$$

7.5 **Energy consumption simulation and analysis**

Vehicle simulation models are built with Matlab/Simulink to investigate their energy consumption. In this research, a production SUV with CEV configuration is selected as the benchmark vehicle. Its parameters are shown in Table 7.1.

Table 7.1. Parameters of CEV.

Vehicle parameter	Value	CEM parameter	Value
Tyre dynamic radius	0.382 m	Maximum power	175 kW
Rolling resistance coefficient	0.018	Maximum torque	800 Nm
Air drag coefficient	0.36	Maximum speed	4200 rpm
Frontal area	2.45 m^2	Continuous power	119 kW
Mass	2200 kg	Continuous torque	455 Nm
Gear ratio	3	Mass	140 kg

Energy consumption research is based on the world harmonized light-duty vehicles test procedure class 3 (WLTP-3). The WLTP-3 profile is shown in Figure 7.3. It combines urban and high speed driving conditions, which is widely used to investigate the energy consumption of hybrid vehicles and electric vehicles.

7.5.1 **Energy consumption of CEV**

Front CEM and rear CEM working points are shown in Figure 7.4. It could be found at most of the time, only rear CEM is used to drive vehicle. This indicates the CEV driving

system is much oversized for normal driving conditions. Vehicle power demand and torque demand during WLTP-3 are shown in Figure 7.5. It is demonstrated that the power demand is much less than the equipped motor power. However, large motor improves vehicle dynamic performance.

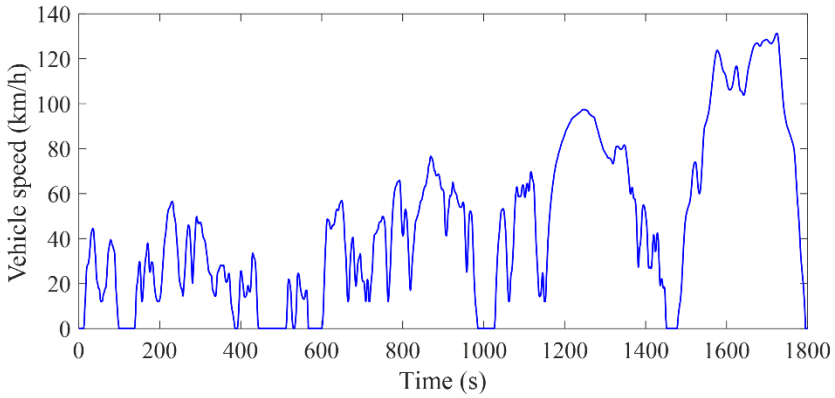

Figure 7.3. WLTP-3 driving cycle.

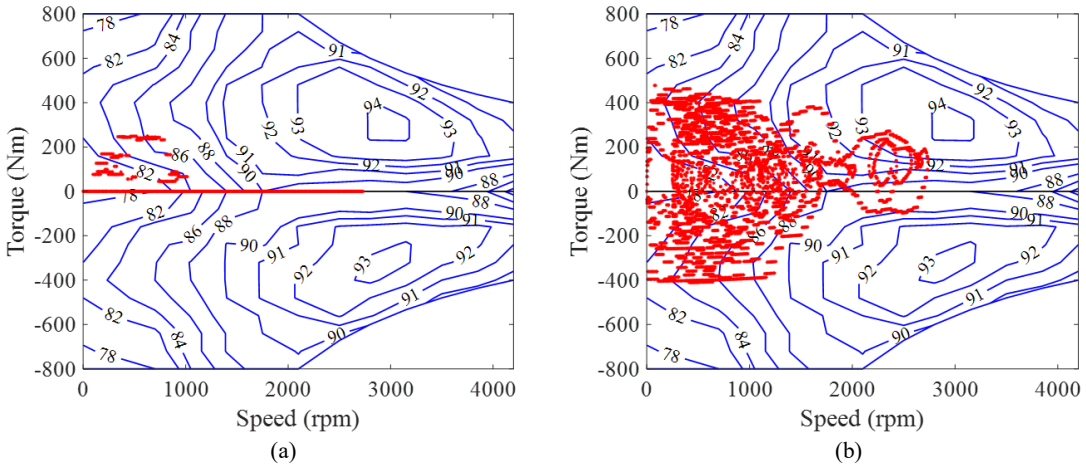

Figure 7.4. CEM working points during WLTP-3, (a) Front CEM, (b) Rear CEM.

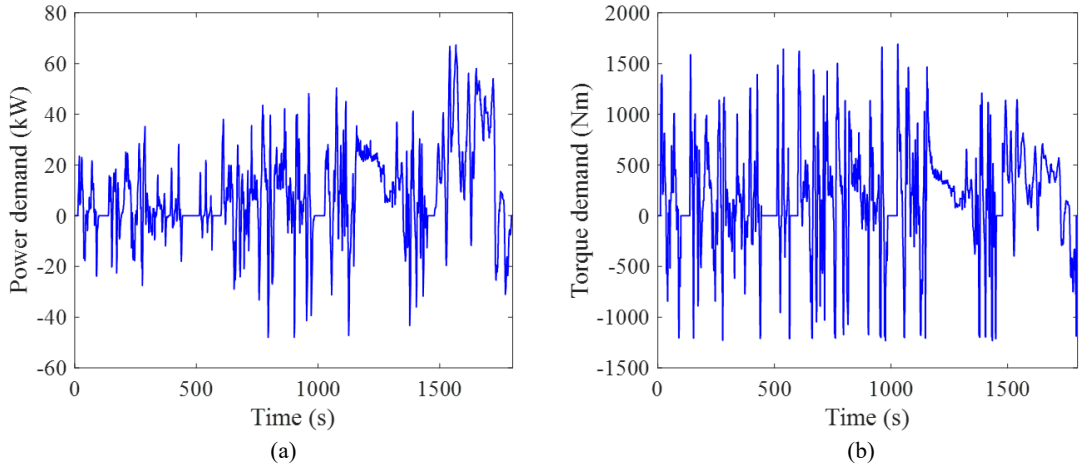

Figure 7.5. CEV power demand during WLTP-3.

7.5.2 **Energy consumption of IEV**

There is no IEV on the market at the moment. However, the PD18 IEM designed by Protean electric has been produced and promoted to the market. This IEM targets on in-wheel drive passenger vehicle. So it is selected to drive the benchmark vehicle to investigate the IEV energy consumption. The IEM parameters are shown in Table 7.2 and its efficiency map is shown in Figure 7.6. The IEM is designed for in-wheel drive so it is installed in wheel directly without any gears.

Table 7.2. Parameters of IEM.

Parameter	Value	Parameter	Value
Maximum torque	1250 Nm	Continuous torque	650 Nm
Maximum power	80 kW	Continuous power	60 kW
Maximum speed	1600 rpm	Mass	36 kg

By simulation, IEM working points during WLTP-3 are shown in Figure 7.6. It is shown that rear IEM covers most of the driving torque which means powertrain is also oversized in IEV.

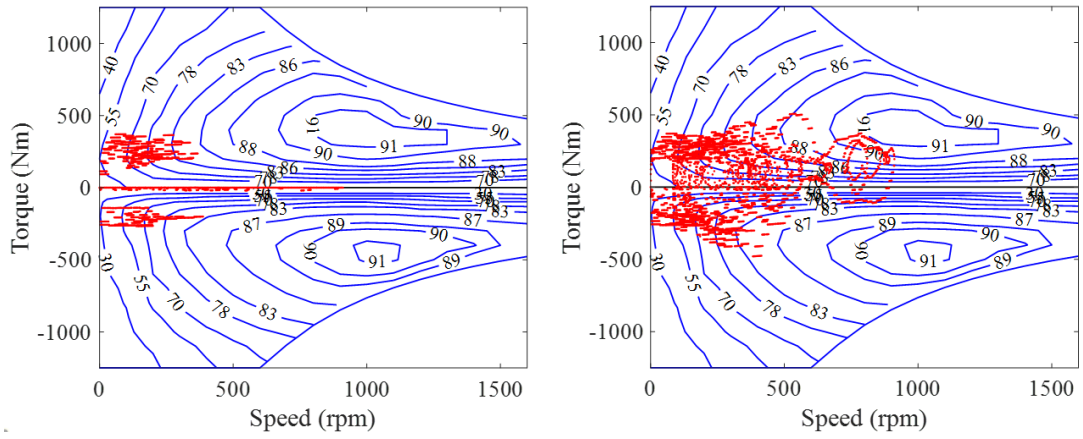

Figure 7.6. IEM working points during WLTP-3, (a) Front IEM, (b) Rear IEM.

7.5.3 **Energy consumption of IHV**

IHV is a novel vehicle configuration proposed in this research. So its powertrain parameters are designed here. To make IHV have similar vehicle dynamic performance with CEV and IEV, IHM power is selected same as IEM. In IHV, a gear is adopted to adjust IHM speed and torque. CHM and CEM are disconnected with wheels, so they just need to satisfy vehicle power demand but not torque demand. From Figure 7.5, the vehicle

power demand is moderate while the torque demand is remarkable. So only one CEM is reserved in IHV powertrain. CHM is selected as the same power as CEM. Parameters of IHV are listed in Table 7.3.

Table 7.3. Parameters of IHV.

Parameter	Value	Parameter	Value
IHM		CHM	
Maximum speed	8750 rpm	Maximum speed	6150 rpm
Maximum displacement	28 cm^3	Maximum displacement	80 cm^3
Maximum working pressure	40 MPa	Maximum working pressure	40 MPa
Maximum torque	160 Nm	Maximum torque	455 Nm
Maximum power	96 kW	Maximum power	185 kW
Mass	16 kg	Mass	36kg
IHM gear ratio	5.47		
HPA		LPA	
Maximum working pressure	40 MPa	Maximum working pressure	33 MPa
Mass	71 kg	Mass	33 kg
Nominal volume	20 L	Nominal volume	10 L

IHM working points during WLTP-3 is shown in Figure 7.7. It is shown that IHV also tries to use only rear IHM for driving. It could also be found that the distribution of rear IHM working points is different from rear IEM. This is determined by different efficiency maps of IHM and IEM.

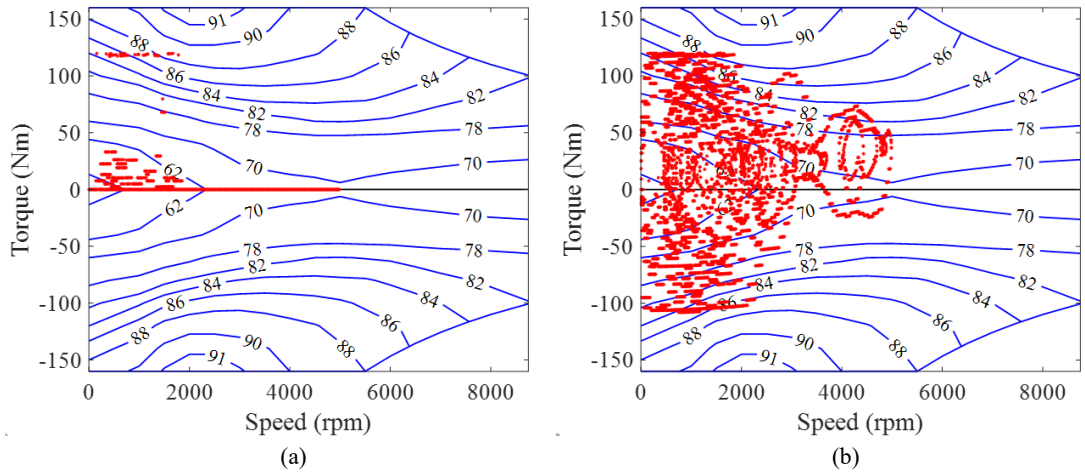

Figure 7.7. IHM working points during WLTP-3, (a) Front IHM, (b) Rear IHM.

HPA pressure and gas volume are shown in Figure 7.8. It is shown that HPA pressure is always lower than its maximum working pressure which means HPA capacity is sufficient for regenerative braking. When HPA is used for regenerative braking, battery charging burden is relieved.

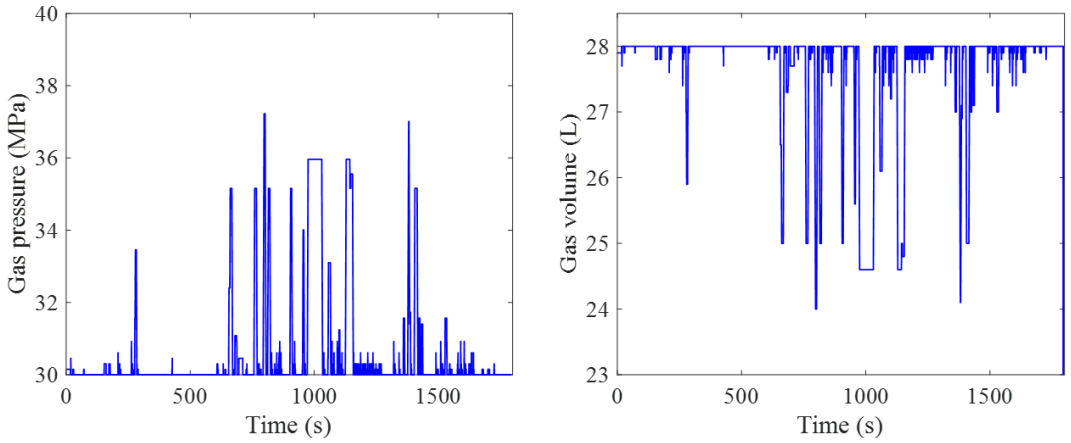

Figure 7.8. HPA pressure and gas volume change during WLTP-3.

Figure 7.9 shows the distribution of CEM and CHM working points during WLTP-3. As mentioned above, in IHV, CEM and CHM are disconnected with wheels. So under a certain power demand, CEM and CHM could work at the most efficient point.

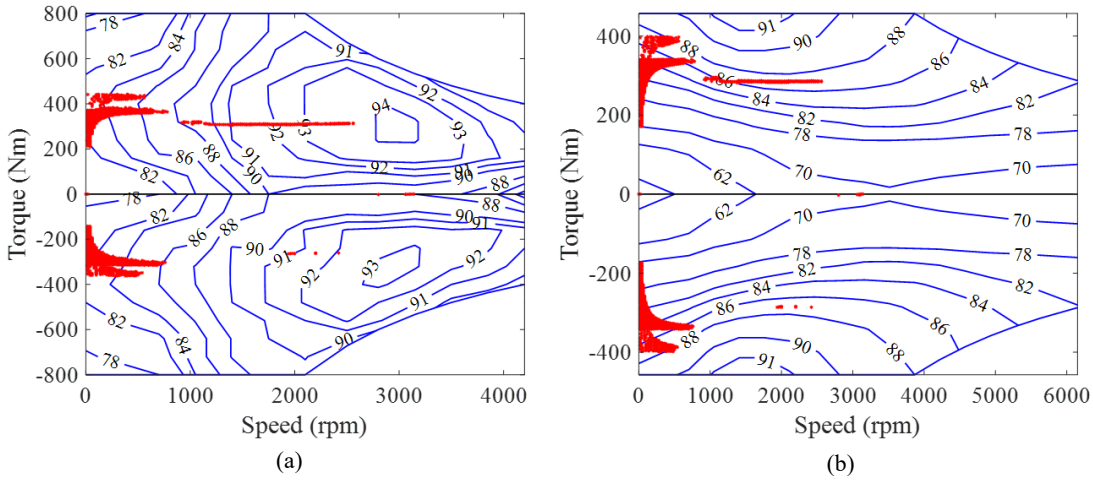

Figure 7.9. CEM and CHM working points during WLTP-3.

7.5.4 **Energy consumption comparison**

Energy consumption and SoC change of each vehicle during WLTP-3 are shown in Figure 7.10. It could be found that IEV consumes slightly more energy than CEV. The main reason is that IEM has lower efficiency than CEM, especially in low speed area. These

results indicate that although powertrain is simplified in IEV which helps reduce power loss, lower IEM efficiency makes IEV not very competitive in energy economy. Energy consumption of IHV is 40% more than CEV and 34% more than IEV, which demonstrates a bad energy economy of IHV. The reason is that hydraulic accumulator has much lower energy density than battery, so when CEM is used to charge HPA, it is equivalent to use CEM to drive vehicle. The total powertrain efficiency is degraded by hydraulic circuit.

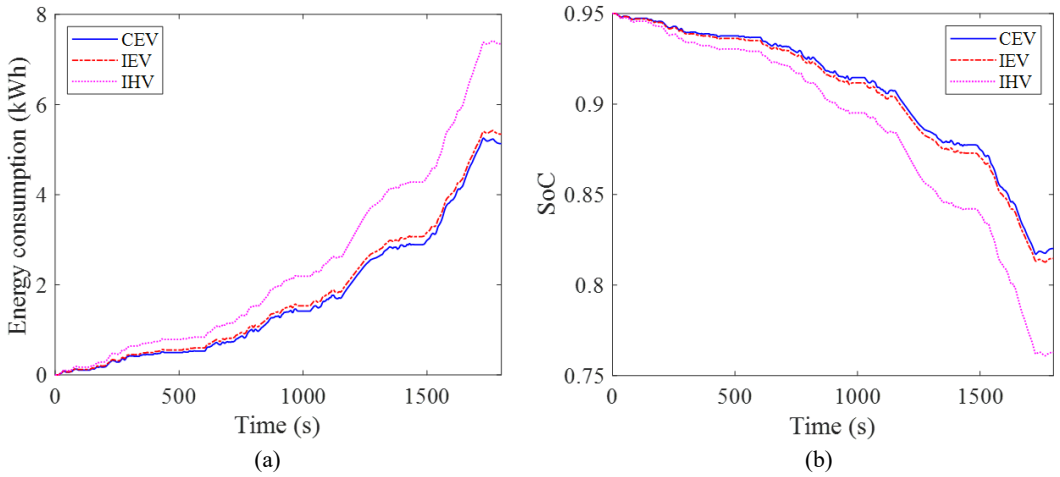

Figure 7.10. Energy consumption and SoC change of each vehicle.

Table 7.4. Energy consumption and SoC change comparison.

Vehicle	Initial SoC	Final SoC	Fuel consumption (kWh)
CEV	0.95	0.82	5.131
IEV	0.95	0.815	5.344
IHV	0.95	0.763	7.346

7.6 **Vertical vibration analysis**

From energy consumption analysis, IHV consumes much more energy than CEV and IEV. However, hydraulic motor has larger power density than electric motor, which could help to mitigate the problems caused by increased unsprung mass. It has been proved that the increased unsprung mass remarkably changes vehicle vertical vibration characteristics and degrades vehicle driving comfort [152]. In this section, vertical vibration characteristics of each vehicle are researched based on a quarter vehicle dynamic model as shown in Figure 7.11. In the model, stiffness and damping are considered as constant parameters [153, 154]. For different vehicles, they have the same quarter vehicle dynamic model but with different parameters.

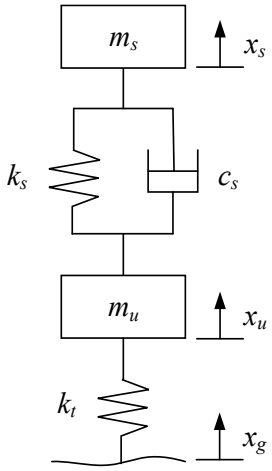

Figure 7.11. Quarter vehicle dynamic model.

The quarter vehicle model is described by equation (7.14):

$$\begin{cases} m_s\ddot{x}_s = -k_s(x_s - x_u) - c_s(\dot{x}_s - \dot{x}_u) \\ m_u\ddot{x}_u = k_s(x_s - x_u) + c_s(\dot{x}_s - \dot{x}_u) - k_t(x_u - x_g) \end{cases} \tag{7.14}$$

where m_s is sprung mass, x_s is sprung mass displacement, k_s is suspension stiffness, c_s is suspension damping, m_u is unsprung mass, x_u is unsprung mass displacement, k_t is tyre stiffness. In this model, tyre damping is ignored due to its small effect on vertical vibration [155]. The quarter vehicle dynamic model parameters of each vehicle are shown in Table 7.5. In IEV, two CEM are removed so its sprung mass is reduced compared with CEV. IEM increases its unsprung mass. In IHV, one CEM is removed but a CHM and two accumulators are installed on-board, so its sprung mass doesn't significantly change. As mentioned, hydraulic motor has higher power density than electric motor, so IHM mass is much smaller than IEM with the same power, which explains IHV unsprung mass is smaller than IEV.

Table 7.5. Quarter vehicle dynamic model parameters of different vehicles.

Parameter	CEV	IEV	IHV
Sprung mass (kg)	510	426.5	506.5
Unsprung mass (kg)	40	74	56
Suspension stiffness (N/m)	32000		
Suspension damping (Ns/m)	2830		
Tyre stiffness (N/m)	200000		

To investigate vehicle vertical vibration characteristics under road excitation, the state space function and output function are built as following:

$$\begin{cases} \dot{\mathbf{X}} = \mathbf{AX}+\mathbf{BU} \\ \mathbf{Y} = \mathbf{CX}+\mathbf{DU} \end{cases} \tag{7.15}$$

In the equation, sprung mass displacement, sprung mass velocity, unsprung mass displacement and unsprung mass velocity are selected as the state variables **X**. Sprung mass acceleration, unsprung mass acceleration, suspension deformation and tyre deformation are selected as the output variables **Y** [156]. Road excitation is selected as the input variable.

$$\mathbf{X} = \left[x_s, \dot{x}_s, x_u, \dot{x}_u\right]^T,\ \mathbf{Y} = \left[\ddot{x}_s, \ddot{x}_u, x_s - x_u, x_u - x_g\right]^T,\ \mathbf{U} = \left[x_g\right] \tag{7.16}$$

From Eq.(7.14), the state space function and output function are obtained as shown in equation (7.17) and equation (7.18):

$$\begin{bmatrix} \dot{x}_s \\ \ddot{x}_s \\ \dot{x}_u \\ \ddot{x}_u \end{bmatrix} = \begin{bmatrix} 0 & 1 & 0 & 0 \\ -\frac{k_s}{m_s} & -\frac{c_s}{m_s} & \frac{k_s}{m_s} & \frac{c_s}{m_s} \\ 0 & 0 & 1 & 0 \\ \frac{k_s}{m_u} & \frac{c_s}{m_u} & -\frac{k_t + k_s}{m_u} & -\frac{c_s}{m_u} \end{bmatrix} \begin{bmatrix} x_s \\ \dot{x}_s \\ x_u \\ \dot{x}_u \end{bmatrix} + \begin{bmatrix} 0 \\ 0 \\ 0 \\ \frac{k_t}{m_u} \end{bmatrix} \left[x_g\right] \tag{7.17}$$

$$\begin{bmatrix} \ddot{x}_s \\ \ddot{x}_u \\ x_s - x_u \\ x_u - x_g \end{bmatrix} = \begin{bmatrix} -\frac{k_s}{m_s} & -\frac{c_s}{m_s} & \frac{k_s}{m_s} & \frac{c_s}{m_s} \\ \frac{k_s}{m_u} & \frac{c_s}{m_u} & -\frac{k_t + k_s}{m_u} & -\frac{c_s}{m_u} \\ 1 & 0 & -1 & 0 \\ 0 & 0 & 1 & 0 \end{bmatrix} \begin{bmatrix} x_s \\ \dot{x}_s \\ x_u \\ \dot{x}_u \end{bmatrix} + \begin{bmatrix} 0 \\ \frac{k_t}{m_u} \\ 0 \\ -1 \end{bmatrix} \left[x_g\right] \tag{7.18}$$

Frequency response analysis under road excitation is conducted and results are shown in Figure 7.12. There are two natural frequencies in quarter vehicle dynamic model. In IEV, the natural frequencies and amplitudes are all greatly changed compared with the benchmark CEV. In IHV, the 1st natural frequency is very close to CEV but the 2nd natural frequency is decreased.

Figure 7.12(a) shows the sprung mass acceleration response to road excitation. It is shown that sprung mass acceleration is significantly increased in IEV with both natural frequencies, which indicates a worse driving comfort. The IHV sprung mass acceleration response is almost the same as CEV at the 1st natural frequency. At the 2nd natural frequency, the IHV sprung mass acceleration response is only slightly higher than CEV.

So from the vertical acceleration perspective, IHV maintains vehicle driving comfort while IEV degrades vehicle driving comfort.

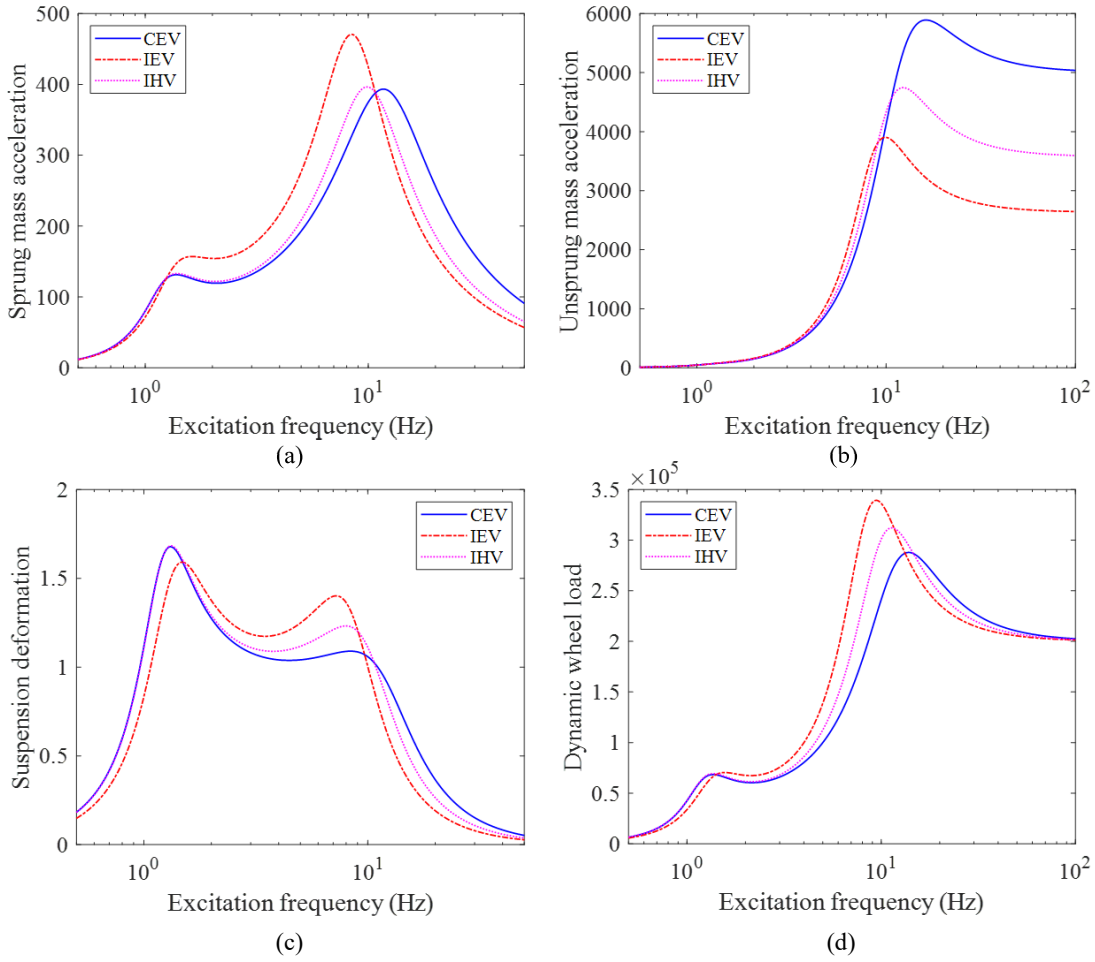

Figure 7.12. Frequency response analysis to road excitation.

Figure 7.12(b) shows that the unsprung mass acceleration response of all vehicles are quite small at the 1st natural frequency. At the 2nd natural frequency, the unsprung mass acceleration response of IEV and IHV are reduced due to larger unsprung mass.

The suspension deformation with different excitation frequency is shown in Figure 7.12(c). IEV has reduced suspension deformation at the 1st natural frequency but increased suspension deformation at the 2nd natural frequency. The IHV suspension deformation is also larger than CEV at the 2nd natural frequency. It should also be noticed although the suspension deformation of IEV and IHV are increased at the 2nd natural frequency, they are still smaller than the CEV suspension deformation at the 1st natural frequency.

The tyre deformation which represents dynamic wheel load is shown in Figure 7.12(d). It is demonstrated that at the 1st natural frequency, the larger unsprung mass in IEV and

IHV don't increase wheel load remarkably. However, wheel load is increased a lot at the 2nd natural frequency in IEV and IHV, which proposes higher requirements for tyre strength. IHV dynamic wheel load is smaller than IEV dynamic wheel load.

7.7 **Summary**

This chapter proposes a novel IHV structure which inherits the advantages of independent wheel torque control and reduces the drawbacks caused by increased unsprung mass in IEV. Through DP optimization, IHV consumes 40% more energy than CEV and 34% more energy than IEV respectively, which makes IHV incompetent for energy saving. However, hydraulic motor has higher power density than electric motor, so less unsprung mass is added in IHV than IEV. Vibration analysis results demonstrate that the vibration problems caused by increased unsprung mass could be alleviated in IHV, especially the vehicle body acceleration which directly affects driving comfort. Besides, heat dissipation and IEM high voltage safety challenge are reduced in IHV. Based on above analysis, IHV is more suitable to work in off-road conditions such as for mining, forestry and agriculture. For these applications, in-wheel drive structure improves vehicle handling and stability performance by independent wheel torque control. Hydraulic motors also have better reliability under bad working conditions. IHV is not recommended for on-road use such as passenger vehicle or commercial vehicle due to its bad energy economy performance.

Chapter 8 Conclusion

PHHV helps to reduce fuel consumption in transportation for medium and heavy duty vehicles. In this research, PHHV hydraulic driving system parameters are designed through vehicle power analysis firstly. During parameter design, all of the HPM working pressure, displacement and speed which affect HPM efficiency are considered. Hydraulic driving system working condition such as minimum working pressure is designed with compromise of vehicle dynamic performance, fuel economy, cost and installation space. Based on the designed hydraulic driving system parameters, the optimal PHHV fuel economy is obtained by DP optimization. Through simulation, PHHV achieves fuel consumption reduction by 27.5% during the typical urban driving cycle CTUDC compared with the original engine driving vehicle, which proves the fuel economy of PHHV. Based on DP optimization results, a practical rule-based EMS is designed to investigate PHHV fuel economy in real application. PHHV consumes only 1.53% more fuel with rule-based EMS compared with DP optimization, indicting the effectiveness and practicality of rule-based EMS. The regenerative braking results show that most of the braking energy could be recovered because the braking intensity is normally small in urban driving conditions with which braking could be realized by HPM only. Parameter sensitivity analysis with different vehicle mass demonstrates PHHV achieves good energy saving benefit with all load conditions.

The vibration characteristics of PHHV powertrain is researched and compared with the original vehicle powertrain for the first time. A 14 degrees of freedom dynamic model is established to obtain the natural frequencies and mode shapes of PHHV powertrain. Based on the natural frequencies and mode shapes, the 14 degrees of freedom dynamic model is simplified and the frequency response of PHHV powertrain to engine excitation and HPM excitation are researched. Results show that with a HPM added on the driveshaft, the powertrain dynamic response to engine excitation is increased only at the 1^{st} natural frequency. However, due to the minimum engine excitation frequency being higher than the 1^{st} natural frequency, powertrain resonance is avoided. HPM also introduces excitation to PHHV powertrain due to its instantaneous torque fluctuations. As HPM excitation is much smaller than engine excitation, it does not produce excessive powertrain vibration. Additionally, HPM is not exposed to significant forced vibration

caused by engine excitation. Consequently, the need for substantive vibration isolation for HPM is reduced.

Based on the simplified PHHV powertrain dynamic model, mode switching from HPM driving mode to engine driving mode is analysed and control strategy is designed. Constant vehicle acceleration is selected as the indicator of stable driving torque. Simulation results demonstrate that by using HPM to compensate engine clutch torque, vehicle dynamic performance is guaranteed during mode switching. From the comparison between different LQR weighting matrices, multiple options are available to drivers on vehicle dynamic performance and driving comfort during mode switching.

Power on gear shifting control strategy is designed for PHHV. Torque interruption is eliminated by using HPM to compensate the driving torque during gear shifting so that vehicle dynamic performance is maintained and powertrain vibration is reduced. EKF is adopted for PHHV powertrain state estimation to provide more accurate state feedback for gear shifting control and mode switching control. HPM torque compensation capability during gear shifting is researched based on the designed gear shifting schedule and typical driving cycles. Results show that HPM could satisfy most of the torque compensation requirements for the gear shifting during typical urban driving cycles with the designed gear shifting schedule.

From above analysis, PHHV has significant effect on reducing vehicle fuel consumption. The attachment of hydraulic driving system doesn’t bring extra challenges to powertrain vibration control. Besides, vehicle dynamic performance could be improved by power on gear shifting with the help of HPM.

Inspired by the high power density of HPM, the potential of using HPM for in-wheel drive is investigated as a case study. Energy economy analysis shows that IHV uses more energy than CEV and IEV due to more powertrain components. Vibration analysis demonstrates that with less added unsprung mass, IHV makes less change to vehicle vertical vibration characteristics than IEV. These results indicate that IHV is suitable for off-road implementations where handling and stability performance are important but energy consumption could be compromised, such as for mining, forestry and agriculture.

Bibliography

[1] E. Honey and I.-S. Suh, "A feasibility study of an electric–hydraulic hybrid powertrain for passenger vehicles," *Proceedings of the Institution of Mechanical Engineers, Part D: Journal of Automobile Engineering,* vol. 229, no. 14, pp. 1894-1906, 2015.

[2] B. Zhu *et al.*, "Gear shift schedule design for multi-speed pure electric vehicles," *Proceedings of the Institution of Mechanical Engineers, Part D: Journal of Automobile Engineering,* vol. 229, no. 1, pp. 70-82, 2014.

[3] F. Zhang, H. Liu, Y. Hu, and J. Xi, "A Supervisory Control Algorithm of Hybrid Electric Vehicle Based on Adaptive Equivalent Consumption Minimization Strategy with Fuzzy PI," *Energies,* vol. 9, no. 11, p. 919, 2016.

[4] E. Galvagno, M. Velardocchia, and A. Vigliani, "A model for a flywheel automatic assisted manual transmission," *Mechanism and Machine Theory,* vol. 44, no. 6, pp. 1294-1305, 2009.

[5] K. Baer, L. Ericson, and P. Krus, "Robustness and performance evaluations for simulation-based control and component parameter optimization for a series hydraulic hybrid vehicle," *Engineering Optimization,* vol. 52, no. 3, pp. 446-464, 2019.

[6] M. Zeng, B. Tan, F. Ding, B. Zhang, H. Zhou, and Y. Chen, "An experimental investigation of resonance sources and vibration transmission for a pure electric bus," *Proceedings of the Institution of Mechanical Engineers, Part D: Journal of Automobile Engineering,* vol. 234, no. 4, pp. 950-962, 2020.

[7] W. Yang, J. Ruan, J. Yang, and N. Zhang, "Investigation of integrated uninterrupted dual input transmission and hybrid energy storage system for electric vehicles," *Applied Energy,* vol. 262, 2020.

[8] J. Nzisabira, Y. Louvigny, and P. Duysinx, "Comparison of ultra capacitors, hydraulic accumulators and batteries technologies to optimize hybrid vehicle ecoefficiency," in *Proceeding of 2nd IEEE Int. Conference of Power Engineering, Energy, and Electric Drives*, 2009: IEEE.

[9] S. Hui, Y. Lifu, and J. Junqing, "Hydraulic/electric synergy system (HESS) design for heavy hybrid vehicles," *Energy,* vol. 35, no. 12, pp. 5328-5335, 2010.

[10] J. Leon, J. M. Garcia, M. J. Acero, A. Gonzalez, G. Niu, and M. Krishnamurthy, "Case Study of an Electric-Hydraulic Hybrid Propulsion System for a Heavy Duty Electric Vehicle," vol. 1, 2016.

[11] H. Kwon and M. Ivantysynova, "System Characteristics Analysis for Energy Management of Power-Split Hydraulic Hybrids," *Energies,* vol. 13, no. 7, 2020.

[12] O. Topal and İ. Nakir, "Total Cost of Ownership Based Economic Analysis of Diesel, CNG and Electric Bus Concepts for the Public Transport in Istanbul City," *Energies,* vol. 11, no. 9, 2018.

[13] J. Li, X. Jin, and R. Xiong, "Multi-objective optimization study of energy management strategy and economic analysis for a range-extended electric bus," *Applied Energy,* vol. 194, pp. 798-807, 2017.

[14] T.-V. Vu, C.-K. Chen, and C.-W. Hung, "A Model Predictive Control Approach for Fuel Economy Improvement of a Series Hydraulic Hybrid Vehicle," *Energies,* vol. 7, no. 11, pp. 7017-7040, 2014.

[15] G. Niu, F. Shang, M. Krishnamurthy, and J. M. Garcia, "Design and Analysis of an Electric Hydraulic Hybrid Powertrain in Electric Vehicles," *IEEE Transactions on Transportation Electrification,* vol. 3, no. 1, pp. 48-57, 2017.

[16] Z. Du, K. L. Cheong, and P. Y. Li, "Energy management strategy for a power-split hydraulic hybrid vehicle based on Lagrange multiplier and its modifications," *Proceedings of the Institution of Mechanical Engineers, Part I: Journal of Systems and Control Engineering,* vol. 233, no. 5, pp. 511-523, 2018.

[17] T. H. Ho and K. K. Ahn, "Modeling and simulation of hydrostatic transmission system with energy regeneration using hydraulic accumulator," *Journal of Mechanical Science and Technology,* vol. 24, no. 5, pp. 1163-1175, 2010.

[18] K.-E. Rydberg, "Energy efficient hydraulic hybrid drives," in *11: th Scandinavian International Conference on Fluid Power, SICFP'09, June 2-4, Linköping, Sweden*, 2009.

[19] R. Kumar and M. Ivantysynova, "An Instantaneous Optimization Based Power Management Strategy to Reduce Fuel Consumption in Hydraulic Hybrids," *International Journal of Fluid Power,* vol. 12, no. 2, pp. 15-25, 2011.

[20] C. Patil *et al.*, "Model-Based Approach to Estimate Fuel Savings from Series Hydraulic Hybrid Vehicle: Model Development and Validation," vol. 1, 2011.

[21] J. Kargul, A. Moskalik, K. Newman, D. Barba, and J. Rockwell, "Design and Demonstration of EPA's Integrated Drive Module for Commercial Series Hydraulic Hybrid Trucks and Buses," *SAE International Journal of Commercial Vehicles,* vol. 8, no. 2, pp. 549-567, 2015.

[22] H. Zhou, Z. Xu, L. Liu, D. Liu, and L. Zhang, "A Rule-Based Energy Management Strategy Based on Dynamic Programming for Hydraulic Hybrid Vehicles," *Mathematical Problems in Engineering,* vol. 2018, pp. 1-10, 2018.

[23] J. T. Wagner and T. Bradley, "Analysis and Optimization of a Parallel Hydraulic Hybrid," SAE Technical Paper0148-7191, 2014.

[24] Y. Yan, G. Liu, and J. Chen, "Integrated modeling and optimization of a parallel hydraulic hybrid bus," *International Journal of Automotive Technology,* vol. 11, no. 1, pp. 97-104, 2010.

[25] F. Liu, W. Wu, J. Hu, and S. Yuan, "Design of multi-range hydro-mechanical transmission using modular method," *Mechanical Systems and Signal Processing,* vol. 126, pp. 1-20, 2019.

[26] C. Ji, Y. Zhu, C. Liang, and X. Liu, "Simulation study on the operating characteristics of a hybrid hydraulic passenger car with a power split transmission," *Vehicle System Dynamics,* vol. 51, no. 10, pp. 1518-1532, 2013.

[27] F. Tavares, R. Johri, and Z. Filipi, "Simulation Study of Advanced Variable Displacement Engine Coupled to Power-Split Hydraulic Hybrid Powertrain," *Journal of Engineering for Gas Turbines and Power,* vol. 133, no. 12, 2011.

[28] S. Hui, J. Ji-hai, and W. Xin, "Torque control strategy for a parallel hydraulic hybrid vehicle," *Journal of Terramechanics,* vol. 46, no. 6, pp. 259-265, 2009.

[29] K. U. S. T. Yaser, R. Bakatwar, A. Bhargava, and S. Tiwari, "Development, Performance Analysis and Optimization of Parallel Hydraulic Hybrid System for City Bus Application," presented at the SAE Technical Paper Series, 2018.

[30] Y.-c. Yan, G.-q. Liu, and J. Chen, "Parameter design strategies of a parallel hydraulic hybrid bus," in *Vehicle Power and Propulsion Conference, 2008. VPPC'08. IEEE*, 2008, pp. 1-6: IEEE.

[31] R. Ramakrishnan, S. S. Hiremath, and M. Singaperumal, "Theoretical investigations on the effect of system parameters in series hydraulic hybrid system with hydrostatic regenerative braking," *Journal of Mechanical Science and Technology,* vol. 26, no. 5, pp. 1321-1331, 2012.

[32] G. Niu, F. Shang, M. Krishnamurthy, and J. M. Garcia, "Evaluation and selection of accumulator size in electric-hydraulic hybrid (EH2) powertrain," in *Transportation Electrification Conference and Expo (ITEC), 2016 IEEE*, 2016, pp. 1-6: IEEE.

[33] J. T. Wagner and T. Bradley, "Analysis and Optimization of a Parallel Hydraulic Hybrid," vol. 1, 2014.

[34] B. Wu, C.-C. Lin, Z. Filipi, H. Peng, and D. Assanis, "Optimal power management for a hydraulic hybrid delivery truck," *Vehicle System Dynamics,* vol. 42, no. 1-2, pp. 23-40, 2004.

[35] A. Taghavipour, M. S. Foumani, and M. Boroushaki, "Implementation of an optimal control strategy for a hydraulic hybrid vehicle using CMAC and RBF networks," *Scientia Iranica,* vol. 19, no. 2, pp. 327-334, 2012.

[36] T. O. Deppen, A. G. Alleyne, K. Stelson, and J. Meyer, "A model predictive control approach for a parallel hydraulic hybrid powertrain," in *Proceedings of the 2011 American Control Conference*, 2011, pp. 2713-2718: IEEE.

[37] Y. Yang, X. He, Y. Zhang, and D. Qin, "Regenerative Braking Compensatory Control Strategy Considering CVT Power Loss for Hybrid Electric Vehicles," *Energies,* vol. 11, no. 3, 2018.

[38] C. Qiu, G. Wang, M. Meng, and Y. Shen, "A novel control strategy of regenerative braking system for electric vehicles under safety critical driving situations," *Energy,* vol. 149, pp. 329-340, 2018.

[39] Z. Zhang, J. Chen, and B. Wu, "The control strategy of optimal brake energy recovery for a parallel hydraulic hybrid vehicle," *Proceedings of the Institution of Mechanical Engineers, Part D: Journal of Automobile Engineering,* vol. 226, no. 11, pp. 1445-1453, 2012.

[40] X. Ning *et al.*, "Optimization of Energy Recovery Efficiency for Parallel Hydraulic Hybrid Power Systems Based on Dynamic Programming," *Mathematical Problems in Engineering,* vol. 2019, pp. 1-11, 2019.

[41] T. Liu, J. Zheng, Y. Su, and J. Zhao, "A Study on Control Strategy of Regenerative Braking in the Hydraulic Hybrid Vehicle Based on ECE Regulations," *Mathematical Problems in Engineering,* vol. 2013, pp. 1-9, 2013.

[42] T. Liu, J. Jiang, and H. Sun, "Investigation to Simulation of Regenerative Braking for Parallel Hydraulic Hybrid Vehicles," in *2009 International Conference on Measuring Technology and Mechatronics Automation*, 2009, vol. 2, pp. 242-245.

[43] B. Zheng, X. Wang, W. Liang, and X. Liu, "Simulation and experiment of front located parallel hydraulic hybrid system," in *2015 International Conference on Fluid Power and Mechatronics (FPM)*, 2015, pp. 1383-1387: IEEE.

[44] F. A. Bender, T. Bosse, and O. Sawodny, "An investigation on the fuel savings potential of hybrid hydraulic refuse collection vehicles," *Waste Manag,* vol. 34, no. 9, pp. 1577-83, Sep 2014.

[45] T. Nguyen, M. Elahinia, and S. Wang, "Hydraulic hybrid vehicle vibration isolation control with magnetorheological fl uid mounts," *International Journal of Vehicle Design,* vol. 63, no. 2-3, pp. 199-222, 2013.

[46] M. H. Elahinia, "Vibration isolation for parallel hydraulic hybrid vehicles," *Shock and Vibration,* vol. 15, no. 2, pp. 193-204, 2008.

[47] A. Mohaghegh-Motlagh and M. H. Elahinia, "Dynamic force profile in hydraulic hybrid vehicles: a numerical investigation," *Vehicle System Dynamics,* vol. 48, no. 4, pp. 405-428, 2010.

[48] J. Huang, Z. Yan, L. Quan, Y. Lan, and Y. Gao, "Characteristics of delivery pressure in the axial piston pump with combination of variable displacement and variable speed," *Proceedings of the Institution of Mechanical Engineers, Part I: Journal of Systems and Control Engineering,* vol. 229, no. 7, pp. 599-613, 2015.

[49] S. Mamèic and M. Bogdevièius, "Simulation of dynamic processes in hydraulic accumulators," *Transport,* vol. 25, no. 2, pp. 215-221, 2010.

[50] Y.-l. Chen, S.-a. Liu, J.-h. Jiang, T. Shang, Y.-k. Zhang, and H. Sui, "Pulsating characteristic of the hydraulic hybrid vehicle system with pipeline effect," *Proceedings of the Institution of Mechanical Engineers, Part C: Journal of Mechanical Engineering Science,* vol. 229, no. 12, pp. 2158-2173, 2014.

[51] A. Pfeffer, T. Glück, W. Kemmetmüller, and A. Kugi, "Mathematical modelling of a hydraulic accumulator for hydraulic hybrid drives," *Mathematical and Computer Modelling of Dynamical Systems,* vol. 22, no. 5, pp. 397-411, 2016.

[52] X. Tang, X. Hu, W. Yang, and H. Yu, "Novel Torsional Vibration Modeling and Assessment of a Power-Split Hybrid Electric Vehicle Equipped With a Dual-Mass

Flywheel," *IEEE Transactions on Vehicular Technology,* vol. 67, no. 3, pp. 1990-2000, 2018.

[53] X. Tang, W. Yang, X. Hu, and D. Zhang, "A novel simplified model for torsional vibration analysis of a series-parallel hybrid electric vehicle," *Mechanical Systems and Signal Processing,* vol. 85, pp. 329-338, 2017.

[54] R. Guo and M.-j. Wang, "Active control of hybrid electric vehicle launch vibration in pure electric mode," *Journal of Vibration and Control,* vol. 24, no. 4, pp. 673-681, 2016.

[55] P. D. Walker and N. Zhang, "Modelling of dual clutch transmission equipped powertrains for shift transient simulations," *Mechanism and Machine Theory,* vol. 60, pp. 47-59, 2013.

[56] S. J. Idehara, F. L. Flach, and D. Lemes, "Modeling of nonlinear torsional vibration of the automotive powertrain," *Journal of Vibration and Control,* vol. 24, no. 9, pp. 1774-1786, 2016.

[57] H. Liu, X. Zhang, Y. Chen, M. Taha, and H. Xu, "Active damping of driveline vibration in power-split hybrid vehicles based on model reference control," *Control Engineering Practice,* vol. 91, 2019.

[58] B. Zhong, B. Deng, and H. Zhao, "Simulation Model and Method for Active Torsional Vibration Control of an HEV," *Applied Sciences,* vol. 9, no. 1, 2018.

[59] J.-S. Chen, "Vibration reduction in electric bus during acceleration and gear shifting," *Advances in Mechanical Engineering,* vol. 7, no. 3, 2015.

[60] A. Smith, N. Bucknor, H. Yang, and Y. He, "Controls Development for Clutch-Assisted Engine Starts in a Parallel Hybrid Electric Vehicle," presented at the SAE Technical Paper Series, 2011.

[61] R. I. Davis and R. D. Lorenz, "Engine torque ripple cancellation with an integrated starter alternator in a hybrid electric vehicle: implementation and control," *IEEE Transactions on Industry Applications,* vol. 39, no. 6, pp. 1765-1774, 2003.

[62] H. Zhang, Y. Zhang, and C. Yin, "Hardware-in-the-Loop Simulation of Robust Mode Transition Control for a Series–Parallel Hybrid Electric Vehicle," *IEEE Transactions on Vehicular Technology,* vol. 65, no. 3, pp. 1059-1069, 2016.

[63] F. Zhu, L. Chen, C. Yin, and J. Shu, "Dynamic modelling and systematic control during the mode transition for a multi-mode hybrid electric vehicle," *Proceedings*

of the Institution of Mechanical Engineers, Part D: Journal of Automobile Engineering, vol. 227, no. 7, pp. 1007-1023, 2013.

[64] Z. G. Zhao, H. J. Chen, Y. Y. Yang, and L. He, "Torque coordinating robust control of shifting process for dry dual clutch transmission equipped in a hybrid car," *Vehicle System Dynamics,* vol. 53, no. 9, pp. 1269-1295, 2015.

[65] Y. Yang, C. Wang, Q. Zhang, and X. He, "Torque Coordination Control during Braking Mode Switch for a Plug-in Hybrid Electric Vehicle," *Energies,* vol. 10, no. 11, p. 1684, 2017.

[66] W. Elzaghir, Y. Zhang, N. Natarajan, F. Massey, and C. Mi, "Model Reference Adaptive Control for Hybrid Electric Vehicle with Dual Clutch Transmission Configurations," *IEEE Transactions on Vehicular Technology,* pp. 1-1, 2017.

[67] C. Yang, X. Jiao, L. Li, Y. Zhang, and Z. Chen, "A robust H ∞ control-based hierarchical mode transition control system for plug-in hybrid electric vehicle," *Mechanical Systems and Signal Processing,* vol. 99, pp. 326-344, 2018.

[68] "A Control Strategy for Mode Transition with Gear Shifting in a Plug-In Hybrid Electric Vehicle," *Energies,* vol. 10, no. 7, p. 1043, 2017.

[69] Z. Zhao, D. Lei, J. Chen, and H. Li, "Optimal control of mode transition for four-wheel-drive hybrid electric vehicle with dry dual-clutch transmission," *Mechanical Systems and Signal Processing,* vol. 105, pp. 68-89, 2018.

[70] L. Chen, G. Xi, and J. Sun, "Torque Coordination Control During Mode Transition for a Series–Parallel Hybrid Electric Vehicle," *IEEE Transactions on Vehicular Technology,* vol. 61, no. 7, pp. 2936-2949, 2012.

[71] H. Kim, J. Kim, and H. Lee, "Mode Transition Control Using Disturbance Compensation for a Parallel Hybrid Electric Vehicle," *Proceedings of the Institution of Mechanical Engineers, Part D: Journal of Automobile Engineering,* vol. 225, no. 2, pp. 150-166, 2011.

[72] J. Sun, G. Xing, and C. Zhang, "Data-Driven Predictive Torque Coordination Control during Mode Transition Process of Hybrid Electric Vehicles," *Energies,* vol. 10, no. 4, p. 441, 2017.

[73] S. Wang, B. Xia, C. He, S. Zhang, and D. Shi, "Mode transition control for single-shaft parallel hybrid electric vehicle using model predictive control approach," *Advances in Mechanical Engineering,* vol. 10, no. 5, 2018.

[74] X. Tang, D. Zhang, T. Liu, A. Khajepour, H. Yu, and H. Wang, "Research on the energy control of a dual-motor hybrid vehicle during engine start-stop process," *Energy,* vol. 166, pp. 1181-1193, 2019.

[75] Z. Lei *et al.*, "Analysis and coordinated control of mode transition and shifting for a full hybrid electric vehicle based on dual clutch transmissions," *Mechanism and Machine Theory,* vol. 114, pp. 125-140, 2017.

[76] D. Kum, H. Peng, and N. K. Bucknor, "Control of Engine-Starts for Optimal Drivability of Parallel Hybrid Electric Vehicles," *Journal of Dynamic Systems, Measurement, and Control,* vol. 135, no. 2, 2013.

[77] K. van Berkel, F. Veldpaus, T. Hofman, B. Vroemen, and M. Steinbuch, "Fast and Smooth Clutch Engagement Control for a Mechanical Hybrid Powertrain," *IEEE Transactions on Control Systems Technology,* vol. 22, no. 4, pp. 1241-1254, 2014.

[78] B. Du, X. Yin, and Y. Yang, "Robust control of mode transition for a single-motor full hybrid electric vehicle," *Advances in Mechanical Engineering,* vol. 9, no. 9, p. 168781401771742, 2017.

[79] G. R. Guercioni and A. Vigliani, "Gearshift control strategies for hybrid electric vehicles: A comparison of powertrains equipped with automated manual transmissions and dual-clutch transmissions," *Proceedings of the Institution of Mechanical Engineers, Part D: Journal of Automobile Engineering,* vol. 233, no. 11, pp. 2761-2779, 2018.

[80] M. Awadallah, P. Tawadros, P. Walker, and N. Zhang, "Dynamic modelling and simulation of a manual transmission based mild hybrid vehicle," *Mechanism and Machine Theory,* vol. 112, pp. 218-239, 2017.

[81] J. Liang, H. Yang, J. Wu, N. Zhang, and P. D. Walker, "Shifting and power sharing control of a novel dual input clutchless transmission for electric vehicles," *Mechanical Systems and Signal Processing,* vol. 104, pp. 725-743, 2018.

[82] A. M. Gavgani, A. Sorniotti, J. Doherty, and C. Cavallino, "Optimal gearshift control for a novel hybrid electric drivetrain," *Mechanism and Machine Theory,* vol. 105, pp. 352-368, 2016.

[83] E. Galvagno, M. Velardocchia, and A. Vigliani, "Analysis and simulation of a torque assist automated manual transmission," *Mechanical Systems and Signal Processing,* vol. 25, no. 6, pp. 1877-1886, 2011.

[84] P. D. Walker and N. Zhang, "Numerical investigations into shift transients of a dual clutch transmission equipped powertrains with multiple nonlinearities," *Journal of Vibration and Control,* vol. 21, no. 8, pp. 1473-1486, 2013.

[85] H.-L. Yu, J.-Q. Xi, F.-q. Zhang, and Y.-h. Hu, "Research on Gear Shifting Process without Disengaging Clutch for a Parallel Hybrid Electric Vehicle Equipped with AMT," *Mathematical Problems in Engineering,* vol. 2014, pp. 1-12, 2014.

[86] P. Banerjee and M. Ivantysynova, "Development of a Torque-Based Control Strategy for a Mode-Switching Hydraulic Hybrid Passenger Vehicle," presented at the SAE Technical Paper Series, 2018.

[87] Z. Zhao, H. Chen, J. Yang, X. Wu, and Z. Yu, "Estimation of the vehicle speed in the driving mode for a hybrid electric car based on an unscented Kalman filter," *Proceedings of the Institution of Mechanical Engineers, Part D: Journal of Automobile Engineering,* vol. 229, no. 4, pp. 437-456, 2014.

[88] S. Kim, J. J. Oh, and S. B. Choi, "Driveline Torque Estimations for a Ground Vehicle With Dual-Clutch Transmission," *IEEE Transactions on Vehicular Technology,* vol. 67, no. 3, pp. 1977-1989, 2018.

[89] S. Kim and S. Choi, "Control-oriented modeling and torque estimations for vehicle driveline with dual-clutch transmission," *Mechanism and Machine Theory,* vol. 121, pp. 633-649, 2018/03/01/ 2018.

[90] Z. G. Zhao, L. J. Zhou, J. T. Zhang, Q. Zhu, and J. K. Hedrick, "Distributed and self-adaptive vehicle speed estimation in the composite braking case for four-wheel drive hybrid electric car," *Vehicle System Dynamics,* vol. 55, no. 5, pp. 750-773, 2017.

[91] G. Reina, M. Paiano, and J.-L. Blanco-Claraco, "Vehicle parameter estimation using a model-based estimator," *Mechanical Systems and Signal Processing,* vol. 87, pp. 227-241, 2017.

[92] X. Lu, T. Lu, and B. Chai, "Mode-switch model predictive controller with “pre-contact” method for alleviating driveline vibration of electric vehicles considering backlash," *Proceedings of the Institution of Mechanical Engineers, Part D: Journal of Automobile Engineering,* 2020.

[93] Z. Zhao, L. He, Y. Yang, C. Wu, X. Li, and J. Karl Hedrick, "Estimation of torque transmitted by clutch during shifting process for dry dual clutch transmission," *Mechanical Systems and Signal Processing,* vol. 75, pp. 413-433, 2016.

[94] J. Na, A. S. Chen, G. Herrmann, R. Burke, and C. Brace, "Vehicle Engine Torque Estimation via Unknown Input Observer and Adaptive Parameter Estimation," *IEEE Transactions on Vehicular Technology,* vol. 67, no. 1, pp. 409-422, 2018.

[95] E. Hashemi, R. Zarringhalam, A. Khajepour, W. Melek, A. Kasaiezadeh, and S.-K. Chen, "Real-time estimation of the road bank and grade angles with unknown input observers," *Vehicle System Dynamics,* vol. 55, no. 5, pp. 648-667, 2017.

[96] S.-W. Kang, J.-S. Kim, and G.-W. Kim, "Road roughness estimation based on discrete Kalman filter with unknown input," *Vehicle System Dynamics,* pp. 1-15, 2018.

[97] X. Gong, J. Suh, and C. Lin, "A novel method for identifying inertial parameters of electric vehicles based on the dual H infinity filter," *Vehicle System Dynamics,* pp. 1-21, 2019.

[98] D. X. Ba, K. K. Ahn, D. Q. Truong, and H. G. Park, "Integrated model-based backstepping control for an electro-hydraulic system," *International Journal of Precision Engineering and Manufacturing,* vol. 17, no. 5, pp. 565-577, 2016.

[99] J. Wei, K. Guo, J. Fang, and Q. Tian, "Nonlinear supply pressure control for a variable displacement axial piston pump," *Proceedings of the Institution of Mechanical Engineers, Part I: Journal of Systems and Control Engineering,* vol. 229, no. 7, pp. 614-624, 2015.

[100] W. Kemmetmüller, F. Fuchshumer, and A. Kugi, "Nonlinear pressure control of self-supplied variable displacement axial piston pumps," *Control Engineering Practice,* vol. 18, no. 1, pp. 84-93, 2010.

[101] P. Walker, B. Zhu, and N. Zhang, "Powertrain dynamics and control of a two speed dual clutch transmission for electric vehicles," *Mechanical Systems and Signal Processing,* vol. 85, pp. 1-15, 2017.

[102] B. Wu, C. Lin, Z. Filipi, H. Peng, and D. Assanis, "Optimization of Power Management Strategies fo ra Hydraulic Hybrid Medium Truck," in *Proceeding of the 2002 Advanced Vehicle Control Conference*, 2002.

[103] Z. Filipi and Y. J. Kim, "Hydraulic Hybrid Propulsion for Heavy Vehicles: Combining the Simulation and Engine-In-the-Loop Techniques to Maximize the Fuel Economy and Emission Benefits," *Oil & Gas Science and Technology – Revue de l'Institut Français du Pétrole,* vol. 65, no. 1, pp. 155-178, 2009.

[104] J. Peng, H. He, and R. Xiong, "Rule based energy management strategy for a series–parallel plug-in hybrid electric bus optimized by dynamic programming," *Applied Energy,* vol. 185, pp. 1633-1643, 2017.

[105] S. Park and C. Ahn, "Power Management Controller for a Hybrid Electric Vehicle With Predicted Future Acceleration," *IEEE Transactions on Vehicular Technology,* vol. 68, no. 11, pp. 10477-10488, 2019.

[106] C. Lin, M. Zhao, H. Pan, and J. Yi, "Blending gear shift strategy design and comparison study for a battery electric city bus with AMT," *Energy,* vol. 185, pp. 1-14, 2019.

[107] J. Ruan, P. D. Walker, P. A. Watterson, and N. Zhang, "The dynamic performance and economic benefit of a blended braking system in a multi-speed battery electric vehicle," *Applied Energy,* vol. 183, pp. 1240-1258, 2016.

[108] L. Li, X. Li, X. Wang, J. Song, K. He, and C. Li, "Analysis of downshift's improvement to energy efficiency of an electric vehicle during regenerative braking," *Applied Energy,* vol. 176, pp. 125-137, 2016.

[109] Y. You, D. Sun, and D. Qin, "Shift strategy of a new continuously variable transmission based wheel loader," *Mechanism and Machine Theory,* vol. 130, pp. 313-329, 2018/12/01/ 2018.

[110] N. MANRING, "The torque on the input shaft of an axial-piston swash-plate type hydrostatic pump," *Journal of dynamic systems, measurement, and control,* vol. 120, no. 1, pp. 57-62, 1998.

[111] C. Lv, "The characteristic study on torsion vibration of dual mass flywheel and its simulation analysis," *M.S. Thesis, Sch. of Mech. Eng., Shanghai Jiao tong Univ, Shanghai, 2008*.

[112] G. Rizzoni and Y. Zhang, "Identification of a non-linear internal combustion engine model for on-line indicated torque estimation," *Mechanical Systems and Signal Processing,* vol. 8, no. 3, pp. 275-287, 1994.

[113] J. Ivantysyn and M. Ivantysynova, *Hydrostatic pumps and motors: principles, design, performance, modelling, analysis, control and testing*. Tech Books International, 2003.

[114] M. K. Sethi, P. Kumar, and A. Kumar, "Transient Vibration Reduction of a Powertrain Using MRE Based Adaptive Tuned Vibration Absorber," *Procedia Engineering,* vol. 144, pp. 689-696, 2016.

[115] L.-k. Yang, H.-y. Li, M. Ahmadian, and B. Ma, "Analysis of the influence of engine torque excitation on clutch judder," *Journal of Vibration and Control,* vol. 23, no. 4, pp. 645-655, 2016.

[116] W. Liu, H. He, F. Sun, and H. Wang, "Optimal design of adaptive shaking vibration control for electric vehicles," *Vehicle System Dynamics,* vol. 57, no. 1, pp. 134-159, 2018.

[117] R. Guo, H. Chen, and M.-J. Wang, "Modeling and active control of power-split hybrid electric vehicle launch vibration," *Journal of Low Frequency Noise, Vibration and Active Control,* 2018.

[118] X. Qi, Y. Yang, X. Wang, and Z. Zhu, "Analysis and optimization of the gear-shifting process for automated manual transmissions in electric vehicles," *Proceedings of the Institution of Mechanical Engineers, Part D: Journal of Automobile Engineering,* vol. 231, no. 13, pp. 1751-1765, 2017.

[119] Y. Tian, J. Ruan, N. Zhang, J. Wu, and P. Walker, "Modelling and control of a novel two-speed transmission for electric vehicles," *Mechanism and Machine Theory,* vol. 127, pp. 13-32, 2018/09/01/ 2018.

[120] B. Gao, Y. Xiang, H. Chen, Q. Liang, and L. Guo, "Optimal Trajectory Planning of Motor Torque and Clutch Slip Speed for Gear Shift of a Two-Speed Electric Vehicle," *Journal of Dynamic Systems, Measurement, and Control,* vol. 137, no. 6, p. 061016, 2015.

[121] M. Liu, F. Gu, J. Huang, C. Wang, and M. Cao, "Integration Design and Optimization Control of a Dynamic Vibration Absorber for Electric Wheels with In-Wheel Motor," *Energies,* vol. 10, no. 12, p. 2069, 2017.

[122] L. Jin, L. Gao, Y. Jiang, M. Chen, Y. Zheng, and K. Li, "Research on the control and coordination of four-wheel independent driving/steering electric vehicle," *Advances in Mechanical Engineering,* vol. 9, no. 4, p. 168781401769887, 2017.

[123] L. Li, Z. Zhu, Y. Chen, K. He, X. Li, and X. Wang, "Engagement control of automated clutch for vehicle launching considering the instantaneous changes of driver's intention," *Journal of Dynamic Systems, Measurement, and Control,* vol. 139, no. 2, p. 021011, 2017.

[124] J. Liang, H. Yang, J. Wu, N. Zhang, and P. D. Walker, "Power-on shifting in dual input clutchless power-shifting transmission for electric vehicles," *Mechanism and Machine Theory,* vol. 121, pp. 487-501, 2018.

[125] Z. Zhao, J. Chen, X. Li, and D. Lei, "Downshift decision and process optimal control of dual clutch transmission for hybrid electric vehicles under rapid braking condition," *Mechanical Systems and Signal Processing,* vol. 116, pp. 943-962, 2019/02/01/ 2019.

[126] B. Gao, Q. Liang, Y. Xiang, L. Guo, and H. Chen, "Gear ratio optimization and shift control of 2-speed I-AMT in electric vehicle," *Mechanical Systems and Signal Processing,* vol. 50-51, pp. 615-631, 2015.

[127] J. J. Oh and S. B. Choi, "Real-Time Estimation of Transmitted Torque on Each Clutch for Ground Vehicles With Dual Clutch Transmission," *IEEE/ASME Transactions on Mechatronics,* vol. 20, no. 1, pp. 24-36, 2015.

[128] N. P. Mandal, R. Saha, S. Mookherjee, and D. Sanyal, "Pressure Compensator Design for a Swash Plate Axial Piston Pump," *Journal of Dynamic Systems, Measurement, and Control,* vol. 136, no. 2, 2013.

[129] Y. Sun, L. Li, B. Yan, C. Yang, and G. Tang, "A hybrid algorithm combining EKF and RLS in synchronous estimation of road grade and vehicle′ mass for a hybrid electric bus," *Mechanical Systems and Signal Processing,* vol. 68-69, pp. 416-430, 2016.

[130] H. Guo, H. Chen, F. Xu, F. Wang, and G. Lu, "Implementation of EKF for Vehicle Velocities Estimation on FPGA," *IEEE Transactions on Industrial Electronics,* vol. 60, no. 9, pp. 3823-3835, 2013.

[131] S. De Pinto *et al.*, "On the Comparison of 2- and 4-Wheel-Drive Electric Vehicle Layouts with Central Motors and Single- and 2-Speed Transmission Systems," *Energies,* vol. 13, no. 13, 2020.

[132] L. Shao, A. E. H. Karci, D. Tavernini, A. Sorniotti, and M. Cheng, "Design Approaches and Control Strategies for Energy-Efficient Electric Machines for Electric Vehicles—A Review," *IEEE Access,* vol. 8, pp. 116900-116913, 2020.

[133] J. Hu, H. Ran, T. Pang, and Y. Zhang, "Parameter design and performance analysis of shift actuator for a two-speed automatic mechanical transmission for pure electric vehicles," *Advances in Mechanical Engineering,* vol. 8, no. 8, p. 168781401666425, 2016.

[134] L. Guo, B. Gao, and H. Chen, "Online Shift Schedule Optimization of 2-Speed Electric Vehicle Using Moving Horizon Strategy," *IEEE/ASME Transactions on Mechatronics,* vol. 21, no. 6, pp. 2858-2869, 2016.

[135] J. Liang, P. D. Walker, J. Ruan, H. Yang, J. Wu, and N. Zhang, "Gearshift and brake distribution control for regenerative braking in electric vehicles with dual clutch transmission," *Mechanism and Machine Theory,* vol. 133, pp. 1-22, 2019.

[136] Y. Tian, H. Yang, W. Mo, S. Zhou, N. Zhang, and P. D. Walker, "Optimal coordinating gearshift control of a two-speed transmission for battery electric vehicles," *Mechanical Systems and Signal Processing,* vol. 136, 2020.

[137] W. Wang, J. Li, and F. Sun, "Pseudo-spectral optimisation of smooth shift control strategy for a two-speed transmission for electric vehicles," *Vehicle System Dynamics,* pp. 1-26, 2019.

[138] J. Ruan, P. Walker, and N. Zhang, "A comparative study energy consumption and costs of battery electric vehicle transmissions," *Applied Energy,* vol. 165, pp. 119-134, 2016.

[139] F. Bottiglione, S. De Pinto, G. Mantriota, and A. Sorniotti, "Energy Consumption of a Battery Electric Vehicle with Infinitely Variable Transmission," *Energies,* vol. 7, no. 12, pp. 8317-8337, 2014.

[140] S. Murata, "Innovation by in-wheel-motor drive unit," *Vehicle System Dynamics,* vol. 50, no. 6, pp. 807-830, 2012.

[141] L. De Novellis, A. Sorniotti, P. Gruber, and A. Pennycott, "Comparison of Feedback Control Techniques for Torque-Vectoring Control of Fully Electric Vehicles," *IEEE Transactions on Vehicular Technology,* vol. 63, no. 8, pp. 3612-3623, 2014.

[142] Z. Shuai, H. Zhang, J. Wang, J. Li, and M. Ouyang, "Combined AFS and DYC Control of Four-Wheel-Independent-Drive Electric Vehicles over CAN Network with Time-Varying Delays," *IEEE Transactions on Vehicular Technology,* vol. 63, no. 2, pp. 591-602, 2014.

[143] D. Lim, M.-Y. Lee, H.-S. Lee, and S. Kim, "Performance Evaluation of an In-Wheel Motor Cooling System in an Electric Vehicle/Hybrid Electric Vehicle," *Energies,* vol. 7, no. 2, pp. 961-971, 2014.

[144] D. Tan and C. Lu, "The Influence of the Magnetic Force Generated by the In-Wheel Motor on the Vertical and Lateral Coupling Dynamics of Electric Vehicles," *IEEE Transactions on Vehicular Technology,* vol. 65, no. 6, pp. 4655-4668, 2016.

[145] S. Zhou, P. Walker, and N. Zhang, "Parametric design and regenerative braking control of a parallel hydraulic hybrid vehicle," *Mechanism and Machine Theory,* vol. 146, 2020.

[146] L. Wang, X. Liu, X. Wang, B. Fu, and R. Xu, "Research on differential performance of four-wheel independent steering of a hydraulic wheel-driving off-road vehicle," *The Journal of Engineering,* vol. 2019, no. 13, pp. 68-73, 2019.

[147] Z. Yang, F. Shang, I. P. Brown, and M. Krishnamurthy, "Comparative Study of Interior Permanent Magnet, Induction, and Switched Reluctance Motor Drives for EV and HEV Applications," *IEEE Transactions on Transportation Electrification,* vol. 1, no. 3, pp. 245-254, 2015.

[148] Z. Chen and A. Vahidi, "Route Preview in Energy Management of Plug-in Hybrid Vehicles," *IEEE Transactions on Control Systems Technology,* vol. 20, no. 2, pp. 546-553, 2012.

[149] T. Liu, X. Tang, H. Wang, H. Yu, and X. Hu, "Adaptive Hierarchical Energy Management Design for a Plug-In Hybrid Electric Vehicle," *IEEE Transactions on Vehicular Technology,* vol. 68, no. 12, pp. 11513-11522, 2019.

[150] X. Zhang, D. Gohlich, and J. Li, "Energy-Efficient Toque Allocation Design of Traction and Regenerative Braking for Distributed Drive Electric Vehicles," *IEEE Transactions on Vehicular Technology,* vol. 67, no. 1, pp. 285-295, 2018.

[151] Z. Song *et al.*, "Torque Distribution Strategy for Multi-PMSM Applications and Optimal Acceleration Control for Four-Wheel-Drive Electric Vehicles," *Journal of Dynamic Systems, Measurement, and Control,* vol. 142, no. 2, 2020.

[152] D. Van Schalkwyk and M. Kamper, "Effect of hub motor mass on stability and comfort of electric vehicles," in *2006 IEEE vehicle power and propulsion conference*, 2006, pp. 1-6: IEEE.

[153] H. Qi, Y. Chen, N. Zhang, B. Zhang, D. Wang, and B. Tan, "Improvement of both handling stability and ride comfort of a vehicle via coupled hydraulically interconnected suspension and electronic controlled air spring," *Proceedings of the Institution of Mechanical Engineers, Part D: Journal of Automobile Engineering,* vol. 234, no. 2-3, pp. 552-571, 2019.

[154] M. Liu, Y. Zhang, J. Huang, and C. Zhang, "Optimization control for dynamic vibration absorbers and active suspensions of in-wheel-motor-driven electric

vehicles," *Proceedings of the Institution of Mechanical Engineers, Part D: Journal of Automobile Engineering,* 2020.

[155] L. Zhao, C. Zhou, Y. Yu, and F. Yang, "An analytical formula of driver RMS acceleration response for quarter-car considering cushion effects," *Vehicle System Dynamics,* vol. 55, no. 9, pp. 1283-1296, 2017.

[156] G. Ślaski, A. Gudra, and A. Borowicz, "Analysis of the influence of additional unsprung mass of in-wheel motors on the comfort and safety of a passenger car," *Archiwum Motoryzacji,* vol. 65, no. 3, 2014.